# Investigation of magnetized dissipative accretion flow around Black Holes

*A thesis submitted in partial fulfilment of the requirements for the award of*

**Doctor of Philosophy**

by

**Biplob Sarkar**

Department of Physics
Indian Institute of Technology Guwahati
Guwahati 781039, India.

March 2018

*I would like to dedicate this thesis to my parents and to all the great Teachers mankind has known . . .*

# Declaration

I hereby declare that the contents of this thesis are original and have not been submitted for consideration for any other degree or qualification in this, or any other university. This dissertation is my own work and contains nothing which is the outcome of work done by others, except for the collaboration as specified in the text and Acknowledgements.

Biplob Sarkar
March 2018

# Certificate

This is to certify that the work contained in the thesis entitled “**Investigation of magnetized dissipative accretion flow around Black Holes**” submitted by Mr. Biplob Sarkar in the partial fulfillment of the requirement for the award of the degree of Doctor of Philosophy in Physics, Department of Physics, Indian Institute of Technology Guwahati, is a record of the candidate’s own work carried out by him under my supervision and guidance. The matter embodied in this report has not been submitted in part or full to any other university or institute for the award of any degree.

Dr. Santabrata Das
Associate Professor
Department of Physics
Indian Institute of Technology Guwahati
Guwahati - 781039
Assam, India.

March 2018

# Acknowledgements

Once a great teacher in days of old gave the following instruction to his equally great disciple on the battlefield:

*"Your right is to work only; but never to the fruits thereof.*
*May you not be motivated by the fruits of actions; nor let*
*your attachment be towards inaction."*

To begin with I pay my deepest regards to that great teacher for such a profound teaching which has been a guiding light to humanity since ages and which shall continue to do so.

I am thankful to my Ph.D. supervisor Dr. Santabrata Das for introducing me to the theoretical studies of black hole astrophysics. I thank him for his guidance, encouragement, constant help and support and for pointing out my drawbacks which helped me to bring out the best in myself.

I am fortunate to receive the opportunity to pursue my Ph.D. Degree at Department of Physics, IIT Guwahati. I acknowledge the computational and other facilities provided by the Department and Institute for smooth conduct of the research.

I would also like to thank my doctoral committee, chairman Dr. Subhradip Ghosh and members Dr. Tarak Nath Dey and Dr. Lal Mohan Kundu, for their comments and suggestions.

Particular thanks goes to my co-author, Dr. Samir Mandal for his valuable help and contributions.

I acknowledge the financial assistance from MHRD and Equal Opportunity Cell of IIT Guwahati for successful completion of my research work.

I also like to extend my warmest regards to Dr. Sibasish Laha, Dr. Bhupendra Mishra, Dr. Rajiv Kumar, Dr. Rajitha K. V., Dr. Anjali Rao and Dr. Indrani Banerjee, who were always open and available for scientific discussions.

I am thankful for the support and care of all my Ph.D. batchmates. Their support eased the path of the Ph.D. life a great deal. In particular I would like to extend my best regards to Debashish, Kartik, Tapas, Sandeep, Gyan and Shantakumar. I also thank all my seniors and the members of the numerical lab for a pleasant and supportive work atmosphere. Special thanks goes to Sourav for all the technical help.

I was fortunate to have bright and extremely talented group members, Ramiz and Indu. It has been a wonderful experience working with them and I have been enriched in many ways.

I have spent many wonderful days training at the IITG Karate Dojo and I would cherish those memories.

Among the many books that I have read during these Ph.D. years, a few have had a huge impact on my life. I think it would be highly unfair not to mention them as they have helped me to face the tough times. I would like to acknowledge the motivation and inspiration I received from *Think and Grow Rich* by Napoleon Hill, *The Power of Positive Thinking* by Dr. Norman Vincent Peale, *The Alchemist* and *Manual Of The Warrior Of Light* by Paulo Coelho and the classic *Man's Search for Meaning* by Dr. Viktor E. Frankl.

Last but not least, I'd like to acknowledge the support and love of my family members throughout all these years.

# Abstract

In general, it is accepted that magnetic fields have a principal effect on the physics of accretion discs around black holes. For instance, magnetorotational instability can excite and maintain magnetic turbulence, whereby angular momentum can be transported outward. Again, dissipation of magnetic energy contributes to the heating of the disc. It has been shown through extensive numerical simulations that the inner region of the accretion flow around a black hole is likely to be threaded by a large-scale toroidal magnetic field, while on a small scale, magnetic field lines are stochastic in nature. In this thesis, we have presented the efforts to investigate steady, optically thin, accretion solutions in such magnetized accretion discs around black holes. The magnetic fields inside the disc are considered to be turbulent and dominated by the azimuthal component. The vertical structure of the disc is supported against gravity through the combined effects of gas and magnetic pressure. In the absence of any coupling between ions and electrons in the disc, we have approximated the electron temperature as a fraction of the ion temperature. Moreover, in the thesis, we consider that the heating of the flow takes place due to the thermalization of magnetic energy through the magnetic reconnection mechanism. Towards this, we consider a set of magnetohydrodynamic equations in the steady state to model the dissipative accretion flow in the disc.

In the first work, we focus on supermassive black hole sources and mimic the effect of space time geometry around the black hole by employing the pseudo-Newtonian potential. We have considered Comptonization of the bremsstrahlung radiation to be the prospective cooling mechanism in the flow. With this, we obtain the global transonic accretion solutions for dissipative magnetized flows and show that rotating magnetized accretion flow harbours centrifugally supported shock waves. We examine the properties of the shock waves and find that the dynamics of the post-shock corona (PSC) is controlled by the flow parameters, namely, viscosity, cooling efficiency factor ($\xi$) and strength of the magnetic field, respectively. We separate the effective region of

the parameter space for standing shock and observe that shock can form for a wide range of flow parameters. We show that maximum disc luminosity always remains higher for shocked flows as compared to the shock free case. We obtain the critical viscosity parameter that allows global accretion solutions including shocks. We compute the maximum energy that could be extracted from the PSC. This is compared against the observed radio luminosity values for several supermassive black hole sources and close agreement is seen.

In the second work, we concentrate on magnetized accretion flows around non-rotating stellar mass black holes. For these systems, we have considered synchrotron cooling as the dominant radiative process active in the flow. Here also, the general relativistic effects are simulated using the pseudo-Newtonian potential. With this, we obtain the global transonic accretion solutions and depending on the initial parameters, steady state accretion flows are shown to possess centrifugally supported shock waves. We calculate the critical value of viscosity parameter for shock ($\alpha_B^{\rm cri}$) adopting the canonical values of adiabatic indices as $\gamma = 4/3$ (ultra-relativistic) and 1.5 (semi-non-relativistic). We further show that global shock solutions are relatively more luminous compared to the shock free solutions. Also, we have calculated the synchrotron spectra for shocked solutions. We find that when magnetic field is large, the flow is radiatively more efficient and the spectrum is shifted towards high energy. Considering the dissipative nature of shock, we calculate the maximum shock luminosity and discuss the observational implication of the present formalism.

In the thrid work, we extend the formulations of the second work to include the effect of rotation of the black hole. In order to mimic the geometry of space time around a rotating black hole, we use the pseudo-Kerr potential. We show that the rotation of the black hole significantly affects the shock properties and the dynamics of the PSC. We investigate the shock properties against the inflow parameters and observe that standing shock continues to form around the rapidly rotating black holes as well. We classify the parameter space spanned by critical accretion rate ($\dot{m}^{\rm cri}$) and viscosity ($\alpha_B$) into regions that allow closed accretion solution (passing through the inner sonic point only) and standing accretion shocks. Further, we observe that standing shock exists in a magnetically dominated accretion flow when the accretion rate lies in general in the sub-Eddington domain. We also compute the maximum energy that could be extracted from the PSC and study its variation with magnetic parameter $\beta$ and spin of the black hole. In the final part, we present the conclusions of our work.

# List of Publications

## Publications in journals:

1. *Standing shocks in magnetized dissipative accretion flow around black holes*,
   **Biplob Sarkar** and Santabrata Das, 2018, Journal of Astrophysics and Astronomy, 39, 3

2. *Properties of magnetically supported dissipative accretion flow around black holes with cooling effects*,
   **Biplob Sarkar**, Santabrata Das and Samir Mandal, 2018, Monthly Notices of the Royal Astronomical Society, 473, 2415

3. *Dynamical structure of magnetized dissipative accretion flow around black holes*,
   **Biplob Sarkar** and Santabrata Das, 2016, Monthly Notices of the Royal Astronomical Society, 461, 190

4. *On the possibilities of mass loss from an advective accretion disc around stationary black holes*,
   Santabrata Das, Indranil Chattopadhyay, Anuj Nandi and **Biplob Sarkar**, 2014, Bulletin of the Astronomical Society of India, 42, 39

## Papers submitted to journals:

1. *Standing shocks in magnetized advection accretion flows onto a rotating black hole*,
   Santabrata Das and **Biplob Sarkar**, Monthly Notices of the Royal Astronomical Society (Under review)

# Publications in conference proceedings:

1. *Shocks in magnetically supported accretion flow around black holes*,
   **Biplob Sarkar** and Santabrata Das, 2015, Astron. Soc. India Conf. Ser., 12, 91

2. *Dissipative standing shocks in accretion flows around black holes: a self-consistent analytical study*,
   **Biplob Sarkar** and Santabrata Das, 2013, Astron. Soc. India Conf. Ser., 8, 143

# Conferences/Workshops/Schools

## Oral presentation

1. "*Shocks in magnetically supported accretion disc*", **Biplob Sarkar** and Santabrata Das, in *Accretion Onto Black Holes, A topical conference*, International Center, Goa, September 5-7, 2013 organized by TIFR.

2. "*Effects of magnetic fields on shocks in BH accretion discs*", **Biplob Sarkar** and Santabrata Das, in the conference, *Hard X-ray Astronomy: Astrosat and Beyond*, International Center, Goa, September 24-26, 2014 organized by TIFR.

3. "*Magnetically supported viscous accretion flow around Black Holes*", **Biplob Sarkar**, Santabrata Das and Samir Mandal, in National conference on *Recent Trends in the Study of Compact Objects: Theory and Observation (RETCO-II)*, 6-8 May, 2015, ARIES, Nainital, India.

4. "*Accretion flow around black holes*", **Biplob Sarkar**, in a one day symposium on *100 years of General Relativity: Where do we stand?*, 13 February, 2016, Department of Physics, IIT Guwahati.

5. "*Magnetically supported accretion flow around black holes with shocks*", **Biplob Sarkar**, in the *Department Day, Physics*, 12 March, 2016, organized by Research Scholar Forum (RSF), Department of Physics, IIT Guwahati.

6. "*Implications of standing shocks in magnetized accretion discs around black holes*", **Biplob Sarkar** and Santabrata Das, in the conference, '*Wide Band Spectral and Timing Studies of Cosmic X-ray Sources*', January 10-13, 2017, organized by TIFR, Mumbai, India.

7. "*Hints from standing shocks in magnetized accretion flows around black holes*", **Biplob Sarkar**, in the *Annual Physics Meet*, 28 January, 2017, organized by Research Scholar Forum (RSF), Department of Physics, IIT Guwahati.

8. "*Properties of magnetically supported dissipative accretion flow around black holes*", **Biplob Sarkar**, Santabrata Das and Samir Mandal, in the *29th meeting of the Indian Association for General Relativity and Gravitation (IAGRG)*, May 18-20, 2017, organized by Department of Physics, IIT Guwahati, Assam, India.

## Poster presentation

1. "*Self-consistent study of dissipative standing shocks in accretion flows around black holes*", **Biplob Sarkar** and Santabrata Das, in National conference on *Recent Trends in the Study of Compact Objects: Theory and Observation*, 11-13 March, 2013, Indian Institute of Technology Guwahati, Assam, India.

2. "*Astrophysical flows around black holes*", Indu Kalpa Dihingia, Ramiz Aktar and **Biplob Sarkar**, in the *Research Conclave'15* organized by Students' Academic Board, 23-26 March, 2015, IIT Guwahati.

3. "*Accretion around Black Hole, A Journey*", Indu Kalpa Dihingia, Ramiz Aktar and **Biplob Sarkar**, in the *Research Conclave'16* organized by Students' Academic Board, 17-20 March, 2016, IIT Guwahati.

4. "*Dissipative accretion flow around Black Holes*", Indu Kalpa Dihingia, Ramiz Aktar and **Biplob Sarkar**, in the *Research Conclave'17* organized by Students' Academic Board, 16-19 March, 2017, IIT Guwahati.

## Workshop/School attended

1. Quality Improvement Program on *Computational Techniques in Physics*, 1-6 August, 2011, Department of Physics, IIT Guwahati.

2. Workshop on *Multiwavelength Astronomy with Astrosat*, 9-12 January, 2012, IIST, Trivandrum.

3. IUCAA Sponsored *Introductory Workshop on Relativistic Astrophysics (IWRAP)*, 21-23 August, 2014, Department of Physics, Gauhati University, Guwahati.

# Contents

**List of figures** xix

**List of tables** xxiii

**1 Introduction** 1

1.1 Models of Accretion Discs . . . 3

1.1.1 Standard Disc (Shakura-Sunyaev) . . . 3

1.1.2 SLE . . . 4

1.1.3 Slim Disc . . . 5

1.1.4 ADAF . . . 5

1.2 Importance of the Magnetic Fields . . . 7

1.3 Treatment of gravitational field around a Black Hole . . . 9

1.3.1 Pseudo-Newtonian Potential . . . 13

1.3.2 Pseudo-Kerr Potential . . . 15

1.4 Radiative processes . . . 16

1.5 Concept of Optical Depth . . . 18

1.6 Shocks in Accretion Flow . . . 19

1.7 Over view of the work . . . 22

**2 Magnetized accretion flows in presence of bremsstrahlung cooling process** 27

2.1 Model for the accretion flow . . . 30

2.1.1 Governing Equations . . . 30

2.1.2 Sonic Point Analysis . . . 34

2.2 Global Accretion Solution . . . 37

2.2.1 Shock free global accretion solution . . . 39

2.2.2 Shock induced global accretion solution . . . 40

2.2.3 Shock dynamics and properties . . . 44
2.2.4 Accretion disc luminosity . . . 48
2.2.5 Parameter space for shock . . . 50
2.2.6 Critical viscosity parameter . . . 52
2.3 Astrophysical Applications . . . 52
2.4 Chapter Conclusion . . . 56

**3 Magnetically supported accretion flows in presence of synchrotron cooling 59**
3.1 Governing Equations . . . 60
3.1.1 Sonic Point Analysis . . . 61
3.2 Results . . . 64
3.2.1 Global accretion solution . . . 64
3.3 Chapter Conclusion . . . 84

**4 Advective magnetized accretion flow around rotating black hole 87**
4.1 Governing Equations . . . 88
4.1.1 Analysis of transonic conditions . . . 92
4.2 Results and Discussions . . . 95
4.2.1 Transonic Global Solutions . . . 95
4.2.2 Global Accretion Solutions with Shock . . . 95
4.2.3 Properties of Standing Shocks . . . 97
4.2.4 Parameter Space for Shock . . . 102
4.2.5 Energy Extraction from PSC . . . 108
4.3 Chapter Conclusion . . . 110

**5 Conclusions and Future perspective 113**

**References 117**

# List of figures

1.1 Comparison of the general relativistic (solid) and Newtonian (dashed) effective potentials against $r$ for $l = 4.2$. . . . . . . . . . . . . . . . . . . . 12

1.2 Comparison of the general relativistic (solid) and pseudo-Newtonian (dashed) effective potentials against $r$ for $l = 4.2$. . . . . . . . . . . . . . 14

2.1 Radial dependence of Mach number ($M = v/a$) of the accreting matter for different values of angular momentum ($\lambda_{\rm edge}$) at the outer edge. . . 38

2.2 A complete global accretion solution containing shock is depicted along with outer ($x_{\rm out}$) and inner ($x_{\rm in}$) sonic points. . . . . . . . . . . . . . . 40

2.3 Variation of flow variables as function of radial coordinate around a Schwarzschild black hole. . . . . . . . . . . . . . . . . . . . . . . . . . . . 42

2.4 Plot of Mach number with logarithmic radial distance for different values of cooling factor ($\xi$). . . . . . . . . . . . . . . . . . . . . . . . . . . . 43

2.5 Plot of Mach number with logarithmic radial distance for different values of $\beta_{\rm edge}$. . . . . . . . . . . . . . . . . . . . . . . . . . . . . . . . . . 45

2.6 Variation of different flow properties such as (a) the shock location $x_s$, (b) shock compression ratio $R$, and (c) shock strength $\Theta$ as a function of $\xi$. . . . . . . . . . . . . . . . . . . . . . . . . . . . . . . . . . . . . . 46

2.7 Variation of different flow properties such as (a) the shock location $x_s$, (b) shock compression ratio $R$, and (c) shock strength $\Theta$ as a function of $\beta_{\rm edge}$. . . . . . . . . . . . . . . . . . . . . . . . . . . . . . . . . . . 48

2.8 Variation of maximum disc luminosity $L_{\rm disc}^{\rm max}$ as a function of cooling efficiency factor $\xi$. . . . . . . . . . . . . . . . . . . . . . . . . . . . . . 49

2.9 Separations of the parameter space that allow stationary shock waves in the $\lambda_{\rm in} - \xi$ plane. . . . . . . . . . . . . . . . . . . . . . . . . . . . 50

2.10 Effective regions of the parameter space for stationary shock in the $\lambda_{\rm in} - \xi$ plane. . . . . . . . . . . . . . . . . . . . . . . . . . . . . . . . 51

2.11 Variation of critical viscosity parameter ($\alpha_B^{\rm cri}$) with $\beta_{\rm in}$ that allows standing shocks. . . . . . . . . . . . . . . . . . . . . . . . . . . . . 53

3.1 Radial dependence of Mach number ($M = v/a$) of the accreting matter for different values of plasma $\beta$ ($\beta_{\rm in}$) at the inner sonic point $x_{\rm in}$. . . . . 65
3.2 Illustration of a complete global accretion solution including shock transition in the $\log x - M$ plane. . . . . . . . . . . . . . . . . . . . . . . 68
3.3 Variation of Mach number as function of logarithmic radial distance. . 69
3.4 Variation of different flow properties as function of logarithmic radial coordinate. . . . . . . . . . . . . . . . . . . . . . . . . . . . . . . . 71
3.5 Variation of (a) shock location $x_s$, (b) compression ratio $R$, and (c) shock strength $\Theta$ as function of $\dot{m}$. . . . . . . . . . . . . . . . . . . . . 73
3.6 Variation of (a) the shock location $x_s$ (b) shock compression ratio $R$ and (c) shock strength $\Theta$ as function of $\beta_{\rm edge}$. . . . . . . . . . . . . . 74
3.7 Variation of (a) the shock location $x_s$ (b) shock compression ratio $R$ and (c) shock strength $\Theta$ as function of viscosity $\alpha_{\rm B}$ for different values of $\lambda_{\rm edge}$. . . . . . . . . . . . . . . . . . . . . . . . . . . . . . . . . 76
3.8 Variation of critical viscosity parameter ($\alpha_B^{\rm cri}$) as function of plasma $\beta$ at inner sonic point ($\beta_{\rm in}$) that allows standing shocks. . . . . . . . . . 77
3.9 Variation of critical accretion rate $\dot{m}^{\rm cri}$ that allows standing shock as function of $\beta_{\rm in}$. . . . . . . . . . . . . . . . . . . . . . . . . . . . . . 78
3.10 Typical spectra from an accretion disc around a black hole of mass $M = 10{\rm M}_\odot$ for a strong and weak accretion shock located at $x_s = 13.14$ and 72.12 respectively. . . . . . . . . . . . . . . . . . . . . . . . . . 79
3.11 Variation of maximum disc luminosity $L_{\rm disc}^{\rm max}$ as a function of accretion rate $\dot{m}$. . . . . . . . . . . . . . . . . . . . . . . . . . . . . . . . . . 81
3.12 Variation of maximum energy dissipation at shock ($\Delta\mathcal{E}^{\rm max}$) as a function of $\beta$ at inner sonic point ($\beta_{\rm in}$) for three different values of accretion rates. 82

4.1 Plot of Mach number with logarithmic radial distance. . . . . . . . . . 96
4.2 Shock location ($x_s$) variation with $\beta_{\rm edge}$. . . . . . . . . . . . . . . . . . 98
4.3 Variation of the shock location ($x_s$) as function of $\beta_{\rm out}$ (lower axis) and $\beta_{\rm in}$ (upper axis). . . . . . . . . . . . . . . . . . . . . . . . . . . . . . 99
4.4 Variation of the shock location ($x_s$) as function of $\dot{m}$. . . . . . . . . . . 100
4.5 Variation of the shock location ($x_s$) as function of $\alpha_B$. . . . . . . . . . . 102

4.6 Variation of critical accretion rate ($\dot{m}^{\rm cri}$) as a function of viscosity parameter ($\alpha_B$) for various $a_k$. . . . . . . . . . . . . . . . . . . . . . . . . 103
4.7 Variation of critical accretion rate ($\dot{m}^{\rm cri}$) for standing accretion shock with viscosity parameter ($\alpha_B$) for different $\beta_{\rm in}$. . . . . . . . . . . . . . . . 105
4.8 Comparison of critical accretion rate $\dot{m}^{\rm cri}$ for shock with $\beta_{\rm in}$. . . . . . . . 106
4.9 Variation of critical accretion rate $\dot{m}^{\rm cri}$ with $a_k$ for shock. . . . . . . . . 107
4.10 Plot of maximum energy dissipation ($\Delta\mathcal{E}^{\rm max}$) at the shock with $a_k$ for three distinct values of $\beta_{\rm in}$. . . . . . . . . . . . . . . . . . . . . . . . . . . . 108

# List of tables

2.1 Estimation of shock luminosity. Column 1 lists the names of the sources and Column 2-3 give mass and accretion rate. Column 4-7 provide the model parameters and Column 8-10 denote the maximum energy dissipation, shock location and estimated maximum shock luminosity obtained from equation (2.20). Observed core radio luminosity values are given in column 11 (Sarkar and Das 2016). . . . . . . . . . . . . . . . 55

3.1 Flow variables measured at the sonic points for a shock induced global accretion solution. See text for details (Sarkar, Das, and Mandal 2018). 70

# Chapter 1

# Introduction

Accretion of matter onto a compact object is widely believed to serve as a powerful source of energy in various astrophysical sources, including X-ray binaries, cataclysmic variables, quasars and active galactic nuclei (AGN). Although the development of accretion theory was first begun long time ago (Bondi and Hoyle 1944, Bondi 1952), the process of rigorously developing this theory started after the discovery of first X-ray sources (Giacconi *et al.* 1962) and quasars (Schmidt 1963). In the final stage of accretion onto stars, matter crashes with an inner boundary. This boundary may be the surface of the star, or exterior boundary of a magnetosphere when the star is strongly magnetized. In this case, we may be assured that all gravitational energy of the falling matter will be changed into heat and subsequently transmitted outward.

The situation is altered when the gravitating systems have black holes at their centers. When a black hole resides at the center, matter gravitates towards the horizon. Since radiation is not emitted from the region inside the horizon, the entire luminosity originates from the accretion flow in the course of its journey towards the black hole. Meanwhile, a number of binary X-ray sources within the galaxy have been discovered to have black holes at their centers (Chen and Taam 1994, Ziolkowski 2010). It was recommended by Zel'dovich and Novikov (1964) and Salpeter (1964) that the centers of AGNs may have black holes. According to Madejski, Done, and Zycki (1999), presence of a black hole at the center of the gravitating system is the most viable model to explain AGN.

In an accreting binary X-ray source, matter is accumulated around the black hole from the stellar wind or from the binary counterpart. Here, the binary counterpart is a typical star that fills its Roche lobe. For AGNs, the super massive black hole at the center will accumulate matter from the encompassing gas cloud, interstellar medium or stars in orbit around the black hole. Since matter accreting towards the black hole invariably carries angular momentum, this prevents the matter to fall radially inward. Matter rather moves inward gradually in spiral path forming a disc like depository commonly called as accretion disc. Without any dissipative processes, the matter may circle in Keplerian orbits around the black hole creating a differentially rotating disc. Due to viscous stress arising form differential rotation, the angular momentum in the disc is redistributed and matter transfers angular momentum to the outside. Consequently, matter falls in the deep potential well of the black hole. Accreting matter loses a huge sum of gravitational potential energy while falling towards the black hole and this energy apparently is transmitted away. This is the mechanism that powers the binary X-ray sources. In this approach, the self-gravity of the disc is disregarded since it is insignificant. One of the early models considered for galactic X-rays sources using accretion discs was proposed by Pringle and Rees (1972). In addition, Lynden-Bell (1969) considered the accretion disc around a Schwarzschild black hole in the galactic nuclei as a model for quasars.

One of the essential quest in the accretion disc theory is the inception of the transport of angular momentum in discs. The molecular viscosity of the fluid in the accretion disc is insufficient to account for the outward transport of angular momentum in a Keplerian disc. It is also unable to account for the observed luminosities from the discs. Thus, the viscosity in accretion discs must be significantly greater than the molecular viscosity. Since the initial studies of accretion discs, it is accepted that the gas flow in accretion discs is turbulent in nature (Shakura and Sunyaev 1973). However, the physical mechanisms associated with the onset of trubulence still remians unclear. Nevertheless, it is possible to introduce an *effective viscosity* so that the stresses inside the disc are parametrized. While doing this, we assume the maximum length of mean free path $\lambda$ for random motions which is equivalent to the thickness of the disc $h$. This would be normally expected when the random motions contributing to angular momentum transport are perturbations of maximum size. The characteristic velocity for this is considered to be the sound speed $a$. Hence, we parametrize the viscosity as

$$\nu = \alpha a h,$$

where $\nu$ is the kinematic viscosity. This prescription is known as the *$\alpha$-prescription* (Shakura and Sunyaev 1973). The original work by Shakura and Sunyaev (1973) was a breakthrough in the initial endeavors to interface the emitted radiation to the flow of gas in the accretion disc. This Keplerian disc model is now considered to be a "standard" model where fluid blobs move around the central object in Keplerian orbits.

As has been already indicated, that the turbulence in the accretion discs is the essential driver for angular momentum transport to greater radii. The mechanism to generate sustained turbulence in accretion discs had remained a puzzle for a long time until Balbus and Hawley (1991) demonstrated the importance of Magneto-Rotational Instability (MRI) in explaning it. Various ensuing numerical simulations demonstrated that the instability in reality quickly forms into maintained turbulence, which transports angular momentum outwards at a rate that is in agreement with those required by observations (Brandenburg *et al.* 1995, Hawley, Gammie, and Balbus 1995; 1996, Stone *et al.* 1996, Armitage 1998).

In spite of the phenomenal success of the Shakura & Sunyaev model, there are additional classes of accretion disc models, with a specific goal to interpret the observations. It has been shown through observations of black hole sources, that the accretion disc emission is not primarily blackbody. Specifically, an enormous luminosity is emitted in hard X-rays as well. After the identification of the hard X-ray component, investigations are focussed to explain the origin of this component. Successful explanation of the origin of hard X-rays from accretion discs, remains as a test for the theoretical models of accretion disc. In the following, we decsribe the main classes of accretion models.

## 1.1 Models of Accretion Discs

In this segment, we focus on steady disc models. We start with the standard accretion disc model.

### 1.1.1 Standard Disc (Shakura-Sunyaev)

In the theory of accretion discs, one of the foundations is the model of optically thick, geometrically thin, gas pressure dominated discs formulated by Shakura (1972) and Shakura and Sunyaev (1973). In the very same year, the model was generalized to the relativistic version by Novikov and Thorne (1973). In the standard discs, the angular momentum is locally Keplerian at every radial coordinate and the disc has high radiative efficiency. This model depends on the presumption that the gas being accreted is efficiently cooled. As a result, all the energy discharged through viscous dissipation is radiated out locally. Consequently, the energy balance is

$$Q^{+}_{\rm vis} \sim Q^{-}_{\rm rad} \gg Q_{\rm adv}, \tag{1.1}$$

where $Q^{+}_{\rm vis}$ is the the viscous heating rate, $Q^{-}_{\rm rad}$ is the radiative cooling rate for optically thick flows and $Q_{\rm adv}$ is the advective cooling rate. Meanwhile, the temperature in the disc varies with the radius as (Shakura and Sunyaev 1973, Frank, King, and Raine 2002)

$$T(R) \propto R^{-3/4}, \tag{1.2}$$

where $T(R)$ is the temperature of the disc at radial coordinate $R$. This is the reason that the emission from the accretion disc around black hole is called multi-temperature black body. As a result, the accreting gas is considerably cooler ($\sim 10^7 K$) than the local virial temperature. This model successfully explains the high/soft states where the spectrum is thermally dominated. However, the inner region of the standard disc was found to be thermally unstable (Piran 1978) since the growth of heating rate exceeds the cooling rate in this region.

### 1.1.2 SLE

The works of Eardley, Lightman, and Shapiro (1975), Shapiro, Lightman, and Eardley (1976) were the first to examine black hole accretion discs at rather sub-Eddington accretion rate and concentrate on a category of optically thin solution where the disc is characterized with two-temperature (SLE). The temperature of the electron ($T_e$) in this model was observed to be lower than the ion temperature ($T_i$), where $T_i$ remained close to the virial temperature. This occured because the cooling of electrons was significantly more viable than the cooling of ions. Thus, because of high pressure kept up by hot ions, the disc continued to remain geometrically thick. The gas in this model is altogether more hotter than the local Shakura-Sunyaev solution. The gas being optically thin, cooling takes place via bremsstrahlung or by means of Comptonization of soft photons that are produced locally. The energy balance in this case satisfies equation (1.1) and the electrons in the plasma of the accretion disc achieve temperatures $T_e \sim 10^9 K$. The SLE solution successfully explains the hard X-ray emission from X-ray binaries and AGNs (e.g. Kusunose and Takahara 1985, Wandel and Liang 1991, Melia and Misra 1993).

Soon after the introduction of SLE model, it was realised that the disc is thermally unstable (Pringle 1976, Piran 1978). This is on account of the fact that the increase of ion temperature causes the disc to swell vertically, which lowers the cooling rate of ions through Coulomb interactions with electrons and prompts thermal runaway.

### 1.1.3 Slim Disc

When the mass accretion rate in the disc is equivalent to or exceeds the Eddington accretion rate, the accreting gas traps the photons and a significant portion of heat generated through viscosity is advected inwards along with the flow. At that point, the radiative cooling rate becomes noticeably lower than the viscous heating rate, in spite of the fact that disc luminosity reaches the Eddington limit. Due to inefficient radiative cooling, the energy balance becomes,

$$Q^{+}_{\rm vis} \sim Q_{\rm adv} \gg Q^{-}_{\rm rad}. \tag{1.3}$$

In the slim disc model, the flow is transonic and passes through an inner sonic radius, where the angular velocity is sub-Keplerian. Further, the flow is optically thick and radiation pressure dominated. Also, the inflow velocity is high in this model. Moreover, the disc is geometrically thick, where the height of the disc is similar to the radius and additionally the disc is moderately cool. The significant energy advection along with the flow stablizes the disc. This model was put forward by Abramowicz *et al.* (1988). The model was treated using full relativistic equations by Beloborodov (1998). Sądowski (2009) investigated the slim disc model around rotating black holes and examined their relevance for X-ray binaries.

### 1.1.4 ADAF

Similar to optically thick discs, there are accretion solutions where the disc is optically thin and the entropy advection is dominant. In such discs, the radiative cooling is ineffective and a large amount of accretion energy dissipated by viscosity is advected with the accreting gas as stored entropy. Solution of this category was first exhibited by Ichimaru (1977) and are termed advection dominated accretion flow (ADAF). Later Narayan and Popham (1993), Narayan and Yi (1994; 1995a;b), Abramowicz *et al.* (1995), Chen (1995) and Chen *et al.* (1995) carried out more detailed examination of the model and demonstrated that with the introduction of advection, the disc may be thermally stable. ADAF solutions are gas pressure supported and due to ineffective radiative cooling, the heating due to viscous dissipation is balanced by the radial advection of heat. Thus, equation (1.3) holds for the energy balance. Furthermore, in this model the electron temperature turns out to be high enough to account for the hard X-ray emission.

Since these optically thin solutions become non-existent above critical mass accretion rate, they can not account for the luminosity of the X-ray hard state when it exceeds 10% of the Eddington luminosity (Oda *et al.* 2007). Further, the hot accretion flow solutions of Narayan and Yi (1994; 1995a;b), Chen (1995) are described assuming "self similarity" and these solutions ignore the existence of event horizon, sonic radius, shocks[1], etc. Earlier, Chakrabarti (1989) and Abramowicz and Chakrabarti (1990) presented a similar version of ADAF solutions where self-consistent global accretion solutions were considered. These advective accretion solutions are transonic, inviscid and radiatively inefficient. Additionally, Chakrabarti and Titarchuk (1995) (hereafter CT95) and later Mandal and Chakrabarti (2005a;b) displayed two temperature accretion flow solutions around Schwarzschild black holes in the general "advective framework". These works by Chakrabarti and his collaborators have shown that shocks formation takes place in accretion discs around black holes, whenever possible. These shocks occur at a few tens of Schwarzschild radii. Many other workers have supported the existence of shocks in advective accretion flows around black holes (Gu and Lu 2001, Yuan *et al.* 2002b, Gu and Lu 2004, Le and Becker 2005, Gu and Lu 2006, Le and Becker 2007, Fukumura and Kazanas 2007). According to the CT95 model, the post-shock region in the low state is very hot. This hot post-shock region inverse Comptonizes the soft photons from the disc and results in the emission of hard spectrum. Moreover, in the low state, the CT95 model proposes that $\alpha$-parameter (ratio of the viscous stress-to-pressure) increases with disc accretion rate. Further, numerical simulations have revealed that shock instabilities in ADAF solutions around black holes have the potential in explaining the interesting phenomenon of quasi-periodic oscillations (QPOs) in the X-ray spectrum. For instance, Molteni, Sponholz, and Chakrabarti (1996b) and Chakrabarti, Acharyya, and Molteni (2004) showed that QPOs may originate when the cooling timescale in the post-shock region is roughly identical to the infall timescale.

---

[1] Shocks in accretion flows will be discussed in Section 1.6 of this Chapter.

## 1.2 Importance of the Magnetic Fields

The astrophysical environment has an abundance of magnetic fields and because of their inevitable existence in accretion discs around black holes, these frameworks display many intriguing highlights. It was Ichimaru (1977) who first considered the implication of magnetic fields on the transition from an optically thin hot disc to an optically thick cool disc. He contended that the magnetic pressure can not surpass the gas pressure in the disc, in view of the buoyant escape of magnetic flux from the disc. Shibata, Tajima, and Matsumoto (1990) carried out magnetohydrodynamic (MHD) simulations of magnetized accretion discs, where the magnetic flux buoyantly escapes from the disc due to Parker instability (Parker 1966). This simulation demonstrated that when magnetic pressure dominates in the disc, the disc can sustain itself in the low-$\beta$ state ($\beta = P_{\rm gas}/P_{\rm mag} < 1$, where $P_{\rm gas}$ is the gas pressure and $P_{\rm mag}$ is the magnetic pressure), since the growth rate of Parker instability decreases in the low-$\beta$ state as a result of magnetic tension. Further, in order to explain the fluctuations in X-ray emissions from Cyg X-1, neutron star X-ray binaries and AGNs, Mineshige, Kusnose, and Matsumoto (1995) proposed that the X-rays are emitted from accretion discs which are optically thin and dominated by magnetic pressure. These investigations eventually indicate the feasibility of magnetized accretion disc around black hole.

Often, the implications of large scale ordered magnetic fields in accretion disc studies are explored in two classes. In one classification, the global magnetic field is considered where both the poloidal and toroidal components of the ordered magnetic field are present (e.g., Hirose *et al.* 2004, Bu, Yuan, and Xie 2009, Faghei 2013). In the other classification, the accretion disc is threaded just by the toroidal field (e.g., Akizuki and Fukue 2006, Oda *et al.* 2007, Abbassi, Ghanbari, and Najjar 2008, Samadi, Abbassi, and Khajavi 2014, Mosallanezhad, Abbassi, and Beiranvand 2014). The latter one is legitimized since rotation dominates the accretion disc and we anticipate the magnetic fields in the disc to be predominantly toroidal in nature (Samadi, Abbassi, and Khajavi 2014). The generation of the toroidal magnetic field takes place in the disc as a result of the shear of the accretion flow (Pessah and Psaltis 2005, Mosallanezhad, Bu, and Yuan 2016). Numerical MHD simulations by Hirose *et al.* (2004) demonstrated that the toroidal component of the magnetic field governs the main body of the accretion flow, mainly in its inner region, whereas regions close to the poles are predominantly governed by a poloidal magnetic field chiefly resides in the vertical direction.

With regards to observational perspectives, magnetic fields have been proposed to play a vital role in the generation/collimation of jets in black hole systems. Extensive MHD simulations of accretion disc around rotating black holes has shown that windy hot materials (*i.e.* corona) escape from the interior region of the disc as jets (Koide *et al.* 2002, McKinney and Gammie 2004, De Villiers *et al.* 2005). In the region surrounding the horizon, rotation of the black hole drags the space-time geometry. As a result, the magnetic field lines are twisted and the rotational energy from the black hole can be extracted along the field lines. Blandford and Znajek (1977) demonstrated that this mechanism can possibly create truly relativistic jets. Moreover, Oda *et al.* (2010) reported the relevance of the magnetically supported disc and demonstrated that the model can account for the bright/hard state seen during the bright hard-to-soft transition of galactic black hole candidates. Such state transition in X-ray observations have been identified and reported by Gierliński and Newton (2006).

Magnetic fields in accretion discs play two vital roles. In one hand, they are responsible for transporting angular momentum allowing matter to accrete and on the other hand, dissipation of magnetic energy causes the heating of the accreting matter (Hirose, Krolik, and Stone 2006, Krolik, Hirose, and Blaes 2007). In the conventional model of accretion discs (e.g., Shakura and Sunyaev 1973), viscosity is treated phenomenologically using the $\alpha-$parameter. However, the precise physical process that permits satisfactory angular momentum transport to account for the activities of sources, for example, dwarf nova, which are powered by accretion, remains unclear. As noted earlier, the relevance of MRI in accretion discs was reported by Balbus and Hawley (1991). The magnetic turbulence is successfully excited and maintained through MRI. The Maxwell stress resulting from the turbulent magnetic fields adequately transports angular momentum allowing disc material to fall towards the black hole. The ratio ($\alpha_{\rm SS}$) of the Maxwell stress to the gas pressure in the quasi-steady state, which is related to the $\alpha$-parameter (ratio of the viscous stress-to-pressure) in the typical accretion disc models (Shakura and Sunyaev 1973), is $0.01 - 0.1$ (e.g., Hawley 2000, Hawley and Krolik 2001, Machida and Matsumoto 2003). Additionally, Pariev, Blackman, and Boldyrev (2003) obtained solutions of optically thick, magnetic pressure dominated disc, in the steady state, using the $\alpha-$prescription of viscosity, similar to the Shakura-Sunyaev approach. They proposed that the disc is supported vertically, fundamentally by magnetic pressure of turbulent magnetic fields. However, in this work, the formation of the low$-\beta$ discs was not explained and further the optically thin solution incorporating advective cooling was also not examined.

The findings delineated above have additionally been supported by numerical simulations. Machida, Nakamura, and Matsumoto (2006) carried out global three-dimensional MHD simulations of black hole accretion discs. The simulation was begun considering a torus which is radiatively inefficient and threaded by feeble toroidal magnetic fields. With the development of MRI, the formation of an optically thin, hot accretion disc occurs through the effective transport of angular momentum. When the density of the accretion disc surpasses the critical density, a cooling instability is triggered in the disc and gas pressure diminishes because of cooling. Consequently, disc contracts in vertical direction while endeavoring to almost conserve the toroidal magnetic flux. This leads the magnetic fields to intensify because of flux conservation and in due course, $P_{\rm mag}$ surpasses $P_{\rm gas}$. Thus, a magnetic pressure supported disc is formed. At the point when $P_{\rm mag}$ dominates, contraction of the disc in the vertical direction halts since the magnetic pressure holds the disc. At last, an optically thin, radiatively inefficient, hot, high-$\beta$ disc experiences transition to a low-$\beta$ disc, which is optically thin, radiatively efficient and cool, with the exception of in the plunging region (e.g., Machida, Nakamura, and Matsumoto 2006, Oda *et al.* 2010). Consequently in the thesis, we focus on accretion discs which are threaded by toroidal magnetic fields.

## 1.3 Treatment of gravitational field around a Black Hole

Due to the extreme gravity around a black hole, a full general relativistic treatment is ideal to investigate the properties of accretion flow around it. However, a full general relativistic treatment of the equations governing the transonic accretion flow around black holes is very tedious. It is especially the case when angular momentum, viscosity, magnetic fields, radiative processes etc. are included. In order to avoid the complexity of a full general relativistic treatment, pseudo-potentials are widely used to mimic the geometry of spacetime around stationary as well as rotating black holes. The utility in using a pseudo-potential lies in the fact that it allows us to get a qualitative understanding of the results that a full general relativistic treatment would reveal.

For the sake of generality, we consider a rotating black hole and to describe the spacetime around it, we use the spherical polar corodinates. Also, we choose a unit system as $G = M_{\rm BH} = c = 1$, where $G$ denotes the gravitational constant, $M_{\rm BH}$ is the central mass and $c$ represents the speed of light, respectively. The four distance between any two points around the rotating black hole (Kerr solution) is given by (Shapiro and Teukolsky 1983):

$$ds^2 = -d\tau^2 = -\left(1 - \frac{2r}{\Sigma}\right) dt^2 - \frac{4a_k r \sin^2\theta}{\Sigma} dt d\phi + \frac{\Sigma}{\Delta} dr^2 + \Sigma d\theta^2 + \left(r^2 + a_k^2 + \frac{2ra_k^2 \sin^2\theta}{\Sigma}\right) \sin^2\theta d\phi^2, \quad (1.4)$$

where the rotation of the black hole is in the $\phi$ direction, $a_k$ is the specific spin angular momentum of the central mass and

$$\Delta = r^2 - 2r + a_k^2, \qquad \Sigma = r^2 + a_k^2 \cos^2\theta.$$

For the case of a non-rotating black hole ($a_k = 0$), equation (1.4) reduces to the Schwarzschild metric. Further, we choose the plane of motion to be the equatorial plane ($\theta = \pi/2$ and sin $\theta = 1$). On the basis of these assumptions, equation (1.4) reduces to,

$$ds^2 = -d\tau^2 = -\left(1 - \frac{2}{r}\right) dt^2 + \left(1 - \frac{2}{r}\right)^{-1} dr^2 + r^2 d\phi^2. \quad (1.5)$$

To consider the motion of freely moving test particles, the Lagrangian is given by

$$2L = -\left(1 - \frac{2}{r}\right) \dot{t}^2 + \left(1 - \frac{2}{r}\right)^{-1} \dot{r}^2 + r^2 \dot{\phi}^2, \quad (1.6)$$

where $\dot{t} = dt/d\tau = u^t$ is the $t-$component of 4-momentum, and so on. Here, $\tau$ is the proper time.

Solving the geodesic equation gives,

$$u_\phi = r^2 \dot{\phi} = l = \text{constant of motion},$$

$$-u_t = \left(1 - \tfrac{2}{r}\right) \dot{t} = E = \text{constant of motion}.$$

Dividing equation (1.5) by $d\tau^2$ and using these constants of motion, one obtains

$$\frac{E^2}{\left(1 - \frac{2}{r}\right)} - \frac{(dr/d\tau)^2}{\left(1 - \frac{2}{r}\right)} - \frac{l^2}{r^2} = 1 \quad (1.7)$$

On rearranging the terms, this takes the form

$$\left(\frac{dr}{d\tau}\right)^2 = E^2 - V_{\rm eff}^2, \tag{1.8}$$

where

$$V_{\rm eff} = \left[\left(1 - \frac{2}{r}\right)\left(1 + \frac{l^2}{r^2}\right)\right]^{1/2} \tag{1.9}$$

Here, $V_{\rm eff}$ is the effective potential. The utility in defining an effective potential lies in the fact that through it the problem is reduced to particle motion in a force field in Newtonian mechanics.

In Newtonian physics, a test particle around a star feels the gravitational potential $\Psi_N$ given by,

$$\Psi_N = -\frac{1}{r}. \tag{1.10}$$

For Newtonian gravity, we define

$$V_{\rm Newt}(r) = 1 + \Psi_N + \frac{1}{2}\frac{l^2}{r^2}, \tag{1.11}$$

where $V_{\rm Newt}$ is the effective potential of a rotating gas with specific angular momentum $l$. The first term on the right-hand side corresponds to the rest mass energy while the second and third terms are respectively the gravitational potential and the centrifugal potential.

In Fig. 1.1 we have compared both $V_{\rm eff}$ and $V_{\rm Newt}$ for radial motion for a given value of angular momentum ($l = 4.2$). First, we notice that for large values of $r$, the relativistic potential is close to the Newtonian effective potential. However, as $r$ becomes small, the general relativistic correction becomes increasingly important. While the Newtonian theory gives an infinite centrifugal barrier, in the relativistic case, the barrier is of finite height.

From equation (1.9), we have, $V_{\rm eff} = 0$ at $r = r_g = 2$. $r_g = \frac{2GM}{c^2}$ is termed as the Schwarzschild radius.

The trajectories followed by particles entering a black holes are known as 'capture orbits'. The conditions to be satisfied for the occurence of stable circular orbits are: (a) $\frac{\delta V_{\rm eff}}{\delta r} = 0$ and, (b) $\frac{dr}{d\tau} = 0$. Using condition (a), we obtain the following equation:

$$r^2 - l^2 r + 3l^2 = 0. \tag{1.12}$$

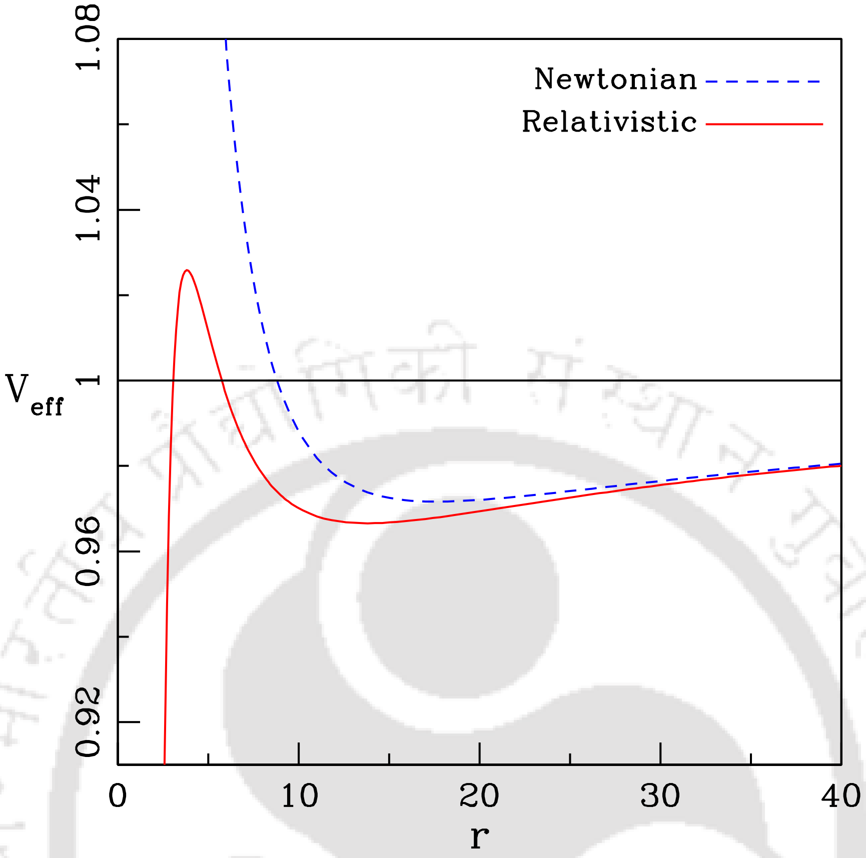

Fig. 1.1 Comparison of the general relativistic (solid) and Newtonian (dashed) effective potentials against $r$ for $l = 4.2$. The solid horizontal line for which $V_{\rm eff} = 1$ denotes the rest mass energy of particle falling into the black hole. See text for details.

Therefore, the real values of $r$ exist when $l \geq 2\sqrt{3}$, which indicates that $V_{\rm eff}$ has an extremum for $l \geq 2\sqrt{3}$. Putting $l = 2\sqrt{3}$ in equation (1.12), we obtain $r = 6$, which is the lowest value of $r$ above which a circular orbit is allowed. The circular orbit of radius $r = 6$ is known as the *marginally stable orbit* or the *last stable orbit* ($r_{\rm ms}$). When $r < r_{\rm ms}$, a particle can not go around a black hole in a circular orbit. When we impose the condition (b) in equation (1.8) and use equation (1.12), we obtain

$$E^2 = \frac{(r-2)^2}{r(r-3)}. \tag{1.13}$$

The specific Keplerian angular momentum curve is obtained as the locus of extrema of $V_{\rm eff}$. Therefore,

$$\lambda^2_{\rm Kep} = \left(-\frac{u_\phi}{u_t}\right)^2 = \frac{r^3}{(r-2)^2}. \tag{1.14}$$

Setting $r = 6$ and $l = 2\sqrt{3}$ in equation (1.9), we get

$$V_{\rm eff}(r_{\rm ms}) = \sqrt{\frac{8}{9}}. \tag{1.15}$$

Hence, the binding energy at $r_{\rm ms}$ is obtained as

$$E_{\rm bind} = 1 - V_{\rm eff}(r_{\rm ms}) = 1 - \sqrt{\frac{8}{9}} = 5.72\%. \tag{1.16}$$

When a black hole consumes a particle, $E_{\rm bind}$ amount of energy will be released in the form of radiation.

### 1.3.1 Pseudo-Newtonian Potential

We have seen that the Newtonian potential $\Psi_{\rm N} = -\frac{1}{r}$ is ineffective to account for black hole accretion, since it can not deliver accretion solution connecting the event horizon to infinity. In this thesis, we are interested to study the behaviour of particle motion outside the horizon (say, $r > 2r_g$) and thus we use *Paczyński-Wiita potential* (Paczyńsky and Wiita 1980) that satisfactorily describe the general relativistic effects. Paczyński-Wiita potential is a simple pseudo-Newtonian potential to describe behaviour of test particles moving in the vicinity of a black hole and is given as

$$\Psi_{\rm PN} = -\frac{1}{(r-2)}. \tag{1.17}$$

The effective potential to describe the orbital motion is given as

$$V^{\rm PN}_{\rm eff} = 1 + \frac{l^2}{2r^2} + \Psi_{\rm PN}, \tag{1.18}$$

where the rest mass energy '1' has been added to the pseudo-Newtonian potential in right-hand side. Utilizing the condition $\delta V^{\rm PN}_{\rm eff}/\delta r = 0$, one obtains

$$L^2_{\rm Kep} = \frac{r^3}{(r-2)^2}. \tag{1.19}$$

We find that $\Psi_{\rm PN}$ reproduces expression of the Keplerian angular momentum distribution (denoted by $L_{\rm Kep}$) same as in general relativity for the Schwarzschild spacetime. We have previously observed that $r_{\rm ms}$ is the location of the minima of the Keplerian

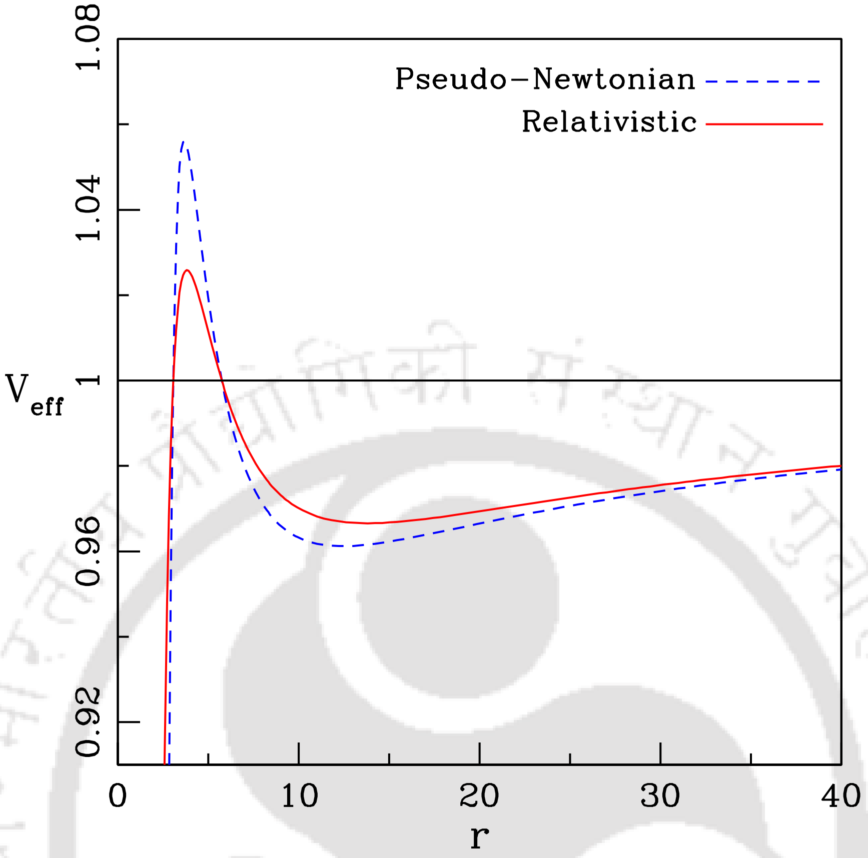

Fig. 1.2 Comparison of the general relativistic (solid) and pseudo-Newtonian (dashed) effective potentials against $r$ for $l = 4.2$. The solid horizontal line for which $V_{\rm eff} = 1$ denotes the rest mass energy of particle falling into the black hole. See text for details.

angular momentum. The minima of equation (1.19) is found to be $r_{\rm ms} = 6$. This further displays the excellence of the Paczyński-Wiita potential as it gives the correct location of the marginally stable orbit according to the Schwarzschild metric.

In Fig. 1.2 we have compared both $V_{\rm eff}$ and $V_{\rm eff}^{\rm PN}$ for radial motion for a given value of angular momentum ($l = 4.2$). It can be clearly seen that the pseudo-Newtonian potential mimics qualitatively the effects of space-time curvature on an orbiting body in a Newtonian description.

When general relativistic effects are approximated by the pseudo-Newtonian potential, the binding energy at $r_{\rm ms}$ is found to be

$$E_{\rm bind} = 1 - V_{\rm eff}^{\rm PN}(r_{\rm ms}) = 6.25\%. \tag{1.20}$$

Therefore, we find that the results from the pseudo-Newtonian approach are very satisfactory and the error is within a few per cents. In Chapter 2 and 3 of the thesis, we shall use $\Psi_{\rm PN}$ to take care of the general relativistic effects.

### 1.3.2 Pseudo-Kerr Potential

Over the years, there have been a number of attempts to extend the concept of employing a 'pseudo-Newtonian' approach even for rotating black holes in the Kerr geometry. It has been shown that it is indeed possible to approximate the salient features of the Kerr geometry by adopting an effective potential. In the following, we discuss the pseudo-Kerr effective potential proposed by Chakrabarti and Mondal (2006). This potential is expressed as,

$$\Psi_{\rm eff} = -\frac{\mathcal{Q} + \sqrt{\mathcal{Q}^2 - 4\mathcal{P}\mathcal{R}}}{2\mathcal{P}}, \tag{1.21}$$

where,

$$\mathcal{P} = \frac{\epsilon^2\lambda^2}{2x^2},$$

$$\mathcal{Q} = -1 + \frac{\epsilon^2\omega\lambda r^2}{x^2} + \frac{2a_k\lambda}{r^2 x},$$

$$\mathcal{R} = 1 - \frac{1}{r - x_0} + \frac{2a_k\omega}{x} + \frac{\epsilon^2\omega^2 r^4}{2x^2}.$$

Here, $x$ and $r$ represent respectively the cylindrical and spherical radial distance from the black hole when the black hole itself is regarded to be situated at the origin of the cylindrical coordinate system. Also, $\lambda$ indicates the specific angular momentum of the flow. In addition, $x_0 = 0.04 + 0.97a_k + 0.085a_k^2$, $\omega = 2a_k/(x^3 + a_k^2 x + 2a_k^2)$ and $\epsilon^2 = (x^2 - 2x + a_k^2)/(x^2 + a_k^2 + 2a_k^2/x)$, where, $\epsilon$ is the redshift factor and $a_k$ indicates the black hole rotation parameter defined as the specific spin angular momentum of the black hole. In the same spirit as for $\Psi_{\rm PN}$, the pseudo-Kerr effective potential proposed by Chakrabarti and Mondal (2006) is also an ad hoc prescription in the sense that this potential is not derived from the Kerr metric. As per Chakrabarti and Mondal (2006), the above potential reproduces characteristics of particle trajectories in the Kerr geometry very satisfactorily when the Kerr parameter lies in the range $-1 \lesssim a_k \lesssim 0.8$.

This potential has numerous applications. Firstly, the use of this potential allows us to handle the computations of accretion flow properties around rotating black holes very easily. As has been the case with $\Psi_{\rm PN}$ potential, a complete analysis of the accretion flow can be done with the pseudo-Kerr potential including various dissipative processes and magnetic fields. Secondly, numerical simulations become more feasible and time-dependent properties can be investigated easily by simply replacing the Newtonial potential with the pseudo-Kerr one. Thirdly, shocks and non-linear flow properties like quasi-periodic oscillations of X-rays can also be examined using this potential. Consequently, the above potential has been adopted in Chapter 4 to mimic the spacetime geometry around a rotating black hole.

## 1.4 Radiative processes

During accretion, a part of the gravitational energy of the flow is emitted as radiation. This radiation ranges throughout the whole of the electromagnetic spectrum and extends from radio to $\gamma-$rays. The emission of radiation in various frequency-bands is determined fundamentally by the nature of the medium and the physical mechanisms related to the system. In case of accretion discs around black holes, the radiation is primarily emitted in the X-ray band. Below we discuss the emission and absorption mechanisms that have been used in the thesis.

(i) **Free-free emission (or thermal bremsstrahlung)**: When an electron in a plasma moves in the Coulomb field of the massive ions, it accelerates or decelerates and consequently emits a photon. This mechanism is known as bremsstrahlung and is also called free-free emission. We can further assume that the plasma is optically thin (implying that the radiation field is not in equilibrium), the electrons and ions in the plasma are in thermal equilibrium at the temperature $T$ and also consider nonrelativistic particle speeds. The radiation from such a plasma has a typical shape of continuous spectrum that is decided just by the temperature. This specific sort of bremsstrahlung process is known as the thermal bremsstrahlung. The emission coefficient (in erg cm$^{-3}$ s$^{-1}$ Hz$^{-1}$) is given by (Shapiro and Teukolsky 1983),

$$4\pi j_\nu^{\rm ff} = 6.8 \times 10^{-38} \frac{g_{\rm ff} Z^2 N_i N_e}{T^{1/2}} \exp(\frac{-h\nu}{k_B T}), \tag{1.22}$$

where $N_e$ and $N_i$ are electron and ion number densities, $Z$ is the atomic number, $g_{\rm ff}$ is the Gaunt factor, $\nu$ is the frequency and $k_B$ is the Boltzmann's constant. To obtain the total amount of energy emitted by free-free transitions per cm$^3$ per sec, equation (1.22) is integrated over all frequency as

$$\Lambda_{\rm ff} = 1.42 \times 10^{-27} Z^2 N_i N_e T^{1/2}\ \bar{g}_{\rm ff}\ {\rm erg\ cm^{-3}\ s^{-1}},$$

where $\bar{g}_{\rm ff} \sim 1$ is the mean Gaunt factor. For the pure hydrogen gas, we have $Z = 1$ and $N_e = N_i$. The following relation holds,

$$N_i Z = \frac{\rho}{m_p + m_e} \approx \frac{\rho}{m_p},$$

where $\rho$ is the density, $m_p$ is the mass of proton and $m_e$ is the electron mass. Thus we finally have,

$$\Lambda_{\rm ff} = 1.42 \times 10^{-27} \frac{\rho^2}{m_p^2} T^{1/2} \ {\rm erg\ cm^{-3}\ s^{-1}}.$$

(ii) **Synchrotron emission**: When electrons in a plasma spiral in a magnetic field with relativistic velocities ($v \sim c$), the radiation emitted by this procedure is called synchrotron radiation. We consider an electron of charge $e$ moving with speed $\vec{v}$ in a magnetic field $\vec{B}$. In the momentary rest frame of the electron, the force due to magnetic field $(e/c)[\vec{v} \times \vec{B}]$ is zero; however there will be a non-zero value of electric field of magnitude $E' = (v/c)\gamma B$. This elecrtic field $E'$ is caused due to the magnetic field in the lab frame and it will induce an acceleration in the electron of magnitude $a' = (eE'/m_e)$. Due to this acceleration, the electron will emit energy. The total amount of energy emitted by relativistic electrons gyrating around magnetic field lines per cm$^3$ per sec is given by (Shapiro and Teukolsky 1983),

$$\Lambda_{\rm syn} = \frac{16}{3} \frac{e^2}{c} \left(\frac{eB}{m_e c}\right)^2 \left(\frac{kT_e}{m_e c^2}\right)^2 N_e \ {\rm erg\ cm^{-3} s^{-1}},$$

where $T_e$ is the electron temperature in the plasma. Here, $N_e = \frac{f_e \rho}{m_p}$, where $f_e$ is the number of free electrons per baryon. For complete ionization of hydrogen gas, $f_e = 1$ and we have,

$$\Lambda_{\rm syn} = \frac{16}{3} \frac{e^2}{c} \left(\frac{eB}{m_e c}\right)^2 \left(\frac{kT_e}{m_e c^2}\right)^2 \frac{\rho}{m_p} \ {\rm erg\ cm^{-3} s^{-1}}.$$

(iii) **Inverse Compton emission**: Another important mechanism by which high energy photons can be created is the scattering of photons by hot electrons which are highly relativistic. In such a mechanism, the low energy photons gain a large amount of energy from the electrons and get converted into high energy photons. This mechanism is named as *inverse Compton emission* and it is very important in high energy astrophysics. In general, an astrophysical flow could generate soft photons due to various radiative processes, namely bremsstrahlung, synchrotron etc.

Global solutions of transonic accretion flows around black holes in both the weak and strong viscosity limits (Chakrabarti 1989; 1990a;b) have revealed that, the advective flows around black holes in reality have two components. The viscous Keplerian disc lies in the equatorial plane and this Keplerian disc is flanked by the low viscosity sub-Keplerian flow both on the top and the bottom. The inner part of this sub-Keplerian flow slows down due to the centrifugal barrier and becomes hotter. This hot, inner puffed up region is the Compton cloud. Soft photons originating from the Keplerian disc are intercepted by the Compton cloud and are re-radiated after suffering multiple scatterings. On the basis of the ratio of the Keplerian disc accretion rate ($\dot{M}_d$) to the sub-Keplerian halo rate ($\dot{M}_h$), the electrons in the Compton cloud may lose energy (inverse Compton scattering) or gain energy (Compton scattering). If the temperature of the electron cloud increases, the accretion disc is in the hard state, while if the temperature of the electron cloud decreases by losing energy to the photons, the disc goes to the softer state. Hence, a power-law hard photon component is a signature of the hard state of the black hole candidate. Thus, the inverse Compton emission mechanism plays a very important role in deciding the spectral state of black hole candidates.

## 1.5 Concept of Optical Depth

When photons propagate through a medium and if the ray traverses a distance $dx$ through the medium, then the *optical depth* $\tau$ is defined as,

$$d\tau = \alpha_\nu dx,$$

where $\alpha_\nu$ is the absorption coefficient. Quantities with subscript $\nu$ are frequency dependent. Hence, the optical depth along the ray path between $x_0$ and $x$ becomes

$$\tau_\nu = \int_{x_0}^{x} \alpha_\nu(x')dx'.$$

A medium is known as optically thick if the optical depth $\tau_\nu \gg 1$ along a ray path while propagation through the medium. On the other hand, a medium is known as optically thin, if $\tau_\nu \ll 1$ for a ray path through it. Using the optical depth $\tau_\nu$, we can calculate the variation of the specific intensity along the ray path as

$$I_\nu(\tau_\nu) = I_\nu(0)e^{-\tau_\nu},$$

provided there is no emission from the medium itself. This relation reveals that when the medium is optically thick, it will extinguish the light from a source propagating through it. On the other hand, if the medium is optically thin, it does not extinguish the light substantially. Hence for a given frequency of electromagnetic radiation under consideration, the term optically thick indicates that the medium is opaque, while the term optically thin indicates that the medium is transparent.

In case of an accretion disc, the scattering optical depth given by,

$$\tau_{\rm es} = \kappa_{\rm es}\rho h,$$

where $\kappa_{\rm es} = 0.38\ {\rm cm}^2\ {\rm g}^{-1}$ is the electron scattering opacity, $\rho$ is the density and $h$ is the half-thickness of the disc. The effective optical depth of the disc in the vertical direction is given by (Rajesh and Mukhopadhyay 2010),

$$\tau_{\rm eff} = \sqrt{\tau_{\rm es}\tau_{\rm abs}}.$$

Here, $\tau_{\rm abs}$ denotes the absorption effect arising due to different radiative processes and is given by (Rajesh and Mukhopadhyay 2010),

$$\tau_{\rm abs} = \frac{hq_{\rm abs}}{4\sigma T_e^4},$$

where $\sigma$ is the Stefan-Boltzmann constant, $T_e$ is the electron temperature in the plasma and $q_{\rm abs}$ is the total emissivity due to all the non-thermal processes involved.

## 1.6 Shocks in Accretion Flow

Flows containing the propagation of shock waves are frequently encountered in astrophysical systems. Shocks emerge in a number of settings in which there is a supersonic flow of gas with respect to a solid barrier. In the following discussion on shocks, we follow the treatment of Clarke and Carswell (2007) and Frank, King, and Raine (2002).

Perturbations in a fluid consistently spread at the speed of sound ($a$) with respect to the fluid. The ratio of the flow speed ($v$) to the sound speed is called the Mach number ($M = v/a$). When there is a barrier in a supersonic flow, it prevents the perturbations to spread upstream from the barrier, i.e. the flow is unable to adapt to the existence of the obstruction as there is no chance to get a signal propagated toward that direction. In this way, the flow remains undisturbed until the point when it comes to the obstruction, and there, its properties undergo a discontinuous change in a *shock*.

On the other hand, a subsonic flow can adapt to the existence of an obstruction as the disturbances caused can be imparted upstream through the flow.

A shock shows itself as a border between two zones of the flow where the conditions undergo a discontinuous change. As in case of any fluid, the typical conditions like the conservation of matter, momentum and energy equations should apply here. So to deal with the flow through the shock, these conditions should simply be translated as they apply over the shock front. It is suitable to do this in the frame in which the shock front is at rest.

As the shock is very thin, we can view it as locally plane. Again, since the fluid moves through the shock very rapidly, changes in the fluid conditions cannot influence the particulars of the transition on the two sides of the shock front, so we can respect the flow into and out of the shock as steady.

Taking the normal to the shock (*i.e.*, surface of discontinuity) in the $x$ direction, the equation of continuity becomes (Frank, King, and Raine 2002),

$$\frac{\partial}{\partial x}(\rho v_x) = 0, \tag{1.23}$$

where $\rho$ is the density. Integrating this over a layer of thickness $dx$ around the shock, we get

$$\rho v_x|_{\frac{dx}{2}} - \rho v_x|_{-\frac{dx}{2}} = 0. \tag{1.24}$$

This implies that for an infinitesimal layer $dx$, $\rho v_x$ must be the same on both sides of the shock. So

$$\rho_+ v_+ = \rho_- v_- = J. \tag{1.25}$$

Here, the quantities with subscripts '$-$' and '$+$' refer to values before and after the shock, respectively. It is clear that, here the conserved quantity $J = \rho v$ is the mass flux.

Similarly, we deal with the momentum equation. In the steady state, the momentum equation can be written as (Frank, King, and Raine 2002),

$$\rho(\mathbf{v} \cdot \nabla)\mathbf{v} = -\nabla P_{\rm tot} + \mathbf{f}. \tag{1.26}$$

where $P_{\rm tot}$ is the total pressure in the flow and $\mathbf{f}(= -\rho\nabla\psi + \frac{(\mathbf{B}\cdot\nabla)\mathbf{B}}{4\pi})$ represents the force density acting on the fluid. Here, $\psi$ is the gravitational potential and $\mathbf{B}$ is the magnetic field. Thus, we have for the $x$ component

$$\rho v_x \frac{\partial v_x}{\partial x} + \frac{\partial P_{\rm tot}}{\partial x} = f_x, \tag{1.27}$$

or

$$\frac{\partial}{\partial x}(P_{\rm tot} + \rho v_x^2) = f_x, \tag{1.28}$$

where $f_x$ is the force density in the $x$ direction. Integrating over the small region $dx$ gives

$$(P_{\rm tot} + \rho v_x^2)|_{\frac{dx}{2}} - (P_{\rm tot} + \rho v_x^2)|_{-\frac{dx}{2}} = \lim_{dx \to 0} \int_{-\frac{dx}{2}}^{+\frac{dx}{2}} f_x dx = 0, \tag{1.29}$$

since $f_x$ is finite. Consequently,

$$P_{\rm tot+} + \rho_+ v_+^2 = P_{\rm tot-} + \rho_- v_-^2, \tag{1.30}$$

*i.e.*, the sum of the total and ram pressures across the boundary remains constant.

The energy equation is given by (Clarke and Carswell 2007),

$$\frac{\partial E}{\partial t} + \nabla \cdot [(E + p_{\rm gas})\mathbf{v}] = -\rho \dot{Q}_{\rm cool} + \rho \frac{\partial \psi}{\partial t}, \tag{1.31}$$

where, $E$ is defined as the total energy per unit volume, $p_{\rm gas}$ is the gas pressure and $\dot{Q}_{\rm cool}$ (per kilogram) is defined as a cooling function. $E$ can be explicitly written as,

$$E = \rho \left( \frac{1}{2} v^2 + \psi_{\rm eff} + \epsilon + \frac{B^2}{4\pi\rho} \right),$$

where the terms on the right-hand side are recognisable as the kinetic energy, effective potential energy, internal energy and magnetic energy.

Now, we make some assumptions about the nature of cooling in the shocked gas. We assume that the gas cannot cool, i.e. that the shock is adiabatic (so $\dot{Q}_{\rm cool} = 0$). For an adiabatic shock and in the steady state, we obtain from equation (1.31) that $(E + p_{\rm gas})v$ is the same on both sides of the shock, and we have across the shock front

$$\left[ \frac{1}{2} v^2 + \psi_{\rm eff} + \epsilon + \frac{B^2}{4\pi\rho} + \frac{p_{\rm gas}}{\rho} \right] \rho v = \text{constant}. \tag{1.32}$$

We know from equation (1.25) that $\rho v$ is constant across the shock, and $\psi_{\rm eff}$ is a continuous function at the shock. So,

$$\frac{1}{2}v_+^2 + \epsilon_+ + \frac{B_+^2}{4\pi\rho_+} + \frac{p_{\rm gas+}}{\rho_+} = \frac{1}{2}v_-^2 + \epsilon_- + \frac{B_-^2}{4\pi\rho_-} + \frac{p_{\rm gas-}}{\rho_-}. \tag{1.33}$$

Using the relation, $\epsilon = \frac{1}{(\gamma-1)}\frac{p_{\rm gas}}{\rho}$, the above equation can be written as,

$$\frac{1}{2}v_+^2 + \frac{\gamma}{(\gamma-1)}\frac{p_{\rm gas+}}{\rho_+} + \frac{B_+^2}{4\pi\rho_+} = \frac{1}{2}v_-^2 + \frac{\gamma}{(\gamma-1)}\frac{p_{\rm gas-}}{\rho_-} + \frac{B_-^2}{4\pi\rho_-}. \tag{1.34}$$

The three conditions 1.25, 1.30 and 1.34 are the Rankine–Hugoniot relations (Landau & Lifshitz 1959, Clarke and Carswell 2007, Frank, King, and Raine 2002). The first is essentially mass conservation, the second communicates that a shock represents a conversion of ram pressure to total pressure, and the third the transformation of kinetic energy and magnetic energy into enthalpy. In principle, a shock changes over an ordered flow upstream into a disordered (i.e. hot) flow downstream.

In addition, for a thin shock in a magnetized accretion flow, we consider that the radial advection rate of the toroidal magnetic flux ($\dot{\Phi}$) is continuous across the shock,

$$\dot{\Phi}_+ = \dot{\Phi}_-. \tag{1.35}$$

## 1.7 Over view of the work

In this thesis, we have extensively investigated steady solutions of optically thin accretion discs considering that the magnetic fields inside the disc are turbulent and dominated by the azimuthal component. The consequences of magnetic fields in the disc have been taken into account by considering the total pressure as the sum of the gas pressure and the magnetic pressure: $P_{\rm tot} = p_{\rm gas} + p_{\rm mag}$, $p_{\rm mag} = B^2/8\pi$, where, $P_{\rm tot}$ is the total pressure, $p_{\rm gas}$ is the gas pressure, $p_{\rm mag}$ is the magnetic pressure and $B$ is the strength of magnetic field in the disc, respectively. The vertical structure of the disc is supported against gravity through the combined effects of gas and magnetic pressure. Hence, following the conventional $\alpha$-viscosity prescription of Shakura and Sunyaev (1973), the angular momentum transport in the disc equatorial plane would also be enhanced as the magnetic pressure contributes to the total pressure. Furthermore, to simulate the general relativistic effects in case of stationary or rotating black holes, we make use of appropriate pseudo-potentials. In the absence of any coupling between ions and electrons, we have approximated the electron temperature as, $T_e = (\sqrt{m_e/m_p})T_p$ (Chattopadhyay and Chakrabarti 2002), where $m_e$ is the electron mass, $m_p$ is the ion mass and $T_p$ is the ion temperature, respectively. This assumption is important since the inner part of the disc is very hot and the radiative cooling time of relativistic electrons are shorter than the non-relativistic ions, thus the accreting plasma is expected to be characterized by two temperature flow. Moreover, in the thesis, we consider that the heating of the flow takes place due to the thermalization of magnetic energy through the magnetic reconnection mechanism. Also, the cooling of the flow is governed by the various radiative processes, such as, bremsstrahlung, synchrotron or Comptonization of bremsstrahlung photons. Towards this, we consider a set of magnetohydrodynamic equations in the steady state to model the dissipative accretion flow in the disc. With this, we self-consistently calculate the global accretion solutions including shock waves and investigate the shock properties in terms of the flow parameters. The presentation of thesis is organized in five chapters and the layout is given as per the following:

- **Chapter 1** introduces the reader with various accretion disc models around black holes. The utility and shortcomings of the different models are dealt with. In particular, the role of magnetic fields in such accretion discs around black holes is highlighted and their various aspects are discussed.

- In **Chapter 2**, we study the global structure of optically thin, advection dominated, magnetized accretion flow around stationary black holes. We consider the magnetic field to be turbulent in nature and dominated by the toroidal component. The effect of spacetime geometry around the black hole is mimicked by employing the pseudo-Newtonian potential introduced by Paczyńsky and Wiita (1980). In this chapter, we focus on supermassive black hole sources. For these systems, the magnetic field is expected to be low because of large size of the accretion disc. Thus, we have considered Comptonization of the bremsstrahlung radiation to be the prospective cooling mechanism in the flow (Das and Chakrabarti 2004). With this, we obtain the global transonic accretion solutions for dissipative magnetized flows and show that rotating magnetized accretion flow experiences virtual barrier around black hole due to centrifugal repulsion that can trigger the discontinuous transition of the flow variables in the form of shock waves. We examine the properties of the shock waves and find that the dynamics of the post-shock corona (PSC) is controlled by the flow parameters, namely, viscosity, cooling efficiency factor ($\xi$) and strength of the magnetic field, respectively. We separate the effective region of the parameter space for standing shock and observe that shock can form for wide range of flow parameters. We obtain the critical viscosity parameter that allows global accretion solutions including shocks. We estimate the energy dissipation at the PSC from where a part of the accreting matter can deflect as outflows and jets. We compute the maximum energy that could be extracted from the PSC. This is compared against the observed radio luminosity values for several supermassive black hole sources and close agreement is seen. Finally, the observational implications of the analysis are discussed.

- In **Chapter 3**, we carry out investigations of the global structure of the advection dominated accretion flow around non-rotating stellar mass black holes. For such flows, synchrotron cooling dominates over the bremsstrahlung process since accretion discs around stellar mass black holes are threaded by significant magnetic fields. Thus the contribution of bremsstrahlung radiation is neglected in this Chapter. We consider the accretion disc to be threaded by toroidal magnetic fields and general relativistic effects are simulated using the pseudo-Newtonian potential (Paczyńsky and Wiita 1980). With this, we obtain the global transonic accretion solutions by exploring the variety of boundary conditions and dissipation parameters, namely accretion rate ($\dot{m}$) and viscosity ($\alpha_B$). Depending on the initial parameters, steady state accretion flows are shown to possess centrifugally supported shock waves. These global shock solutions exist even when the level of dissipation is relatively high. We study the properties of shock waves and observe that the dynamics of the PSC is regulated by the flow parameters. Interestingly, we find that shock solution disappears completely when the dissipation parameters exceed their critical values. We calculate the critical value of viscosity parameter ($\alpha_B^{\rm cri}$) adopting the canonical values of adiabatic indices as $\gamma = 4/3$ (ultra-relativistic) and 1.5 (semi-non-relativistic) and find that in the gas pressure dominated domain, $\alpha_B^{\rm cri} \sim 0.4$ for $\gamma = 4/3$ and $\alpha_B^{\rm cri} \sim 0.27$ for $\gamma = 1.5$, respectively. We further show that global shock solutions are relatively more luminous compared to the shock free solutions. Also, we have calculated the synchrotron spectra for shocked solutions. When the shock is considered to be dissipative in nature, it would have an important implication as the available energy at PSC can be utilized to power the outflowing matter escaped from PSC. Towards this, we calculate the maximum shock luminosity and discuss the observational implication of our present formalism.

- In **Chapter 4**, we extend the formulations of Chapter 3 to include the effect of rotation of the black hole and explore the dynamical structure of an advection dominated, magnetized accretion flow around it. Since most stars rotate, it is very crucial to consider that most (if not all) of the black holes should have non-zero values of spin angular momentum ($a_k \neq 0$, where $a_k$ is the Kerr parameter). The spin of the black hole will drastically affect the spacetime geometry around it and hence will have significant consequences on the accretion flow properties. In order to mimic the geometry of spacetime around a rotating black hole, we use the pseudo-Kerr potential introduced by Chakrabarti and Mondal (2006). This potential successfully mimics the geometry of spacetime around a rotating black hole with spin parameter as high as $a_k \lesssim 0.8$. In this Chapter, we consider the accretion disc to be threaded by toroidal magnetic fields and employ synchrotron cooling mechanism to be active in the flow. We obtained the global transonic accretion solutions with shocks and show that the rotation of the black hole significantly affects the shock properties and the dynamics of the PSC. Furthermore, shock dynamics is also affected by the flow parameters such as viscosity ($\alpha_B$), accretion rate ($\dot{m}$) and strength of the magnetic fields. The shock properties are investigated against these flow parameters. For a rotating magnetized accretion flow around a spinning black hole, we classify the parameter space spanned by critical accretion rate ($\dot{m}^{\rm cri}$) and viscosity ($\alpha_B$) into regions that allow closed accretion solution (passing through the inner sonic point only) and standing accretion shocks. We further show that for a rotating black hole, accretion solutions with shock exist for a wide range of inflow parameters. We compute the maximum energy that could be extracted from the PSC and study its variation with magnetic parameter $\beta$ and spin of the black hole.
- **Chapter 5** concludes with a summary of the main results of the thesis. The importance of these results along with the possible extensions are discussed thereafter.

# Chapter 2

# Magnetized accretion flows in presence of bremsstrahlung cooling process

When flow accretes onto a neutron star or a white dwarf, it can be transonic or entirely subsonic.[1] However, when the central object is a black hole, the accretion flow must necessarily be transonic, since the flow velocity approaches the speed of light in the vicinity of the event horizon and is negligible compared to the local sound speed far away from the hole. Thus the flow must contain at least one sonic point. On the other hand, it was shown by Liang and Thompson (1980), Abramowicz and Zurek (1981), Abramowicz and Chakrabarti (1990) that the accretion flow around a black hole can contain multiple sonic points as well. As a result, shock formation can occur in the accretion flow whenever possible (Fukue 1987, Chakrabarti 1989, Lu and Yuan 1998, Lu, Gu, and Yuan 1999, Fukumura and Tsuruta 2004). Due to shock transition, a supersonic flow undergoes a transition to a subsonic branch where the temperature and density of post-shock flow have a catastrophic rise. In case of black hole accretion flows, shocks are triggered as a result of the virtual barrier created by the centrifugal repulsion (Chakrabarti 1997, Nobuta and Hanawa 1999, Okuda *et al.* 2004). In the literature, the shock induced global accretion solutions and its implications around black hole have been widely examined by the various groups of workers (Fukue 1987, Chakrabarti 1989; 1996b, Lu, Gu, and Yuan 1999, Gu and Lu 2001, Das *et al.* 2001b, Gu and Lu 2004, Fukumura and Tsuruta 2004, Chakrabarti and Das 2004, Mondal

---

[1] The contents of this chapter are published in Sarkar B., Das S., 2016, MNRAS, 461, 190.

and Chakrabarti 2006, Das 2007, Becker, Das, and Le 2008, Das, Becker, and Le 2009, Das, Chakrabarti, and Mondal 2010, Aktar, Das, and Nandi 2015, Aktar *et al.* 2017, Dihingia, Das, and Mandal 2018). Beside this, the presence of shock in accretion flow has been investigated in the numerical front considering hydrodynamic (Chakrabarti and Molteni 1993, Molteni, Lanzafame, and Chakrabarti 1994, Ryu, Chakrabarti, and Molteni 1997, Okuda 2014, Okuda and Das 2015, Suková and Janiuk 2015, Suková, Charzyński, and Janiuk 2017) as well as through magnetohydrodynamic simulations (Nishikawa *et al.* 2005, Takahashi *et al.* 2006, Fukumura, Takahashi, and Tsuruta 2007, Fukumura *et al.* 2016).

Shocks in accretion flow are of huge astrophysical significance. For instance, when the cooling timescale in the flow is roughly identical to the infall timescale, the shock begins to show steady oscillations (Molteni, Sponholz, and Chakrabarti 1996b, Ryu, Chakrabarti, and Molteni 1997, Garain, Ghosh, and Chakrabarti 2014). Such shocked accretion flows have been observed to be imperative since they are able to explain an intriguing astrophysical phenomenon called the quasi-periodic oscillations (QPOs) (Chakrabarti and Manickam 2000, Nandi *et al.* 2001a;b, Das *et al.* 2014, Das and Aktar 2015). Further, the post-shock region (equivalently post-shock corona, hereafter PSC) behaves like a Compton cloud which inverse Comptonizes the soft photons from the outer region of the disc, thereby generating the spectral features of black hole sources (Chakrabarti and Titarchuk 1995, Mandal and Chakrabarti 2005a, Chakrabarti and Mandal 2006). Furthermore, PSC causes the generation of jets and outflows that are linked with the spectral states (Chakrabarti 1999, Chattopadhyay and Chakrabarti 2011, Garain, Ghosh, and Chakrabarti 2012, Kumar, Chattopadhyay, and Mandal 2014, Aktar, Das, and Nandi 2015, Aktar *et al.* 2017). All these findings evidently indicate that the magnetohydrodynamic characteristics of the PSC is expected to decide the spectral and timing properties and outflow rates in black hole candidates.

In a number of accretion disc models around black holes, chaotic or random magnetic fields are considered to obtain the transonic global accretion solutions (Narayan and Yi 1995b, Yuan 2001, Mandal and Chakrabarti 2005b, Das 2007, Rajesh and Mukhopadhyay 2010, Xie and Yuan 2012). However, it has been demonstrated through numerical simulations that the inner region of accretion disc probably contains large scale toroidal magnetic fields, while on the small scale, magnetic fields are stochastic in nature (Machida, Hayashi, and Matsumoto 2000, Hirose *et al.* 2004). The influence of such a field has been investigated through self-similar approach (Akizuki and Fukue 2006, Abbassi, Ghanbari, and Najjar 2008, Bu, Yuan, and Xie 2009, Samadi, Abbassi, and Khajavi 2014, Mosallanezhad, Abbassi, and Beiranvand 2014) as well as through global solutions (Oda *et al.* 2007; 2012).

Oda *et al.* (2007) presented a new type of optically thin solution of steady state accretion flow around a black hole based on the outcomes from three-dimensional MHD simulations. When mass accretion rate surpasses the limit for the outset of thermal instability, they showed that magnetic pressure dominates in the flow and supports the disc. Thus, a thermally and viscously stable low$-\beta$ branch emerges. The findings from numerical simulation of Machida, Nakamura, and Matsumoto (2006) were corroborated by these solutions. The accretion disc luminosity on this branch can be greater than 20% of the Eddington luminosity. Besides, the mean disc temperature estimated from the model stays below that of the ADAF/RIAF discs and shows anticorrelation with the mass accretion rate. Subsequently, they came to the conclusion that optically thin low$-\beta$ discs can account for the bright hard state.

In the global accretion solutions studied by Oda *et al.* (2007; 2012), the flow passes through a single sonic point only. They ignored the possibility of accretion solutions passing through multiple sonic points. Based on these considerations, in the present Chapter, we show that a magnetized accretion flow indeed passes through more than one sonic point and may harbour shock waves whenever possible. In view of this, we present the model of an optically thin, advection dominated, magnetized accretion flow around a Schwarzschild black hole. The nature of magnetic fields in the disc is considered as turbulent and dominated by the toroidal component. We consider the set of magneto-hydrodynamic equations describing the accretion flows in the disc and treat Comptonization of bremsstrahlung radiation to be the dominant cooling mechanism active in the flow. For simplicity, the space-time geometry around a Schwarzschild black hole is approximated by adopting the pseudo-Newtonian potential (Paczyńsky and Wiita 1980). We solve the governing equations and show that the rotating magnetized accretion flows harbours shock waves which are triggered due to the centrifgual repulsion. We investigate the dynamical behaviour of the PSC and the shock properties in terms of the flow parameters. We show that the shock solutions are not isolated solutions, rather they form in a wide region of the flow parameters. We determine the critical viscosity parameter that permits the formation of standing shock in the accretion flow. Subsequently, we consider dissipative shocks, where a part of flow energy gets dissipated from the disc during the shock transition. Next, we estimate the maximum energy that is possible to be extracted form the PSC and show that this can successfully explain the observed radio luminosities for several supermassive black hole sources. Finally, we discuss the observational implications of our formalism.

In the following, we first present the model assumptions and governing equations and the methodology to solve them. In Section 2.2, we present the shocked and shock free global accretion solutions, the properties of shock and shock parameter space. Next, in Section 2.3, we compute the maximum shock luminosity from our model and compare it for several supermassive black hole sources. The concluding remarks are presented in Section 2.4.

## 2.1 Model for the accretion flow

Let us first consider the structure of magnetic fields in the disc. In this regard, we rely on the results obtained from both global and local numerical simulations of MHD accretion flow around black holes. It is known through these simulations that magnetic fields in the accretion disc are turbulent and fundamentally dominated by the azimuthal component (Hirose, Krolik, and Stone 2006, Machida, Nakamura, and Matsumoto 2006, Johansen and Levin 2008). Following the results of these simulations, we consider the magnetic fields as a combination of mean fields, denoted by $\mathbf{B} = (0, <B_\phi>, 0)$, and the fluctuating fields, denoted by $\delta\mathbf{B} = (\delta B_r, \delta B_\phi, \delta B_z)$. Here, we express the azimuthal average of any quantity by '<>'. Upon azimuthally averaging, we consider the fluctuating components to vanish ($<\delta\mathbf{B}>= 0$). Besides, the radial and vertical components of the magnetic field become negligible when compared against the azimuthal component, $|<B_\phi> + \delta B_\phi| \gg |\delta B_r|$ and $|\delta B_z|$. Eventually, the azimuthally averaged form of the magnetic field is obtained as $<\mathbf{B}>=<B_\phi> \hat{\phi}$ (Oda *et al.* 2007).

### 2.1.1 Governing Equations

Throughout this Chapter, we use a unit system as $2G = M_{\rm BH} = c = 1$, where $G$, $M_{\rm BH}$ and $c$ are the gravitational constant, mass of the black hole and the speed of light, respectively. In this unit system, length, velocity, time and angular momentum are expressed in unit of $r_g = 2GM_{\rm BH}/c^2$, $c$, $2GM_{\rm BH}/c^3$, and $2GM_{\rm BH}/c$, respectively. Here, we assume that the matter accretes through the equatorial plane of a Schwarzschild black hole. We use cylindrical polar coordinates $(x, \phi, z)$ with the black hole placed at the origin and the disc lies in the $z = 0$ plane. We adopt the pseudo-Newtonian potential (Paczyńsky and Wiita 1980) to describe the space-time geometry around the black hole and is given by,

$$\Phi = -\frac{1}{2(x-1)}, \tag{2.1}$$

where $x$ is the non-dimensional radial distance.

The gas pressure inside the disc is obtained as $p_{\rm gas} = R\rho T/\mu$, where $R$ is the gas constant, $\rho$ is the mass density, $T$ is the temperature and $\mu$ is the mean molecular weight assumed to be 0.5 for fully ionized hydrogen. The magnetic pressure is given by, $p_{\rm mag} =< B_\phi^2 > /8\pi$, where $< B_\phi^2 >$ is the azimuthal average of the square of the toroidal component of the magnetic field. We denote the total pressure in the disc by $P = p_{\rm gas} + p_{\rm mag}$. We define plasma $\beta$ as the ratio of gas pressure ($p_{\rm gas}$) to the magnetic pressure ($p_{\rm mag}$) inside the disc which yields $P = p_{\rm gas}(1 + 1/\beta)$. The adiabatic sound speed is defined as $a = \sqrt{\gamma P/\rho}$, where $\gamma$ is the specific heat ratio assumed to be constant throughout the flow. We adopt the canonical value of $\gamma = 1.5$ in the subsequent analysis. We consider the disc to be axisymmetric, steady and thin. Following this, we compute the half thickness of the disc ($h$) considering the flow is in hydrostatic equilibrium in the transverse direction and is given by,

$$h = \sqrt{\frac{2}{\gamma}} a x^{1/2}(x-1). \tag{2.2}$$

With this, we have the following set of governing equations describing the accretion flow around the black hole in the steady state:

(a) Radial momentum equation:

$$v\frac{dv}{dx} + \frac{1}{\rho}\frac{dP}{dx} - \frac{\lambda^2(x)}{x^3} + \frac{1}{2(x-1)^2} + \frac{\left\langle B_\phi^2 \right\rangle}{4\pi x \rho} = 0, \tag{2.3}$$

where $v$ denotes the radial velocity and $\lambda(x)$ is the specific angular momentum at radial coordinate $x$. The last term on the left hand side represents the magnetic tension force.

(b) Mass Conservation:

$$\dot{M} = 2\pi x \Sigma v, \tag{2.4}$$

where $\dot{M}$ is the mass accretion rate which is a global constant and $\Sigma$ represent the vertically integrated density of flow (Matsumoto *et al.* 1984).

(c) Azimuthal momentum equation:

$$v\frac{d\lambda(x)}{dx} + \frac{1}{\Sigma x}\frac{d}{dx}(x^2 T_{x\phi}) = 0, \tag{2.5}$$

where we consider that the vertically integrated total stress to be dominated by the $x\phi$ component of the Maxwell stress ($T_{x\phi}$). For an advective accretion flow with significant radial velocity, we estimate $T_{x\phi}$ as (Chakrabarti and Das 2004, Machida, Nakamura, and Matsumoto 2006)

$$T_{x\phi} = \frac{< B_x B_\phi >}{4\pi} h = -\alpha_B (W + \Sigma v^2), \tag{2.6}$$

where $\alpha_B$ is the proportionality constant and $W$ is the vertically integrated pressure (Matsumoto *et al.* 1984). On the basis of the seminal work of Shakura and Sunyaev (1973), we regard $\alpha_B$ as a parameter in the present study. When the flow is Keplerian, the radial velocity is very small and equation (2.6) subsequently reduces to the original prescription of '$\alpha$-model' (Shakura and Sunyaev 1973).

(d) Entropy equation:

$$\Sigma v T \frac{ds}{dx} = \frac{hv}{\gamma - 1}\left(\frac{dP}{dx} - \frac{\gamma P}{\rho}\frac{d\rho}{dx}\right) = Q^- - Q^+, \tag{2.7}$$

where we consider $\beta > 1$ inside the flow. Subsequently, we assume $\beta/(\beta+1) \sim 1$ and neglect term with $1/(\beta+1)^2$ for a modest value of $\beta$. Here, $s$ and $T$ represent the specific entropy and the local temperature of the flow, respectively. In the right hand side, $Q^+$ and $Q^-$ denote the vertically integrated heating and cooling rates. The flow is heated due to the thermalization of magnetic energy through the magnetic reconnection mechanism (Hirose, Krolik, and Stone 2006, Machida, Nakamura, and Matsumoto 2006) and therefore, expressed as

$$Q^+ = \frac{< B_x B_\phi >}{4\pi} x h \frac{d\Omega}{dx} = -\alpha_B (W + \Sigma v^2) x \frac{d\Omega}{dx}, \tag{2.8}$$

where $\Omega$ refers to the angular velocity of the flow.

In case of an accretion flow, in general, a number of radiative mechanisms, namely bremsstrahlung, synchrotron, Comptonization due to bremsstrahlung and synchrotron photons, can contribute to the cooling of the flow. However, for the sake of simplicity, in this Chapter, we assume the Comptonization of the bremsstrahlung radiation as the active cooling mechinism in the flow (see Section 1.4 for discussion). In view of this, the cooling rate of the flow is obtained as (Shapiro and Teukolsky 1983),

$$Q^{-} = \xi \times \frac{C\rho h}{v x^{3/2}(x-1)} \left[\frac{\beta}{1+\beta}\right]^{\frac{1}{2}}, \tag{2.9}$$

with

$$C = 1.974 \times 10^{-10} \left(\frac{m_e}{m_p}\right)^{\frac{1}{4}} \left[\frac{\mu m_p}{2k_B}\right]^{\frac{1}{2}} \frac{\dot{m}}{4\pi I_n m_p^2} \frac{1}{2GcM_{\odot}},$$

where $\xi$ is the cooling efficiency factor, $m_p$ and $m_e$ denote the masses of the ion and electron, respectively, $k_B$ represents the Boltzmann constant, $I_n = (2^n n!)^2/(2n+1)!$ and $n[= 1/(\gamma-1)]$ is the polytropic index. In the present analysis, any coupling between the ions and electrons has been neglected and following Chattopadhyay and Chakrabarti (2002), we estimate the electron temperature employing the relation $T_e = \sqrt{m_e/m_p}T_p$. Here, $T_p$ refer the temperature of the ion. Moreover, here $\dot{m}$ denotes the accretion rate which is measured in units of Eddington rate ($\dot{M}_{\rm Edd} = 1.39 \times 10^{17}(M_{\rm BH}/M_{\odot})$ g s$^{-1}$). Throughout this Chapter, we fix $\dot{m} = 0.05$ unless stated otherwise.

(e) Radial advection of the toroidal magnetic flux:

In order to describe the advection rate of the toroidal magnetic flux we consider the induction equation which is given by,

$$\frac{\partial < B_{\phi} > \hat{\phi}}{\partial t} = \nabla \times \left(\vec{v} \times < B_{\phi} > \hat{\phi} - \frac{4\pi}{c}\eta\vec{j}\right), \tag{2.10}$$

where $\vec{v}$ is the velocity vector, $\eta$ denotes the resistivity and $\vec{j} = c\left(\nabla \times < B_{\phi} > \hat{\phi}\right)/4\pi$ represents the current density of the flow. Equation (2.10) is azimuthally averaged. On account of very large length scale in case of accretion discs, the Reynolds number ($R_m$) is significantly large and thus we neglect the magnetic-diffusion term. Further, we also ignore the dynamo term. Assuming the steady state, the subsequent equation is then vertically averaged regarding that the azimuthally averaged toroidal magnetic fields disappear at the surface of the disc. Finally, we arrive at the toroidal magnetic flux advection rate which is given by,

$$\dot{\Phi} = -\sqrt{4\pi} v h B_0(x), \tag{2.11}$$

where

$$\begin{aligned} B_0(x) &= \langle B_\phi \rangle (x; z=0) \\ &= 2^{5/4}\pi^{1/4}(RT/\mu)^{1/2}\Sigma^{1/2}h^{-1/2}\beta^{-1/2} \end{aligned}$$

represents the azimuthally averaged toroidal magnetic field which resides at the disc equatorial plane (Oda *et al.* 2007). In the accretion discs, conservation of $\dot{\Phi}$ may not hold in general for the reason that $\dot{\Phi}$ can change radially because of the existence of the magnetic diffusion term and the dynamo term in equation (2.10). Concurrently, numerical simulation results by Machida, Nakamura, and Matsumoto (2006) showed that the relation, $\dot{\Phi} \propto x^{-1}$, holds in the disc in the quasi steady state. On the basis of this result, we introduce a parameter $\zeta$ and choose a parametric relationship between $\dot{\Phi}$ and $x$, which is given by (Oda *et al.* 2007)

$$\dot{\Phi}\left(x; \zeta, \dot{M}\right) \equiv \dot{\Phi}_{\rm edge}(\dot{M})\left(\frac{x}{x_{\rm edge}}\right)^{-\zeta}, \tag{2.12}$$

where $\dot{\Phi}_{\rm edge}$ denotes the advection rate of the toroidal magnetic flux at the outer edge of the disc ($x_{\rm edge}$). Note that the conservation of the magnetic flux is restored when $\zeta = 0$. However, for $\zeta > 0$, the magnetic flux increases as the accreting matter proceeds towards the black hole horizon. In this Chapter, we consider $\zeta$ to remain constant all throughout and adopt $\zeta = 1$ for representation, until otherwise stated.

### 2.1.2 Sonic Point Analysis

In order to study the dynamical structure of the accretion flow, one needs to obtain the global accretion solution where infalling matter from the outer edge of the disc can smoothly accrete inwards before entering in to the black hole. In addition, it is necessary for the accretion solution to become transonic in order to satisfy the inner boundary conditions imposed by the black hole event horizon. Based on the above insight, we visualize the general nature of the sonic points by solving equations (2.3), (2.4), (2.5), (2.7), (2.11) and (2.12) simultaneously (Das 2007) which is expressed as,

$$\frac{dv}{dx} = \frac{N}{D}, \tag{2.13}$$

where the numerator ($N$) is given by,

$$
\begin{aligned}
N = & \frac{C}{vx^{3/2}(x-1)}\frac{\beta^{1/2}}{(1+\beta)^{1/2}} + \frac{2\alpha_B^2 I_n(a^2g+\gamma v^2)^2}{\gamma^2 xv} \\
& + \frac{2\alpha_B^2 g I_n a^2(5x-3)(a^2g+\gamma v^2)}{\gamma^2 vx(x-1)} \\
& - \left[\frac{\lambda^2}{x^3} - \frac{1}{2(x-1)^2}\right]\left[\frac{(\gamma+1)v}{(\gamma-1)} - \frac{4\alpha_B^2 g I_n(a^2g+\gamma v^2)}{\gamma v}\right] \\
& - \frac{va^2(5x-3)}{x(\gamma-1)(x-1)} - \frac{4\lambda\alpha_B I_n(a^2g+\gamma v^2)}{\gamma x^2} \\
& - \frac{8\alpha_B^2 I_n a^2 g(a^2g+\gamma v^2)}{\gamma^2 v(1+\beta)x} + \frac{2(\gamma+1)a^2v}{\gamma(\gamma-1)(1+\beta)x}
\end{aligned}
\tag{2.13$a$}
$$

and the denominator $D$ is,

$$
\begin{aligned}
D = & \frac{2a^2}{(\gamma-1)} - \frac{(\gamma+1)v^2}{(\gamma-1)} \\
& + \frac{2\alpha_B^2 I_n(a^2g+\gamma v^2)}{\gamma}\left[(2g-1) - \frac{a^2g}{\gamma v^2}\right].
\end{aligned}
\tag{2.13$b$}
$$

Here, we write $g = I_{n+1}/I_n$.

The gradient of sound speed is calculated as,

$$
\begin{aligned}
\frac{da}{dx} = & \left(\frac{a}{v} - \frac{\gamma v}{a}\right)\frac{dv}{dx} + \frac{\gamma}{a}\left[\frac{\lambda^2}{x^3} - \frac{1}{2(x-1)^2}\right] \\
& + \frac{(5x-3)a}{2x(x-1)} - \frac{2a}{(1+\beta)x}
\end{aligned}
\tag{2.14}
$$

The gradient of angular momentum is obtained as,

$$
\begin{aligned}
\frac{d\lambda}{dx} = & -\frac{\alpha_B x(a^2g-\gamma v^2)}{\gamma v^2}\frac{dv}{dx} + \frac{2\alpha_B axg}{\gamma v}\frac{da}{dx} \\
& + \frac{\alpha_B(a^2g+\gamma v^2)}{\gamma v}
\end{aligned}
\tag{2.15}
$$

The gradient of plasma $\beta$ is given by,

$$
\begin{aligned}
\frac{d\beta}{dx} = & \frac{(1+\beta)}{v}\frac{dv}{dx} + \frac{3(1+\beta)}{a}\frac{da}{dx} + \frac{1+\beta}{x-1} \\
& + \frac{(1+\beta)(4\zeta-1)}{2x}
\end{aligned}
\tag{2.16}
$$

Matter starts accreting towards the black hole from the outer edge of the disc with almost negligible velocity and subsequently crosses the black hole horizon with velocity equal to the speed of light. This suggests that the accretion flow trajectory must be smooth along the streamline and therefore, the radial velocity gradient would be necessarily real and finite always. However, equation (2.13b) indicates that there may be some points between the outer edge of the disc and the horizon, where the denominator ($D$) vanishes. To maintain the flow to be smooth everywhere along the streamline, the point where $D$ tends to zero, $N$ must also vanish there. The point where both $N$ and $D$ vanish simultaneously is a special point and called as sonic point ($x_c$). Thus, we have $N = D = 0$ at the sonic point. Setting $D = 0$, we obtain the expression of the Mach number ($M = v/a$) at the sonic point which is calculated as,

$$M_c = \sqrt{\frac{-m_b - \sqrt{m_b^2 - 4m_a m_c}}{2m_a}}, \tag{2.17}$$

where

$$m_a = 2\alpha_B^2 I_n \gamma(\gamma - 1)(2g - 1) - \gamma(\gamma + 1)$$

$$m_b = 2\gamma + 4\alpha_B^2 I_n g(g - 1)(\gamma - 1)$$

$$m_c = -(2\alpha_B^2 I_n g^2(\gamma - 1))/\gamma$$

Setting $N = 0$, we obtain a quartic equation of the sound speed at $x_c$ and is given by,

$$\mathcal{A}_c a^4(x_c) + \mathcal{B}_c a^3(x_c) + \mathcal{C}_c a^2(x_c) + \mathcal{D}_c = 0, \tag{2.18}$$

where

$$\begin{aligned}
\mathcal{A}_c = {} & \frac{2\alpha_B^2 I_n (g + \gamma M_c^2)^2}{\gamma^2 x_c} + \frac{2\alpha_B^2 I_n g(5x_c - 3)(g + \gamma M_c^2)}{\gamma^2 x_c (x_c - 1)} \\
& - \frac{M_c^2(5x_c - 3)}{x_c(\gamma - 1)(x_c - 1)} - \frac{8\alpha_B^2 I_n g(g + \gamma M_c^2)}{\gamma^2(1 + \beta_c)x_c} \\
& + \frac{2(\gamma + 1)M_c^2}{\gamma(\gamma - 1)(1 + \beta_c)x_c},
\end{aligned}$$

$$\mathcal{B}_c = -\frac{4\lambda_c \alpha_B I_n M_c (g + \gamma M_c^2)}{\gamma x_c^2},$$

$$\mathcal{C}_c = -\left[\frac{\lambda_c^2}{x_c^3} - \frac{1}{2(x_c - 1)^2}\right]$$

$$\times \left[ \frac{(\gamma+1)M_c^2}{(\gamma-1)} - \frac{4\alpha_B^2 g I_n (g+\gamma M_c^2)}{\gamma} \right],$$

and

$$\mathcal{D}_c = \frac{C}{x_c^{3/2}(x_c-1)} \sqrt{\frac{\beta_c}{1+\beta_c}}.$$

Here, flow variables with the subscript 'c' indicate their values at the sonic point ($x_c$).

Now, for a set of input flow parameters, we solve equation (2.18) to obtain the sound speed ($a_c$) at $x_c$. Then, we obtain the radial velocity ($v_c$) at $x_c$ using equation (2.17). By employing the values of $v_c$ and $a_c$ in equation (2.13), we study the characteristics of the sonic point. At the sonic radius, $dv/dx$ assumes a 0/0 form. Thus, in order to get the physical values of $dv/dx$ at $x_c$, L'Hospital's rule is employed. At the sonic point, $dv/dx$ owns two distinct values; one of which corresponds to accretion flow and the other is for wind solutions. When both the values of $dv/dx$ are real and of opposite sign, the sonic point is of special interest as the global transonic solutions only pass through it. Such a sonic point is termed as saddle type sonic point (Chakrabarti and Das 2004). In the present Chapter, our main focus is to examine the dynamical structure of accretion flow and its various properties and therefore, the wind solutions are left aside.

## 2.2 Global Accretion Solution

In this Chapter, our goal is to obtain smooth global accretion solutions which can join the event horizon to the outer edge of the disc. With this aim, we simultaneously solve differential equations (2.13-2.16) for a specified set of flow parameters. In this process, we treat $\dot{m}$, $\xi$, $\alpha_B$, and $\gamma$ as global parameters of the flow. In addition, one needs to know the boundary values of angular momentum ($\lambda$) and plasma $\beta$ at a given radial distance ($x$) in order to solve the equations. Since the black hole solutions are necessarily transonic, flow must pass through the sonic point and therefore, it is convenient to supply the boundary values of the flow at the sonic point. With this, we integrate equations (2.13)-(2.16) from the sonic point once inwards up to the just outside the black hole horizon and then outward up to a large distance (equivalently 'disc outer edge'). Finally, these two parts of the solution are combined to obtain a complete global transonic accretion solution. Depending on the input parameters, flow may possess single or multiple sonic points (Das, Chattopadhyay, and Chakrabarti

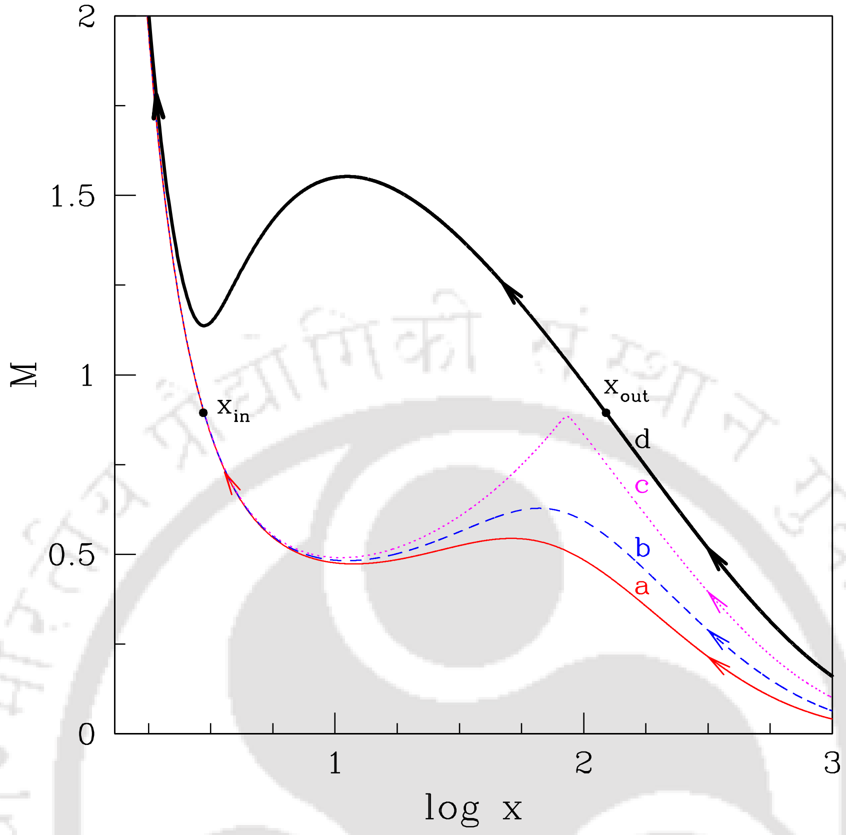

Fig. 2.1 Radial dependence of Mach number ($M = v/a$) of the accreting matter for different values of angular momentum ($\lambda_{\rm edge}$) at the outer edge $x_{\rm edge} = 1000$ where $\beta_{\rm edge} = 1400$, $\alpha_B = 0.01$ and $\xi = 10$. Thin solid and dashed curves represent the results for $\lambda_{\rm edge} = 0.2656\lambda_K$ and $0.1852\lambda_K$, respectively. For the same set of outer edge parameters, the minimum angular momentum that provides the accretion solution passing through the inner sonic is identified as $\lambda^{\rm min}_{\rm edge} = 0.1368\lambda_K$ (dotted curve). When $\lambda_{\rm edge} < \lambda^{\rm min}_{\rm edge}$, accretion solutions pass through the outer sonic point only (thick solid curve) where $\lambda_{\rm edge} = 0.1073\lambda_K$. In the figure, the locations of the inner sonic point ($x_{\rm in}$) and outer sonic point ($x_{\rm out}$) are marked and arrows indicate the direction of the flow towards the black hole. See text for details (Sarkar and Das 2016).

2001a, Sarkar and Das 2013). Sonic points which form close to the horizon are termed as inner sonic points ($x_{\rm in}$), while those form far away from the horizon are called as outer sonic points ($x_{\rm out}$). It is to be noted that we present angular momentum ($\lambda$) in terms of Keplerian angular momentum $\lambda_K$ ($\equiv \sqrt{x^3/2(x-1)^2}$) all throughout the Chapter.

### 2.2.1 Shock free global accretion solution

In Fig. 2.1, we present the examples of accretion solutions where the variation of Mach number ($M = v/a$) is plotted as function of logarithmic radial distance ($x$). The solid curve marked 'a' represents a global accretion solution passing through the inner sonic point $x_{\rm in} = 2.9740$ with angular momentum $\lambda_{\rm in} = 0.8083\lambda_K$, $\beta_{\rm in} = 27.778$, $\alpha_B = 0.01$ and $\xi = 10$, respectively and connects the BH horizon with the outer edge of the disc $x_{\rm edge}$ where we note the values of the flow variables $\lambda_{\rm edge} = 0.2656\lambda_K$, $\beta_{\rm edge} = 1400$, $v_{\rm edge} = 0.00132$, $a_{\rm edge} = 0.03205$ at $x_{\rm edge} = 1000$. Alternatively, one can obtain the same solution when the integration is carried out towards the black hole starting from the outer edge of the disc ($x_{\rm edge}$) with the noted boundary values. Hence, the above result essentially represents the solution of an accretion flow that starts its journey from $x_{\rm edge} = 1000$ and crosses the inner sonic point at $x_{\rm in} = 2.9740$ before entering into the black hole. The arrow indicates the direction of the flow. Now, we decrease $\lambda_{\rm edge} = 0.1852\lambda_K$ keeping all the other values of the flow variables same at $x_{\rm edge} = 1000$ and obtain the global transonic solution by suitably adjusting the values of $v_{\rm edge} = 0.00189$ and $a_{\rm edge} = 0.02962$. The solution is marked as 'b'. Here, the values of $v_{\rm edge}$ and $a_{\rm edge}$ is required additionally to start the integration as the sonic point is not known apriori. Following this approach, we identify the minimum value of angular momentum at the outer edge $\lambda^{\rm min}_{\rm edge} = 0.1368\lambda_K$, below this value accretion solution fails to pass through the inner sonic point. Accretion solution corresponding to the minimum $\lambda^{\rm min}_{\rm edge}$ is indicated by the dotted curve and marked as 'c'. The results namely 'a-c' represent solutions similar to the solution of advection dominated accretion flow (ADAF) around black holes (Narayan, Kato, and Honma 1997, Oda *et al.* 2007), although another important class of solutions still remains unexplored which we present in this Chapter. As $\lambda^{\rm min}_{\rm edge}$ is decreased further, such as $0.1073\lambda_K$, accretion solution changes its character and passes through the outer sonic point ($x_{\rm out} = 122.9$) instead of inner sonic point ($x_{\rm in}$) with angular momentum ($\lambda_{\rm out} = 0.1978\lambda_K$), $\beta_{\rm out} = 431.8$ which is indicated by the thick solid line marked as 'd'. In the frame work of magnetically supported accretion disc, accretion solution passing through the outer sonic points was not studied so far. Solutions particularly of this kind are potentially interesting as they may possess centrifugally supported shock waves. The presence of shock wave in an accretion flow has profound implications as it satisfactorily delineates the spectral and temporal behaviour of numerous black hole sources (Molteni, Tóth, and Kuznetsov 1999, Yadav *et al.* 1999, Okuda *et al.* 2004, Okuda, Teresi, and Molteni 2008, Nandi

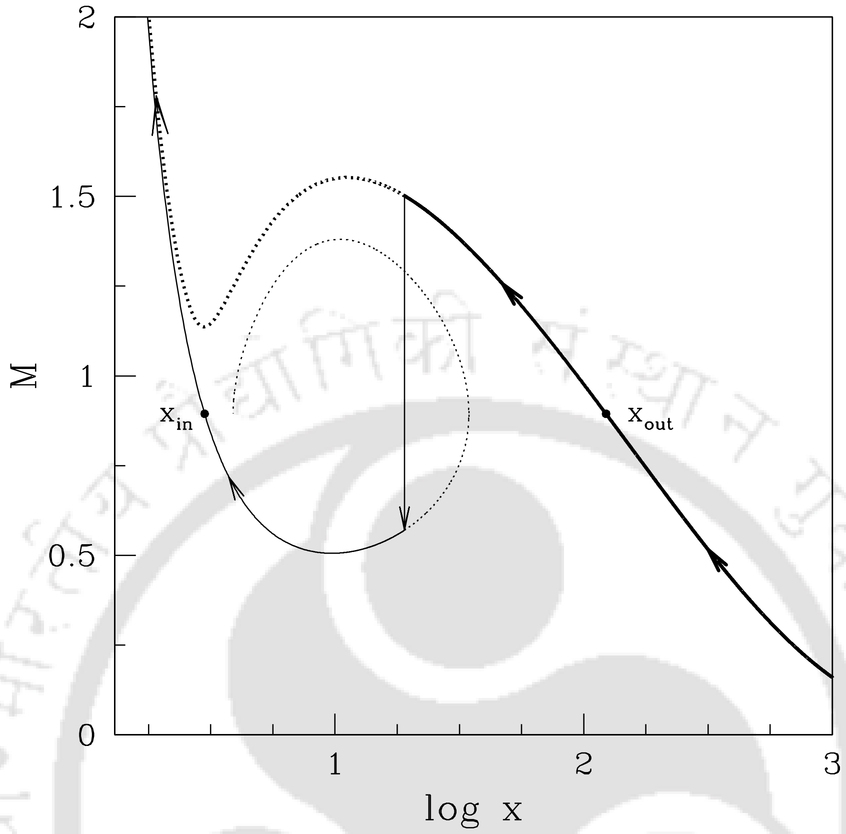

Fig. 2.2 A complete global accretion solution containing shock ($x_s = 19.03$) is depicted along with outer ($x_{\rm out}$) and inner ($x_{\rm in}$) sonic points. Inflow parameters at the outer edge are same as case (d) of Fig. 2.1. See text for details (Sarkar and Das 2016).

*et al.* 2012, Das *et al.* 2014, Okuda 2014, Aktar, Das, and Nandi 2015, Iyer, Nandi, and Mandal 2015, Okuda and Das 2015, Suková and Janiuk 2015, Aktar *et al.* 2017, Suková, Charzyński, and Janiuk 2017). Thus, in this Chapter we intend to study the properties of magnetically supported accretion solutions that possesses shock waves.

### 2.2.2 Shock induced global accretion solution

In Fig. 2.2, we present a global accretion solution that contains shock wave where the flow crosses the sonic region multiple times. Here, we consider inflowing matter that starts accreting towards the black hole sub-sonically with the boundary values at the outer edge same as the case 'd' of Fig. 2.1 and becomes supersonic after crossing the outer sonic point at $x_{\rm out} = 122.9$. As the rotating matter proceeds further, it experiences virtual barrier due to centrifugal repulsion and starts piling up there. The process continues and at some point, the flow eventually encounters discontinuous transition of flow variables in the form of shock when shock conditions are satisfied. This is because the shock solutions are thermodynamically preferred as the post-shock matter possesses high entropy content (Becker and Kazanas 2001). Following Landau & Lifshitz (1959), the conditions for shock transition in a vertically averaged flow are considered as the conservation of (a) mass flux ($\dot{M}_{-} = \dot{M}_{+}$) (b) the momentum flux ($W_{-} + \Sigma_{-} v_{-}^{2} = W_{+} + \Sigma_{+} v_{+}^{2}$) (c) the energy flux, obtained integrating equation (2.3) ($\mathcal{E}_{-} = \mathcal{E}_{+}$) and (d) the magnetic flux ($\dot{\Phi}_{-} = \dot{\Phi}_{+}$) across the shock. Here, the quantities having subscripts '$-$' and '$+$' are referred to the values before and after the shock. While doing so, we assume the shock to be thin and non-dissipative. In the post-shock region, flow momentarily slows down as it becomes subsonic immediately after the shock transition and the pre-shock kinetic energy is then converted in to the thermal energy. Therefore, the post-shock matter essentially becomes hot and dense. Due to gravitational attraction, subsonic post-shock matter continues to accrete towards the BH and gradually picks up its radial velocity and subsequently crosses the inner sonic point smoothly in order to satisfy the supersonic inner boundary condition before jumping in to the black hole. In the figure, we depict the variation of Mach number with the logarithmic radial distance. Thick curve denotes the accretion solution passing through the outer sonic point which in principle can enter in to the black hole directly. Interestingly, on the way towards the black hole, as the shock conditions are satisfied, flow makes discontinuous jump from the supersonic branch to the subsonic branch avoiding thick dotted part of the solution. In the figure, the joining of the supersonic pre-shock flow with the subsonic post-shock flow is indicated by the vertical arrow and the thin solid line denotes the inner part of the solution representing the post-shock flow. Here, $x_{\rm in}$ and $x_{\rm out}$ are the inner and outer sonic points, respectively. Arrows indicate the overall direction of the flow motion during accretion towards black hole.

In Fig. 2.3, we study the structure of a vertically averaged accretion disc corresponding to the solution depicted in Fig. 2.2. Here, each panel shows the variation of flow variables as function of logarithmic radial distance. In Fig. 2.3(a), we demonstrate the radial velocity ($v$) variation of the accreting flow where the shock transition is observed at $x_s = 19.03$ indicated by the vertical arrow. In Fig. 2.3(b), we show the density profile of the flow where the catastrophic jump of density at the shock location is observed. This happens mainly due to the reduction of radial velocity in the post-shock flow where the conservation of mass accretion is preserved across the shock. The formation of shock causes the compression of the post-shock flow that

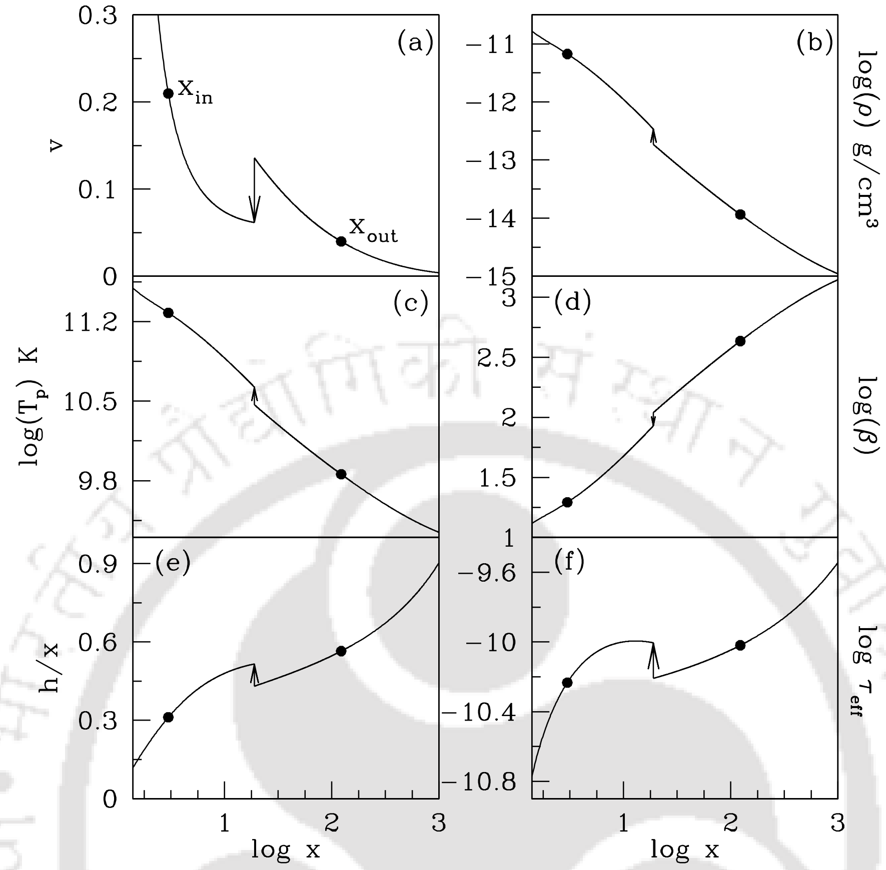

Fig. 2.3 Variation of (a) radial velocity, (b) density in g cm$^{-3}$, (c) temperature (d) ratio of gas pressure to magnetic pressure, (e) disc scaleheight $(h/x)$ and (f) effective optical depth as function of radial coordinate around a Schwarzschild black hole. All the flow variables correspond to the solution depicted in Fig. 2.2. Filled circles represent the sonic points where the closer one is the inner sonic point and the furthest one is the outer sonic point. Vertical arrows indicate the location of the shock location $x_s = 19.03$. See text for details (Sarkar and Das 2016).

along with the enhancement of density effectively increases the temperature of the flow at the inner part of the disc which we show in Fig. 2.3(c). We display the variation of plasma $\beta$ in Fig. 2.3(d) where a noticeable reduction of $\beta$ is seen at the shock location. In Fig. 2.3(e), we present the dependence of the vertical scaleheight $(h/x)$ on the radial coordinate. Here, we observe that the half thickness of the disc always remain smaller than the local radial coordinate all the way from the outer edge of the disc to the horizon even in presence of shock wave. We estimate the effective optical depth as $\tau_{\rm eff} = \sqrt{\tau_{\rm es}\tau_{\rm br}}$, where $\tau_{\rm es}$ denotes the scattering optical depth given by $\tau_{\rm es} = \kappa_{\rm es}\rho h$ and the electron scattering opacity is given by $\kappa_{\rm es} = 0.38$ cm$^2$g$^{-1}$. Here,

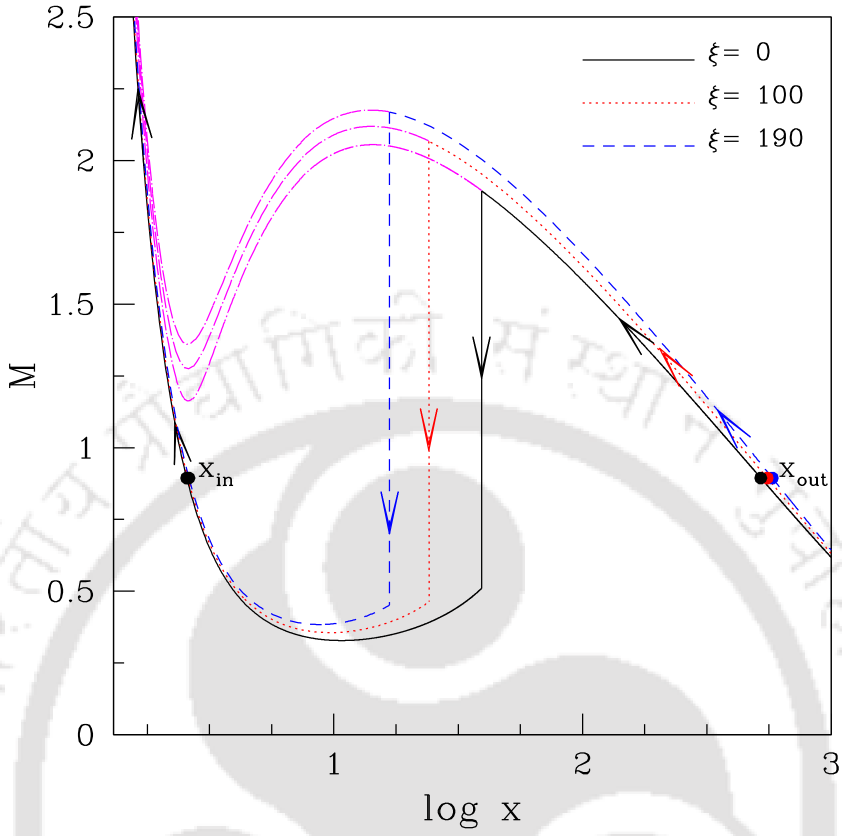

Fig. 2.4 Plot of Mach number with logarithmic radial distance for different values of cooling factor ($\xi$). Accreting flows are injected from $x_{\rm edge} = 1000$ with $\lambda_{\rm edge} = 0.084\lambda_K$, $\mathcal{E}_{\rm edge} = 1.9133 \times 10^{-4}$, $\beta_{\rm edge} = 500$, and $\alpha_B = 0.01$. Solution obtained for cooling free case ($\xi = 0$) is denoted by the solid curve whereas dotted and dashed curves represent the solution for $\xi = 100$ and 190, respectively. The corresponding shock locations are indicated by the vertical arrow as $x_s = 39.27$ (solid), 24.20 (dotted) and 16.78 (dashed). Sonic points are marked by the filled circles (Sarkar and Das 2016).

$\tau_{\rm br}$ represents the absorption effect appears due to thermal processes and is given by $\tau_{\rm br} = \left(hq_{\rm br}/4\sigma T_e^4\right)(2GM_{BH}/c^2)$ (see Section 1.5 for discussion), where $q_{\rm br}$ is the bremsstrahlung emissivity (Shapiro and Teukolsky 1983) and $\sigma$ is the Stefan-Boltzmann constant. For the purpose of representation, here we consider $M_{\rm BH} = 10^6 M_\odot$. We find that the post-shock flow remain optically thin ($\tau < 1$) although the density profile is steeper there. This intuitively suggests that the possibility of escaping hard radiations from the PSC would be quite significant.

### 2.2.3 Shock dynamics and properties

Here, we examine the effect of cooling on the dynamical structure of the accretion flow that contain shock waves. In order for that we fix the outer edge of the disc at $x_{\rm edge} = 1000$ and inject matter sub-sonically with local angular momentum $\lambda_{\rm edge} = 0.084\lambda_K$, $\beta_{\rm edge} = 500$, $\mathcal{E}_{\rm edge} = 1.9133 \times 10^{-4}$ and $\alpha_B = 0.01$, respectively. First, we consider a cooling free flow ($\xi = 0$) that becomes supersonic after crossing the outer sonic point ($x_{\rm out} = 521.22$) and continues its journey towards the black hole. Meanwhile, stationary shock conditions are satisfied and accreting matter encounters a shock transition depicted in Fig. 2.4 where Mach number ($M$) of the flow is plotted as function of logarithmic radial coordinate. The solid vertical arrow indicates the location of the standing shock at $x_s = 39.27$ for flows having no cooling. Next, we introduce cooling considering the flow parameters at the outer edge same as in the cooling free case. When cooling efficiency factor $\xi = 100$ is supplied, shock forms at $x_s = 24.20$ indicated by the dotted vertical arrow. In reality, due to shock compression, the density and temperature in the post-shock flow are enhanced compared to the pre-shock flow and therefore, cooling is very much effective there that reduces the post-shock pressure significantly. This causes the shock front to move forward towards the horizon in order to maintain the pressure balance on either sides of the shock. This clearly indicates that the dynamics of the shock in a way are controlled by the resultant pressure across it. With the gradual increase of the cooling factor $\xi$, shock front proceeds closer to the BH horizon. Following this, we identify the extreme value of cooling factor $\xi = 190$ that provides the global accretion solution including shock waves at $x_s = 16.78$ for the same outer boundary parameters as considered in cooling free case. The shock location for $\xi = 190$ is represented by the dashed vertical line in the figure. When $\xi$ is increased further, shocked accretion solution ceases to exist as the shock conditions are not satisfied there. Note that we obtain the shock induced global accretion solution even for very high cooling efficiency factor. This is possible because the effect of bremsstrahlung cooling in an accretion flow is normally weak as pointed out by Chattopadhyay and Chakrabarti (2000), Das and Chakrabarti (2004).

In our subsequent analysis, we explore the response of $\beta_{\rm edge}$ on shock dynamics. While doing this, we inject matter from the outer edge at $x_{\rm edge} = 1000$ with $\lambda_{\rm edge} = 0.0843\lambda_K$, $\mathcal{E}_{\rm edge} = 1.9133 \times 10^{-4}$, $\alpha_B = 0.01$ and $\xi = 20$, and vary $\beta_{\rm edge}$. In Fig. 2.5, solid, dotted and dashed curves represent the results corresponding to $\beta_{\rm edge} = 500, 450$ and 410, respectively. Here, the shock front moves inward as $\beta_{\rm edge}$ is decreased. This

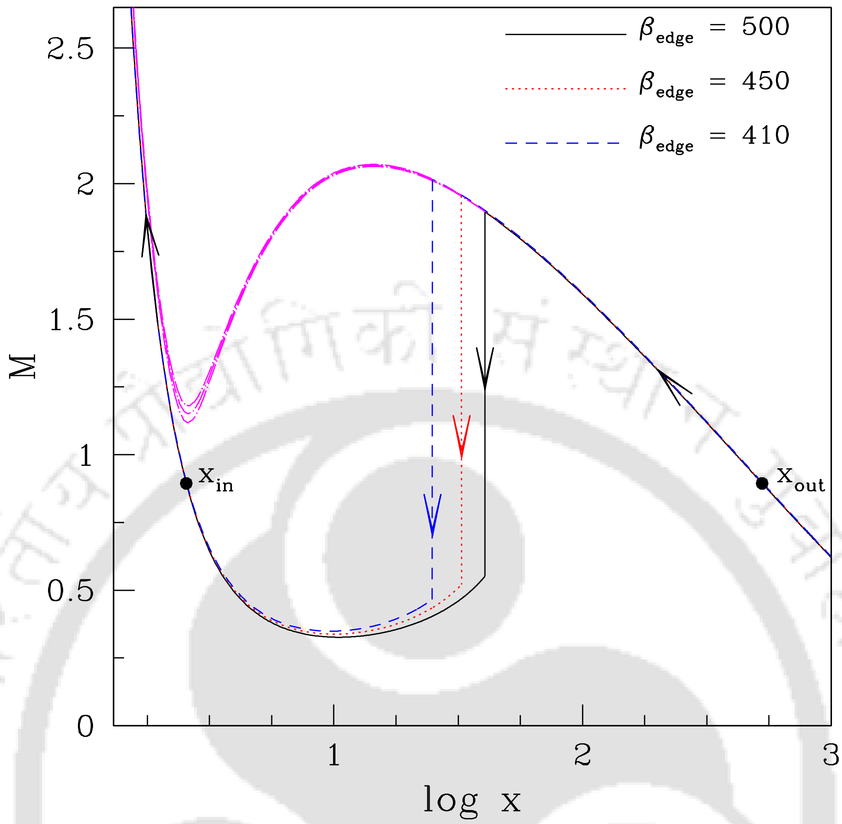

Fig. 2.5 Plot of Mach number with logarithmic radial distance for different values of $\beta_{\rm edge}$. Accreting flows are injected from $x_{\rm edge} = 1000$ with $\lambda_{\rm edge} = 0.0843\lambda_K$, $\mathcal{E}_{\rm edge} = 1.9133 \times 10^{-4}$, $\alpha_B = 0.01$ and $\xi = 20$. Solutions represented by the solid, dotted and dashed curves are for $\beta_{\rm edge} = 500$, 450 and 410 respectively. The corresponding shock locations are indicated by the vertical arrows as $x_s = 40.60$ (solid), 32.69 (dotted) and 24.94 (dashed). Sonic points are marked by the filled circles. See text for details (Sarkar and Das 2016).

eventually indicates the fact that the size of the post-shock corona decreases with the increase of the magnetic pressure inside the disc. In reality, the decrease of $\beta_{\rm edge}$ implies the increment of magnetic turbulence inside the disc. The growth of the turbulent magnetic field increases of Maxwell stress that leads to enhance the angular momentum transport outward. Hence, the centrifugal support against gravity becomes weak that pushes shock front inward. The dynamics of the shock location is eventually controlled due to the combined effect of cooling and magnetic field.

In Fig. 2.6, we present the comparison of shock properties as function of the cooling efficiency factor ($\xi$). In the upper panel (Fig. 2.6a), we show the variation of shock

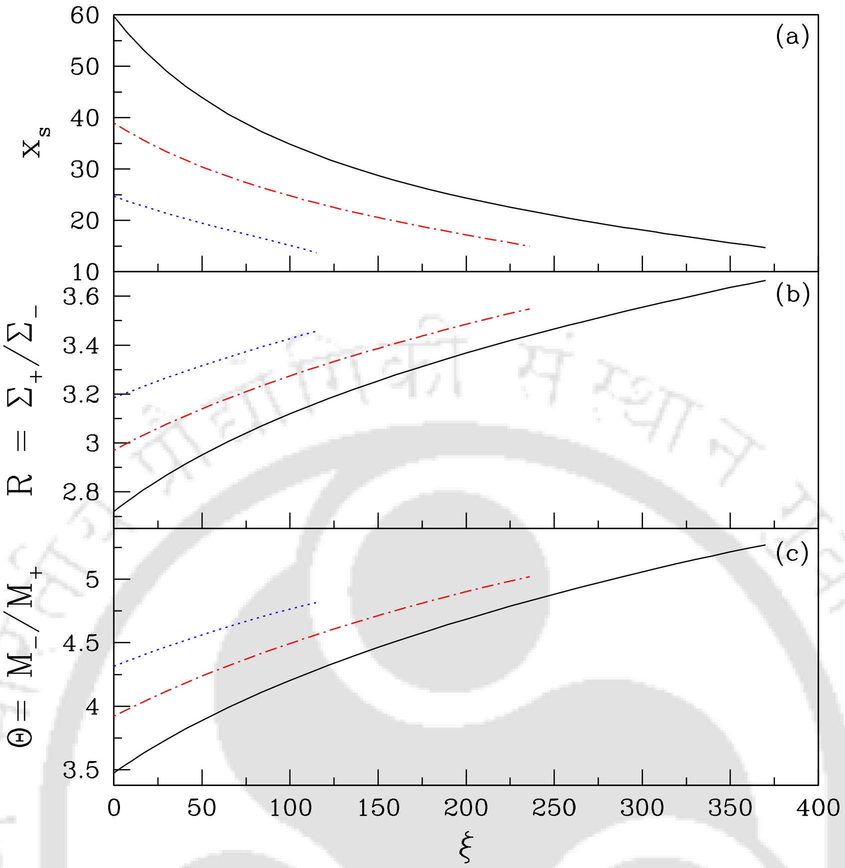

Fig. 2.6 Variation of different flow properties such as (a) the shock location $x_s$, (b) shock compression ratio $R$, and (c) shock strength $\Theta$ as a function of $\xi$ for flows injected from $x_{\rm edge} = 1000$ with $\alpha_B = 0.01$, $\beta_{\rm edge} = 550$ and $\mathcal{E}_{\rm edge} = 1.9133 \times 10^{-4}$ but with different $\lambda_{\rm edge}$. Solid curve corresponds to the result obtained for $\lambda_{\rm edge} = 0.0844\lambda_K$ and the dot-dashed and dotted curves are for $\lambda_{\rm edge} = 0.0837\lambda_K$ and $0.0829\lambda_K$, respectively. See text for details (Sarkar and Das 2016).

locations for different values of $\lambda_{\rm edge}$. Here, we choose the outer edge of the disc at $x_{\rm edge} = 1000$ and inject matter with $\mathcal{E}_{\rm edge} = 1.9133 \times 10^{-4}$, $\beta_{\rm edge} = 550$ and $\alpha_B = 0.01$ for all cases. The solid curve denotes the result corresponding to $\lambda_{\rm edge} = 0.0844\lambda_K$ and the dot-dashed and dotted curves are for $\lambda_{\rm edge} = 0.0837\lambda_K$ and $0.0829\lambda_K$, respectively. It is clear from the figure that stationary shocks in an accretion flow can be obtained for a wide range of $\xi$. For a given $\lambda_{\rm edge}$, the shock front is shifted towards the horizon with the increase of the cooling factor ($\xi$) as depicted in Fig. 2.4. This is because the flow loses its energy due to cooling during accretion. With this, when $\xi$ exceeds its critical value, shock disappears as the standing shock conditions are not satisfied. This eventually provides an indication that the possibility of stationary shock transition is likely to be reduced with the increase of $\xi$. Evidently, the critical value of $\xi$ largely depends on the accretion flow parameters at the outer edge. Moreover, above the critical cooling limit, the accretion flow still may contain shock waves which are oscillatory in nature and the investigation of such shock properties is beyond the scope of the present paper. In addition, for a given $\xi$, shock recedes away from the horizon when $\lambda_{\rm edge}$ is increased. This is not surprising as the large $\lambda_{\rm edge}$ enhances the strength of the centrifugal barrier that pushes the shock front outside. This clearly indicates that the centrifugal force seems to play a crucial role in deciding the possibility of shock formation.

As discussed in Section 2.1.1 that the bremsstrahlung emissivity directly depends on the density and temperature of the flow and therefore, the emergent radiations from the disc are also depend on them. Hence, it is useful to calculate the density and temperature distributions of the flow across the shock discontinuity as both the density and temperature are enhanced due to shock compression in the post-shock flow. For that, first we calculate the compression ratio that determines the density compression of the flow across the shock and is defined as the ratio of the vertically averaged post-shock density to the pre-shock density ($R = \Sigma_+/\Sigma_-$). In Fig. 2.6(b), we plot the variation of compression ratio as function of cooling efficiency factor for the same set of input parameters as in Fig. 2.6(a). A positive correlation is observed in all cases as the compression ratio is increased with the increase of cooling rate. This is quite natural because higher cooling efficiency pushes the shock front inward that causes more compression in the post-shock flow and eventually, compression ratio increases. When the cooling efficiency factor is reached its critical value, we observe a cut-off in the variation of compression ratio. This happens in all cases as the standing shock fails to exist there. Further, we calculate the shock strength ($\Theta$) which is defined as the ratio of pre-shock Mach number ($M_-$) to the post-shock Mach number ($M_+$) and it measures the temperature jump across the shock. In Fig. 2.6(c), we plot shock strength as function of $\xi$ for the same set of input parameters as in Fig. 2.6(a) and observe the variation of $\Theta$ very similar to $R$ as depicted in Fig. 2.6(b).

We continue our study to investigate the shock properties in terms of $\beta_{\rm edge}$ for flows with same outer boundary values, namely, $x_{\rm edge} = 1000$, $\mathcal{E}_{\rm edge} = 1.9133 \times 10^{-4}$, $\alpha_B = 0.01$ and $\xi = 20$. In Fig. 2.7, the solid, dot-dashed, dotted curves are for $\lambda_{\rm edge} = 0.0845\lambda_K$, $0.0837\lambda_K$ and $0.0829\lambda_K$, respectively. As discussed in Fig. 2.5, here also the shock location is reduced with the decrease of $\beta_{\rm edge}$ for all cases having different angular momentum at the outer edge. Interestingly, the lower limit of $\beta_{\rm edge}$ is

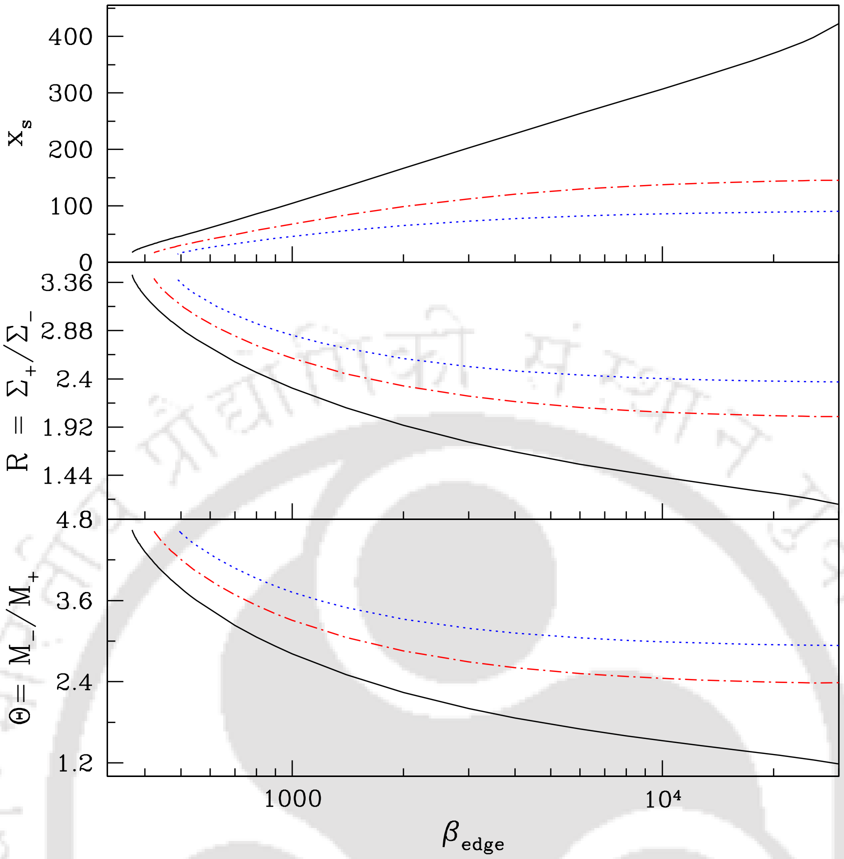

Fig. 2.7 Variation of different flow properties such as (a) the shock location $x_s$, (b) shock compression ratio $R$, and (c) shock strength $\Theta$ as a function of $\beta_{\rm edge}$ for different values of $\lambda_{\rm edge}$. Flows is injected from $x_{\rm edge} = 1000$ with $\mathcal{E}_{\rm edge} = 1.9133 \times 10^{-4}$, $\alpha_B = 0.01$ and $\xi = 20$, respectively. Results represented by the solid curve is for $\lambda_{\rm edge} = 0.0845\lambda_K$ and the dot-dashed and dotted curves are for $\lambda_{\rm edge} = 0.0837\lambda_K$ and $0.0829\lambda_K$. See text for details.

not indefinite, because the possibility of shock transition ceases to exist when $\beta_{\rm edge}$ is reduced to its critical limit. With this, we compute the shock compression ratio ($R$) and the shock strength ($\Theta$) as in Fig. 2.6(b-c) and find that both are increased when $\beta_{\rm edge}$ is decreased gradually.

### 2.2.4 Accretion disc luminosity

In this Chapter, we consider the Bremsstrahlung emission process as the prospective cooling mechanism for flows accreting on to black holes. Following this, we estimate the disc luminosity ($L_{\rm disc}$) as,

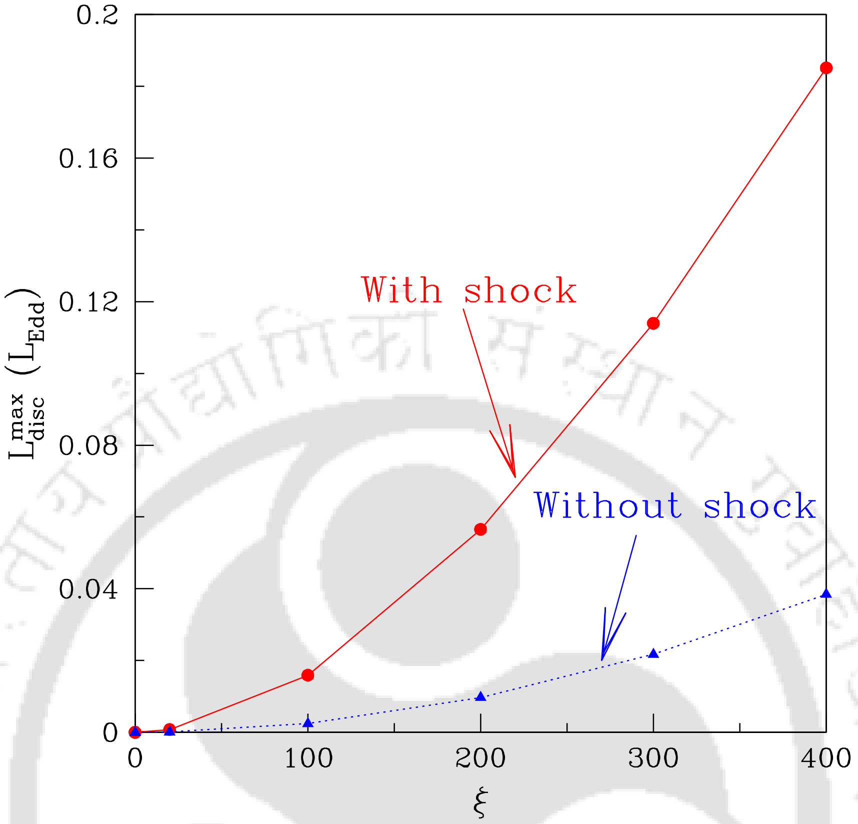

Fig. 2.8 Variation of maximum disc luminosity $L_{\rm disc}^{\rm max}$ as a function of cooling efficiency factor $\xi$. Filled circles connected with solid line and filled triangles connected with dotted line are for shocked and shock free accretion solutions (Sarkar and Das 2016).

$$L_{\rm disc} = 4\pi \int_{x_{\rm in}}^{x_{\rm edge}} Q^{-} x dx,$$

where $x_{\rm in}$ and $x_{\rm edge}$ denote the inner sonic point and the outer edge of the disc, respectively and $Q^{-}$ is the Bremsstrahlung cooling rate. Here, we neglect radiations emitted from the region between the horizon and the inner sonic point as they are expected to be red-shifted and do not contribute significantly in the disc luminosity. In Fig. 2.8, we present the variation of maximum Bremsstrahlung luminosity as function of cooling efficiency factor ($\xi$). Filled circles connected with solid lines denote the results obtained from the shock induced global accretion solution whereas the filled triangles joined with dotted lines represent the results for shock free accretion solutions. For a given cooling efficiency factor, we compute the maximum disc luminosity employing our model for shock and shock free cases. In general, we observe that the total luminosity

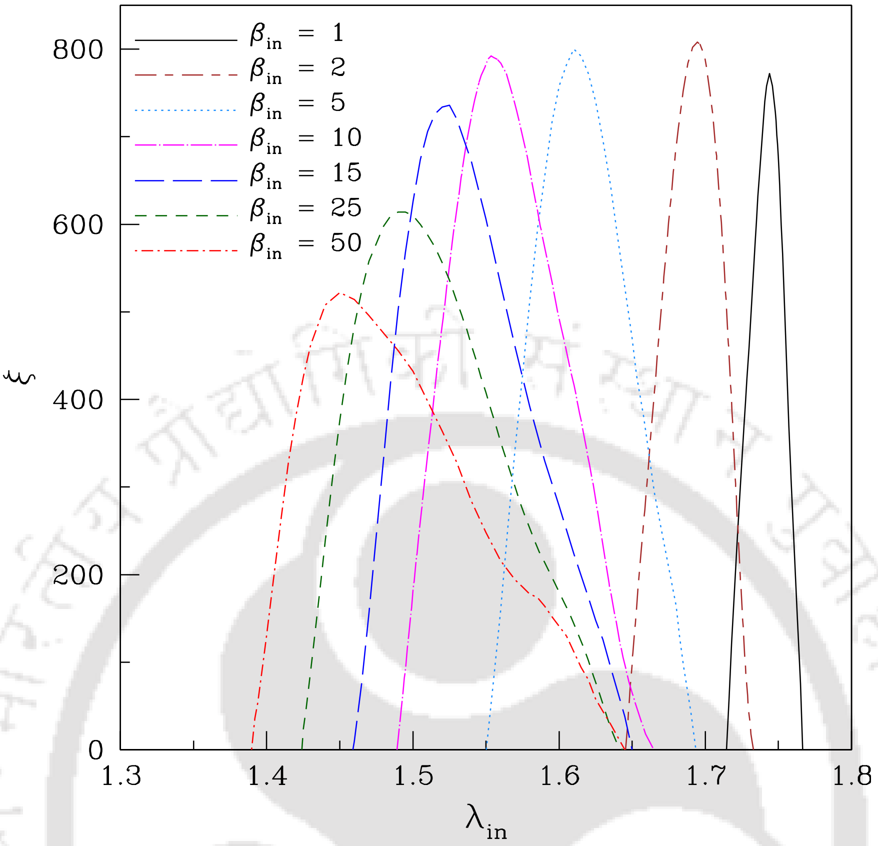

Fig. 2.9 Separations of the parameter space that allow stationary shock waves in the $\lambda_{\rm in} - \xi$ plane. Dot-dashed, dashed, long-dashed, dot-long dashed, dotted, short-long dashed and solid curves are for $\beta_{\rm in} = 50, 25, 15, 10, 5, 2,$ and 1, respectively. Here, we fix $\alpha_B = 0.01$. See text for details (Sarkar and Das 2016).

is enhanced when $\xi$ is increased. This is because the rise of $\xi$ essentially increase the density of the flow and consequently flow cools efficiently. In addition, we find that for a given $\xi$, the disc luminosity is always higher for flows containing shock waves compared to the flows having no shocks. This apparently provides an indication that the shocked accretion solutions are perhaps potentially more preferred to study the energetics of the black hole sources.

### 2.2.5 Parameter space for shock

It is already pointed out that the dissipative global accretion solutions including shock waves are not the isolated solutions, instead such solutions exist for a wide range of angular momentum and the cooling efficiency factor. In order to understand

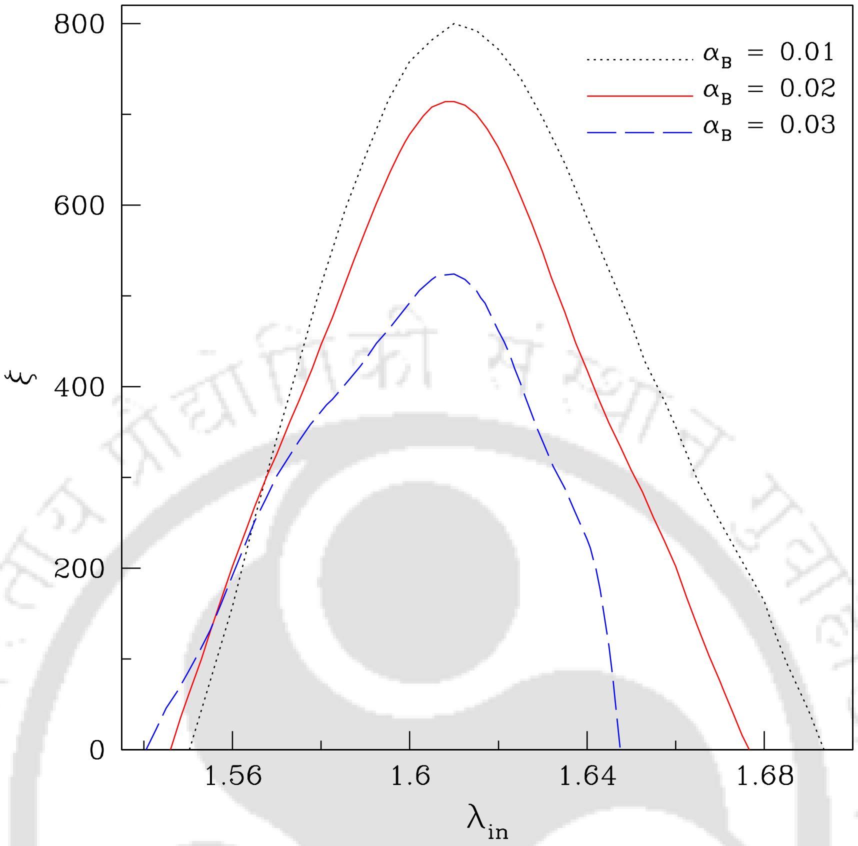

Fig. 2.10 Effective regions of the parameter space for stationary shock in the $\lambda_{\rm in} - \xi$ plane. The regions separated by dotted, solid and dashed curves are for $\alpha_B = 0.01, 0.02$, and 0.03, respectively. Here, we fix $\beta_{\rm in} = 5$. See text for details (Sarkar and Das 2016).

the influence of magnetic field on the properties of the stationary shock waves in a dissipative accretion flow, we identify the region of the parameter space spanned by the angular momentum at the inner sonic point ($\lambda_{\rm in}$) and the cooling efficiency factor ($\xi$) that provides shock solutions and subsequently classify them in terms of $\beta_{\rm in}$. Here, $\beta_{\rm in}$ refers to the value of $\beta$ measured at the inner sonic point $x_{\rm in}$. The results are depicted in Fig. 2.9 where, we choose $\alpha_B = 0.01$. The dot-dashed boundary separates the shock parameter space and is obtained for $\beta_{\rm in} = 50$ where magnetic pressure is weak and accretion flow is tended to be gas pressure dominated. As the strength of the magnetic pressure is increased relative to the gas pressure, the parameter space shifts towards the higher angular momentum side. This is due to the fact that the range of angular momentum at the inner sonic point for transonic accretion flow increases when $\beta_{\rm in}$ is decreased. Here, dashed, long-dashed, dot-long dashed, dotted, short-long dashed and solid curves identify the boundary for $\beta_{\rm in} = 25$, 15, 10, 5, 2 and 1, respectively.

We observe that when the accretion flow starts dominated by the magnetic pressure, the effective region of the parameter space for standing shocks reduces gradually and finally disappears when $\beta_{\rm in}$ reached its critical value.

We continue our study of parameter space to explore the role of viscous dissipation in the shock parameter space. While doing so, we choose $\beta_{\rm in} = 5$ all throughout and obtain the parameter space as function of $\alpha_B$ which is depicted in Fig. 2.10. As before, here again we find that shock induced global accretion solutions are obtained for a wide range of input parameters, namely $\lambda_{\rm in}$ and $\xi$. In the figure, the viscous dissipation parameters are marked. We observe that as the dissipation is increased, the parameter space for stationary shock is shrunk. This is simply because the possibility of shock transition is reduced with the enhancement of dissipation in the flow. Eventually, the shock parameter space disappears when $\alpha_B$ is crossed its critical value.

### 2.2.6 Critical viscosity parameter

In the previous Section, we have pointed out that the dynamical structure of the global accretion flow changes when the viscosity parameter exceeds its critical value. Following this, we obtain the value of the critical viscosity parameter $\alpha_B^{\rm cri}$ based on the criteria of whether a standing shock is formed or not. Evidently, the critical viscosity parameter largely depends on the inflow parameters. In Fig. 2.11, we demonstrate the variation of $\alpha_B^{\rm cri}$ with $\beta_{\rm in}$ for $\xi = 20$. In a magnetized flow, the angular momentum transport in the disc equatorial plane is increased as the magnetic pressure contributes to the total pressure. Hence, a lower value of $\alpha_B$ is sufficient to transport angular momentum required for shock formation. On the contrary, the possibility of shock formation is enhanced with the higher viscosity parameter when the flow is shifted towards the gas pressure dominated regime. As $\beta_{\rm in}$ is increased, the critical viscosity parameter $\alpha_B^{\rm cri}$ tends to approach $\alpha_{\Pi}^{\rm cri}$ ($\sim 0.3$) as estimated by the Chakrabarti and Das (2004) for gas pressure dominated flow.

## 2.3 Astrophysical Applications

So far, we have concentrated on the accretion shocks around black holes where the specific energy across the shock front is considered to be constant (Chakrabarti 1989) and these shocks are radiatively inefficient in nature. However, in reality, the characteristic of the shocks can be dissipative as well where a part of the accreting energy is

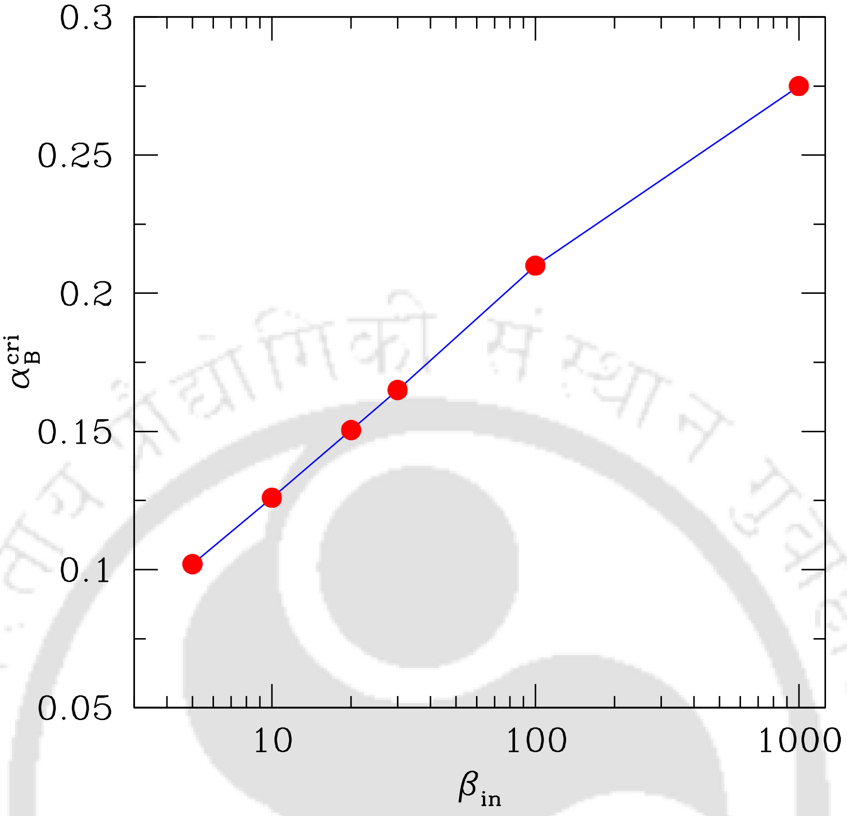

Fig. 2.11 Variation of critical viscosity parameter ($\alpha_B^{\rm cri}$) with $\beta_{\rm in}$ that allows standing shocks. Here, we consider $\xi = 20$. See text for details (Sarkar and Das 2016).

released vertically through the disc surface at the shock location causing the reduction of specific energy in the PSC (Singh and Chakrabarti 2011). Usually the energy dissipation mechanism at the shock is regulated by the thermal Comptonization process (Chakrabarti and Titarchuk 1995) and therefore, the thermal distribution in the PSC is reduced. Based on this criteria, we estimate the energy loss across the shock where we assume that the loss of energy is scaled with the temperature difference between the immediate post-shock and pre-shock flow and is given by (Das, Chakrabarti, and Mondal 2010),

$$\Delta\mathcal{E} = \Delta\mathcal{E}'(a_+^2 - a_-^2), \tag{2.19}$$

where $a_+$ and $a_-$ are the post-shock and pre-shock sound speeds, respectively and $\Delta\mathcal{E}'$ denotes the fraction of the thermal energy difference lost in this process which we treat as a parameter. For a weakly rotating black hole, Das, Chakrabarti, and Mondal (2010) calculated the maximum energy dissipation at the shock and is estimated as

$\Delta\mathcal{E}^{\rm max} \sim 2.5$ per cent. Needless to mentioned that $\Delta\mathcal{E}$ chosen beyond this range does not provide global transonic accretion solution including shock waves.

In this scenario, the accessible energy at the PSC is same as the available energy dissipated at the shock. A fraction of this energy is converted in to high energy radiations and the remaining part of the energy is utilized to produce jets as they are likely to originate from the PSC around the black holes. Subsequently, these jets simultaneously ingest a part of this energy for the work done against gravity and for carrying out their thermodynamical expansion. The remaining part of the energy is then utilized to power the jets. Therefore, according to the energy budget, the total usable energy available in the post-shock flow is $\Delta\mathcal{E}$ and the corresponding loss of kinetic power from the disc can be estimated in terms of the observable quantities as in Le and Becker (2004; 2005),

$$L_{\rm total} = L_{\rm shock} = \dot{M} \times \Delta\mathcal{E} \times c^2 \ \ {\rm erg\ s^{-1}}, \tag{2.20}$$

where $L_{\rm total}$ is the kinetic power lost by the disc, $L_{\rm shock}$ is the shock luminosity and $\dot{M}$ is the accretion rate for a given source, respectively. Following the above approach, we estimate the maximum shock luminosity ($L^{\rm max}_{\rm shock}$) that corresponds to maximum energy dissipation at the shock. Here, $\alpha_B = 0.001$ and $\xi = 10$ are considered for all cases. In Table 2.1, we present the physical parameters of the super-massive black hole sources including model parameters and estimated maximum shock luminosity. In column 1-3, we display the list of sources, their mass ($M_{\rm BH}$) and dimensionless accretion rate ($\dot{m}$). In column 4-6, we indicate the representative values of flow variables at the outer sonic point, namely energy $\mathcal{E}_{\rm out}$, angular momentum $\lambda_{\rm out}$ and $\beta_{\rm out}$. In column 7, we mention the $\Delta\mathcal{E}'$ value that provides the maximum $\Delta\mathcal{E}^{\rm max}$ (in column 8) and shock location $x_s$ (in column 9). In column 10, we present the maximum shock luminosity $L^{\rm max}_{\rm shock}$. In this analysis, our motivation is to quantify the upper limit of the energy that can be extracted from the PSC to power the deflected matter from the disc as Jets. Therefore, we calculate the maximum energy dissipation $\Delta\mathcal{E}^{\rm max}$ at the location of shock transition. We find that the estimated shock luminosities for super-massive black hole sources under consideration are in close agreement with the observed core radio luminosity values $L^{\rm Obs}_{\rm jet}$ (in column 11) (Falcke and Biermann 1999, Falcke, Körding, and Markoff 2004, de Gasperin *et al.* 2012, Riffel, Storchi-Bergmann, and Winge 2013, Shafi *et al.* 2015).

Table 2.1 Estimation of shock luminosity. Column 1 lists the names of the sources and Column 2-3 give mass and accretion rate. Column 4-7 provide the model parameters and Column 8-10 denote the maximum energy dissipation, shock location and estimated maximum shock luminosity obtained from equation (2.20). Observed core radio luminosity values are given in column 11 (Sarkar and Das 2016).

| Object | $M_{\rm BH}$ ($\rm M_{\odot}$) | $\dot{m}$ ($\dot{M}_{\rm Edd}$) | $\mathcal{E}_{\rm out}$ ($10^{-4}c^2$) | $\lambda_{\rm out}/\lambda_K$ | $\beta_{\rm out}$ | $\Delta\mathcal{E}'$ | $\Delta\mathcal{E}^{\rm max}$ ($10^{-3}c^2$) | $x_s$ ($r_g$) | $L^{\rm max}_{\rm shock}$ (erg $\rm s^{-1}$) | $L^{\rm Obs}_{\rm jet}$ (erg $\rm s^{-1}$) |
|---|---|---|---|---|---|---|---|---|---|---|
| Sgr A* | $4.90 \times 10^{6\ a}$ | $2.776 \times 10^{-4\ b}$ | 2.356 | 0.1131 | 1000 | 0.65 | 3.637 | 13.66 | $6.2 \times 10^{38}$ | $1.0 \times 10^{39\ c}$ |
| NGC 4258 | $3.39 \times 10^{7\ d}$ | $9.423 \times 10^{-5\ e}$ | 1.996 | 0.1044 | 3500 | 0.71 | 3.937 | 14.48 | $1.6 \times 10^{39}$ | $1.0 \times 10^{42\ c}$ |
| NGC 3079 | $6.76 \times 10^{7\ d}$ | $5.907 \times 10^{-3\ e}$ | 2.129 | 0.1072 | 2400 | 0.64 | 3.835 | 13.42 | $1.9 \times 10^{41}$ | $4.0 \times 10^{41\ f}$ |
| Mrk 79 | $5.24 \times 10^{7\ g}$ | $1.125 \times 10^{-2\ h}$ | 2.219 | 0.11 | 2000 | 0.74 | 4.242 | 13.39 | $3.1 \times 10^{41}$ | $3.4 \times 10^{40\ h}$ |
| NGC 6500 | $1.70 \times 10^{8\ d}$ | $8.000 \times 10^{-6\ i}$ | 2.125 | 0.1074 | 3000 | 0.70 | 4.089 | 13.51 | $6.9 \times 10^{38}$ | $7.9 \times 10^{38\ j}$ |
| M87 | $3.50 \times 10^{9\ k}$ | $1.192 \times 10^{-4\ l}$ | 2.468 | 0.1149 | 330 | 0.34 | 1.938 | 13.72 | $1.0 \times 10^{41}$ | $5.0 \times 10^{44\ m}$ |

References: [a]Aschenbach (2010), [b]Yuan, Markoff, and Falcke (2002a), [c]Falcke and Biermann (1999), [d]Kadowaki, de Gouveia Dal Pino, and Singh (2015), [e]Yamauchi *et al.* (2004), [f]Shafi *et al.* (2015), [g]Peterson *et al.* (2004), [h]Riffel, Storchi-Bergmann, and Winge (2013), [i]Satyapal, Sambruna, and Dudik (2004), [j]Falcke, Körding, and Markoff (2004), [k]Walsh *et al.* (2013), [l]Kuo *et al.* (2014), [m]de Gasperin *et al.* (2012).

## 2.4 Chapter Conclusion

In this Chapter, we have studied the dynamical structure of a magnetized accretion flow around a non-rotating black hole in presence of Bremsstrahlung cooling. Since the exact physical mechanism for angular momentum transport in an accretion disc is not yet conclusive, we assume that the Maxwell stress is proportional to the total pressure following the work of Machida, Nakamura, and Matsumoto (2006), where the constant of proportionality $\alpha_B$ plays the role similar to the conventional viscosity parameter as described in Shakura and Sunyaev (1973). We indeed find that such an accretion flow is transonic in nature. This is because the inflowing matter must satisfy the inner boundary condition imposed by the black hole horizon. Depending on the flow parameters, namely angular momentum ($\lambda$), viscosity ($\alpha_B$), cooling efficiency factor ($\xi$) and $\beta$ respectively, accreting matter changes its sonic state multiple times as it contains multiple sonic points. Flows of this kind are of special interest as they may contain shock wave which is perhaps essential to understand the spectral and timing properties of the black hole candidates (Chakrabarti and Manickam 2000, Nandi *et al.* 2001a;b; 2012, Radhika and Nandi 2014, Iyer, Nandi, and Mandal 2015, Radhika *et al.* 2016, Bhattacharjee *et al.* 2017).

In Section 2.2, we calculate the shock induced global accretion solution in presence of toroidal magnetic field. Due to shock transition, the post-shock flow, (*i.e.*, PSC) is compressed and as a consequence, PSC becomes hot and dense as is seen in Fig. 2.3. According to our solutions, PSC remains optically thin though there is a sharp rise of density at the inner part of the disc. This effectively enhances the possibility of escaping the hard radiations from PSC. When the cooling efficiency is increased, the thermal pressure of PSC is evidently reduced. As a consequence, shock front moves towards the horizon and finally settles down at a smaller radius where total pressure across the shock front is balanced. Above the critical cooling limit ($\xi^{\rm cri}$), PSC disappears due to effect of excess cooling where shock conditions are not favorable. It must be noted that $\xi^{\rm cri}$ does not correspond to a unique value as it depends of the other flow parameters.

One of the important results of this work is to obtain the global shock solutions in gas pressure dominated flow as well as magnetic pressure dominated flow and subsequently investigate the dependencies of flow parameters on shock properties. In Figs 2.6 and 2.7, we observe that global shock solutions are not the isolated solutions, instead shock may form for a wide range of flow parameters. Moreover, we find that

$\alpha_B$ and $\beta$ play important role in deciding the formation of shock waves (Figs 2.9 and 2.10).

We also calculate the critical viscosity parameter ($\alpha_B^{\rm cri}$) that allows standing shocks in the accretion flow around black holes. Beyond this critical limit, standing shock conditions are not favorable and hence, steady shock ceases to exist. We find that $\alpha_B^{\rm cri}$ gradually increases as the plasma $\beta$ increases and ultimately tends to the value $\sim 0.3$ as reported by Chakrabarti and Das (2004) for gas pressure dominated flow (Fig. 2.11).

Further, we self-consistently study the characteristics of the dissipative shock solutions. In this scenario, a part of the accreting energy is escaped from the shock location in the vertical directions through the disc surface and this dissipated energy is being utilized to power the jets (Chakrabarti and Titarchuk 1995, Le and Becker 2004; 2005). In order to understand the implications of the dissipative shock, we estimate the maximum shock luminosity ($L_{\rm shock}^{\rm max}$) corresponding to the maximum energy dissipation ($\Delta\mathcal{E}^{\rm max}$) at the shock using equations (2.19) and (2.20). In Table 2.1, we summarize the physical parameters of the black hole sources along with the model parameters and $L_{\rm shock}^{\rm max}$. We observe that the estimated $L_{\rm shock}^{\rm max}$ for several super-massive black hole sources are in close agreement with the observed core radio luminosity values ($L_{\rm jet}^{\rm Obj}$).

# Chapter 3

# Magnetically supported accretion flows in presence of synchrotron cooling

The bremsstrahlung cooling mechanism employed in the previous Chapter is the dominant cooling process in the accretion disc around a supermassive black hole where the magnetic field is expected to be low because of large size of the accretion disc.[1] In the present Chapter, we concentrate on the role of synchrotron cooling on magnetically supported accretion flows around black holes. Accretion discs around stellar mass black holes, being relatively smaller in size as compared to supermassive black holes, are expected to be threaded by significant amount of magnetic fields as a consequence of equipartition theory. In such a case, synchrotron emission is expected to be the dominant cooling process in mangetized accretion disc around a stellar mass black hole. When there is significant cooling of the disc, the disc can undergo transition from gas pressure dominated state to magnetic pressure dominated state because of flux conservation at a particular radii (Oda *et al.* 2007; 2012). In the present Chapter, motivated by these reasons, we make a detailed exploration of the effect of toroidal magnetic fields in magnetically supported accretion discs around black holes assuming synchrotron radiation to be the active cooling mechanism. Thus, to model the dissipative accretion flow, a set of steady state magneto-hydrodynamical equations are considered. The magnetic energy dissipation process governs the heating of the flow. The geometry of space time around the black hole is described by the Paczyński and

---

[1] The contents of this chapter are published in Sarkar B., Das S., Mandal S., 2018, MNRAS, 473, 2415.

Wiita (1980) pseudo-Newtonian potential. With this, we self-consistently calculate the global accretion solution including shock waves and investigate the shock properties in terms of the flow parameters. We establish that a wide range of flow parameters admits shocks in an accretion flow. We identify the critical limits of viscosity parameter which allows the existence of shocks in the entire regime ranging from magnetic pressure dominated to gas pressure dominated disc. We also quantify the critical limits of accretion rate which allows the existence of shocks in accretion flow and study its variation with plasma $\beta$. Furthermore, we present the overall variation of the typical spectra for shocked accretion flows injected with a fixed outer edge conditions having different plasma $\beta$ values. Finally, considering the dissipative nature of shocks, we present the theoretical estimate of the maximum energy dissipation ($\Delta\mathcal{E}^{\rm max}$) at shock. Using this available energy at shock, we calculate the maximum kinetic power lost from the disc ($L^{\rm max}_{\rm shock}$), which would be useful to understand the core radio luminosities associated with black hole sources.

The outline of the Chapter is as follows. In Section 3.1, we present the assumptions and governing equations for our model. In Section 3.2, we investigate the global accretion solutions with and without shock, shock properties, and the critical limits of viscosity and accretion rate. Next, we present the radiation spectra of the shocked accretion flows from our model. We also apply our formalism to calculate the maximum energy dissipation at shock and the corresponding shock luminosities. Finally in Section 3.3, we present the concluding remarks.

## 3.1 Governing Equations

The magnetic field structure in the accretion disc is considered to be same as has already been described in the beginning of Section 2.1 of the previous Chapter. As in the previous Chapter, we adopt the Geometric unit system $2G = M_{\rm BH} = c = 1$, in this Chapter as well, where $G$ is the universal Gravitational constant, $M_{\rm BH}$ is the mass of the black hole and $c$ is the speed of light. The notations used for the flow variables are also the same as in the previous Chapter. Further the governing equations (2.1-2.6, 2.8, 2.10-2.12) are also applicable in this Chapter and we avoid repeating them here. However, we wish to highlight the modifications in the entropy generation equation and the cooling mechanism adopted in the present Chapter as compared to those in Chapter 2. In this Chapter, the entropy generation equation (2.7) is modified as,

$$\Sigma \upsilon T \frac{ds}{dx} = \frac{h\upsilon}{\gamma - 1}\left(\frac{dp_{\rm gas}}{dx} - \frac{\gamma p_{\rm gas}}{\rho}\frac{d\rho}{dx}\right) = Q^{-} - Q^{+}, \tag{3.1}$$

In an accretion disc, the cooling of the flow is governed by the various radiative processes, such as, bremsstrahlung, synchrotron or Comptonization of bremsstrahlung and synchrotron photons. Since the accretion flow is magnetized in nature, synchrotron process becomes effective to cool the flow and the cooling rate due to the synchrotron radiation is given by (Shapiro and Teukolsky 1983),

$$Q^{-} = \frac{Sa^5 \rho h}{\upsilon x^{3/2}(x-1)} \frac{\beta^2}{(1+\beta)^3}, \tag{3.2}$$

with,

$$S = 1.048 \times 10^{18} \frac{\dot{m}\mu^2 e^4}{I_n m_e^3 \gamma^{5/2}} \frac{1}{2GM_\odot c^3},$$

where $e$ and $m_e$ denote the charge and mass of the electron, respectively. And, $k_B$ is the Boltzmann constant, $\mu$ $(= 0.5)$ is the mean molecular weight, $I_n = (2^n n!)^2/(2n+1)!$ and $n = 1/(\gamma - 1)$. Following Chattopadhyay and Chakrabarti (2002), we estimate the electron temperature as $T_e = \sqrt{m_e/m_p} T_p$ where, the coupling between the ions and electrons, if any, is ignored. $m_p$ and $T_p$ refer respectively to the mass and temperature of the ion. In the subsequent sections, we express accretion rate in units of Eddington rate ($\dot{M}_{\rm edd} = 1.39 \times 10^{17} \times M_{\rm BH}/M_\odot$ g s$^{-1}$) and we denote it by $\dot{m}$. Furthermore, in account of the energy loss of the flow, we neglect the contribution of the bremsstrahlung emission because it is regarded as a very inefficient cooling process for stellar mass black hole systems (Chattopadhyay and Chakrabarti 2000, Das 2007). We use the canonical value of $\gamma = 4/3$ in the subsequent study, unless otherwise stated.

### 3.1.1 Sonic Point Analysis

In the process of accretion on to the black hole, infalling matter starts its journey from the outer edge of the disc with negligible radial velocity and subsequently crosses the black hole horizon with the velocity comparable to the speed of light. This findings evidently demand that during accretion, infalling matter must change its sonic character smoothly from subsonic state to supersonic state before falling in to the black hole. The radial coordinate where accreting matter encounter such sonic transition is known as sonic point. In the next paragraphs, we carry out the sonic point analysis of the accretion flow by simultaneously solving equations (2.3), (2.4), (2.5), (3.1), (2.11) and (2.12) which is expressed as,

$$\frac{d\upsilon}{dx} = \frac{N}{D}, \tag{3.3}$$

where the numerator $N$ is given by,

$$\begin{aligned} N = {} & \frac{Sa^5}{\upsilon x^{3/2}(x-1)}\frac{\beta^2}{(1+\beta)^3} + \frac{2\alpha_B^2 I_n(a^2g+\gamma\upsilon^2)^2}{\gamma^2 x\upsilon} \\ & + \frac{2\alpha_B^2 g I_n a^2(5x-3)(a^2g+\gamma\upsilon^2)}{\gamma^2\upsilon x(x-1)} \\ & - \left[\frac{\lambda^2}{x^3} - \frac{1}{2(x-1)^2}\right]\left[\frac{[3+\beta(\gamma+1)]\upsilon}{(\gamma-1)(1+\beta)} - \frac{4\alpha_B^2 g I_n(a^2g+\gamma\upsilon^2)}{\gamma\upsilon}\right] \\ & - \frac{\upsilon a^2(5x-3)}{x(\gamma-1)(x-1)}\frac{(\beta+\frac{3}{2\gamma})}{(1+\beta)} - \frac{4\lambda\alpha_B I_n(a^2g+\gamma\upsilon^2)}{\gamma x^2} \\ & - \frac{8\alpha_B^2 I_n a^2 g(a^2g+\gamma\upsilon^2)}{\gamma^2\upsilon(1+\beta)x} + \frac{2[3+\beta(\gamma+1)]a^2\upsilon}{\gamma(\gamma-1)(1+\beta)^2 x} \\ & - \frac{a^2\upsilon}{\gamma(\gamma-1)(1+\beta)(x-1)} - \frac{a^2\upsilon(4\zeta-1)}{2\gamma x(\gamma-1)(1+\beta)} \end{aligned} \tag{3.3a}$$

and the denominator $D$ is given by,

$$\begin{aligned} D = {} & \frac{2a^2}{(\gamma-1)}\left[\frac{2}{\gamma(1+\beta)} + \frac{\beta}{1+\beta}\right] - \frac{[3+(\gamma+1)\beta]\upsilon^2}{(\gamma-1)(1+\beta)} \\ & + \frac{2\alpha_B^2 I_n(a^2g+\gamma\upsilon^2)}{\gamma}\left[(2g-1) - \frac{a^2g}{\gamma\upsilon^2}\right]. \end{aligned} \tag{3.3b}$$

Here, we write $g = I_{n+1}/I_n$.

Further, we obtain the gradient of sound speed, angular momentum and plasma $\beta$, respectively as

$$\begin{aligned} \frac{da}{dx} = {} & \left(\frac{a}{\upsilon} - \frac{\gamma\upsilon}{a}\right)\frac{d\upsilon}{dx} + \frac{\gamma}{a}\left[\frac{\lambda^2}{x^3} - \frac{1}{2(x-1)^2}\right] \\ & + \frac{(5x-3)a}{2x(x-1)} - \frac{2a}{(1+\beta)x}, \end{aligned} \tag{3.4}$$

$$\frac{d\lambda}{dx} = -\frac{\alpha_B x(a^2g-\gamma\upsilon^2)}{\gamma\upsilon^2}\frac{d\upsilon}{dx} + \frac{2\alpha_B a x g}{\gamma\upsilon}\frac{da}{dx}$$

$$+\frac{\alpha_B(a^2 g+\gamma v^2)}{\gamma v}, \tag{3.5}$$

$$\begin{aligned}\frac{d\beta}{dx} &= \frac{(1+\beta)}{v}\frac{dv}{dx}+\frac{3(1+\beta)}{a}\frac{da}{dx}+\frac{1+\beta}{x-1}\\ &+\frac{(1+\beta)(4\zeta-1)}{2x}.\end{aligned} \tag{3.6}$$

From equation (3.3), we obtain two conditions at the sonic point as $N=0$ and $D=0$. Setting $D$ to zero, we have the expression of Mach number ($M=v/a$) at the sonic point ($x_c$) as,

$$M(x_c)=\sqrt{\frac{-m_2-\sqrt{m_2^2-4m_1m_3}}{2m_1}}, \tag{3.7}$$

where

$$m_1 = 2\alpha_B^2 I_n\gamma^2(1+\beta_c)(\gamma-1)(2g-1)-\gamma^2(3+(\gamma+1)\beta_c),$$

$$m_2 = 2\gamma(2+\gamma\beta_c)+4\alpha_B^2 I_n\gamma g(1+\beta_c)(g-1)(\gamma-1),$$

$$m_3 = -2\alpha_B^2 I_n g^2(1+\beta_c)(\gamma-1).$$

Using $N=0$, we get an algebraic equation of the sound speed at $x_c$ which is given by,

$$\mathcal{A}a^3(x_c)+\mathcal{B}a^2(x_c)+\mathcal{C}a(x_c)+\mathcal{D}=0, \tag{3.8}$$

where

$$\mathcal{A}=\frac{S}{x_c^{3/2}(x_c-1)}\frac{\beta_c^2}{(1+\beta_c)^3},$$

$$\begin{aligned}\mathcal{B}=&\frac{2\alpha_B^2 I_n(g+\gamma M_c^2)^2}{\gamma^2 x_c}+\frac{2\alpha_B^2 I_n g(5x_c-3)(g+\gamma M_c^2)}{\gamma^2 x_c(x_c-1)}\\ &-\frac{M_c^2(5x_c-3)}{x_c(\gamma-1)(x_c-1)}\frac{(\beta_c+\frac{3}{2\gamma})}{(1+\beta_c)}-\frac{8\alpha_B^2 I_n g(g+\gamma M_c^2)}{\gamma^2(1+\beta_c)x_c}\\ &+\frac{2[3+\beta_c(\gamma+1)]M_c^2}{\gamma(\gamma-1)(1+\beta_c)^2 x_c}-\frac{M_c^2}{\gamma(\gamma-1)(1+\beta_c)(x_c-1)}\\ &-\frac{(4\zeta-1)M_c^2}{2\gamma(\gamma-1)(1+\beta_c)x_c},\end{aligned}$$

$$\mathcal{C} = -\frac{4\lambda_c \alpha_B I_n M_c (g + \gamma M_c^2)}{\gamma x_c^2},$$

$$\mathcal{D} = -\left[\frac{\lambda_c^2}{x_c^3} - \frac{1}{2(x_c - 1)^2}\right]$$
$$\times \left[\frac{[3 + \beta_c(\gamma + 1)]M_c^2}{(1 + \beta_c)(\gamma - 1)} - \frac{4\alpha_B^2 g I_n (g + \gamma M_c^2)}{\gamma}\right].$$

Here, the quantities with subscript 'c' indicate their values measured at the sonic point.

Upon solving equation (3.8) for a set of input parameters of the flow, we calculate the sound speed at $x_c$ and then, find the radial velocity of the flow using equation (3.7). Using these quantities in equation (3.3), we investigate the properties of the sonic point. As before, in this Chapter, we are interested to study the properties of the global accretion flow around the black holes and hence, the wind solutions are left aside for future study.

## 3.2 Results

We simultaneously solve the differential equations (3.3), (3.4), (3.5) and (3.6) for a given set of flow parameters to obtain the global transonic accretion solution around black hole. In this analysis, $\dot{m}$, $\alpha_B$ and $\gamma$ are treated as the global parameters of the flow. And, three additional parameters are required in order to start the numerical integration of the above equations from a reference point ($x_{\rm ref}$). These three parameters are $x_{\rm ref}$, angular momentum at $x_{\rm ref}$ ($\lambda_{\rm ref}$) and plasma $\beta$ at $x_{\rm ref}$ ($\beta_{\rm ref}$), respectively and they are treated as the local parameters. With this, we obtain the transonic global accretion solutions that may contain shock waves. It is to be noted that we present angular momentum ($\lambda_{\rm ref}$) in terms of Keplerian angular momentum $\lambda_K$ ($\equiv \sqrt{x_{\rm ref}^3/2(x_{\rm ref} - 1)^2}$) all throughout the Chapter.

### 3.2.1 Global accretion solution

In Fig. 3.1, we present the 'phase space diagrams' of accretion solutions where the Mach number ($M = v/a$) is plotted as function of the logarithmic radial distance ($x$). Here, we consider the inner sonic point ($x_{\rm in}$) as the reference point ($x_{\rm ref}$) and choose $x_{\rm in} = 2.41$. The angular momentum and the plasma $\beta$ at $x_{\rm in}$ are kept fixed as $\lambda_{\rm in} = 0.9327\lambda_K$ and $\beta_{\rm in} = 20$, respectively. Moreover, we choose $\alpha_B = 0.02$, $\dot{m} = 0.004$

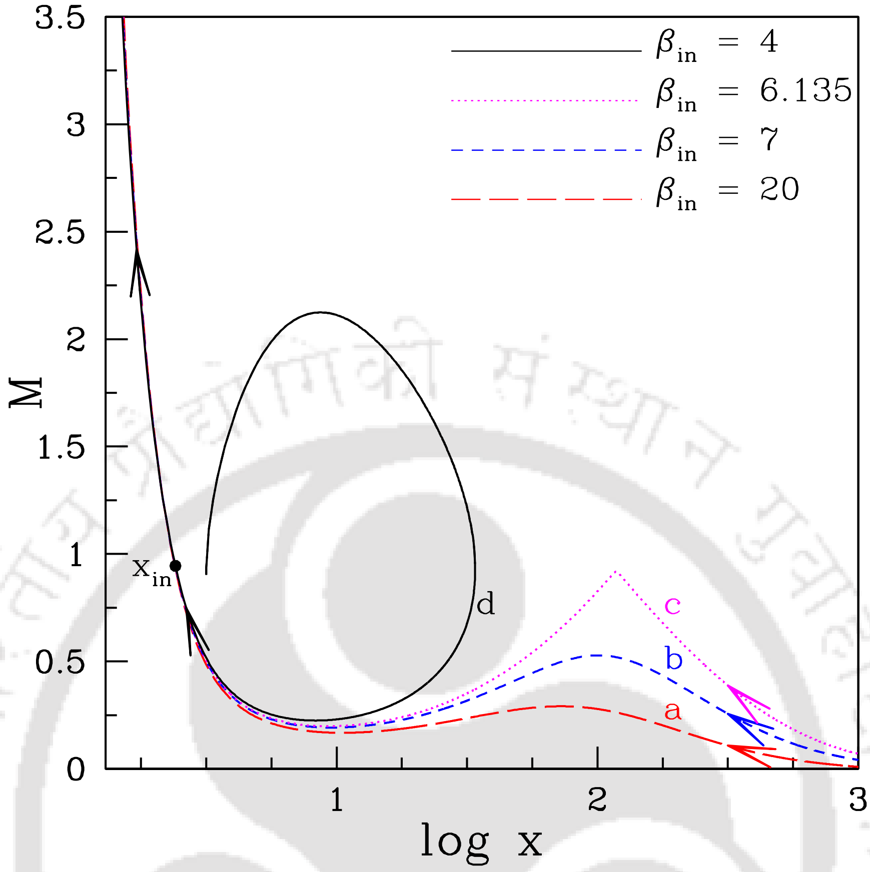

Fig. 3.1 Radial dependence of Mach number ($M = v/a$) of the accreting matter for different values of plasma $\beta$ ($\beta_{\rm in}$) at the inner sonic point $x_{\rm in} = 2.41$. Here, $\lambda_{\rm in} = 0.9327\lambda_K$, $\alpha_B = 0.02$ and $\dot{m} = 0.004$. Long-dashed and short-dashed curves represent the results for $\beta_{\rm in} = 20$ and 7, respectively. For the same set of flow parameters, the minimum values of plasma $\beta$ that provides the accretion solution connecting the inner sonic point to up to a large distance (equivalently 'outer edge of the disc') is obtained as $\beta^{\rm cri}_{\rm in} = 6.135$ and the solution is depicted with the dotted curve. When $\beta_{\rm in} < \beta^{\rm cri}_{\rm in}$, accretion solutions fail to connect to the outer edge of the disc and such a representative solution is depicted by the solid curve for $\beta_{\rm in} = 4$ (Sarkar, Das, and Mandal 2018).

and $\gamma = 4/3$. With this set of parameters, we integrate equations (3.3-3.6) starting from the inner sonic point once inward up to black hole horizon and then outward up to a large distance (equivalently 'outer edge of the disc') . Upon joining them, ultimately we get a global transonic accretion solution as it connects the outer edge of the disc with the black hole horizon. In the figure, this solution is plotted with long-dashed curve and marked as 'a'. The arrow indicates the direction of the flow. Next, we decrease plasma $\beta$ at $x_{\rm in}$ as $\beta_{\rm in} = 7$ and calculate the global transonic accretion solution keeping the remaining flow parameters fixed. The obtained result is plotted using short dashed curve and marked with ‘b’. We observe that the qualitative feature of the solution ‘b’ is very much similar to solution ‘a’. With the gradual decrease of $\beta_{\rm in}$, we obtain a critical value $\beta^{cri}_{\rm in} = 6.135$ corresponding to the chosen set of flow parameters, which is the minimum value of $\beta_{\rm in}$ that provides a transonic global accretion solution passing through the inner sonic point. This solution is plotted with the dotted curve and marked as ‘c’. Needless to mention that the curves marked with ‘a-c’ represent the results identical to the well known advection dominated accretion flow (ADAF) solutions around black holes (Narayan, Kato, and Honma 1997, Oda *et al.* 2007). When $\beta_{\rm in} < \beta^{cri}_{\rm in}$, transonic accretion solution fails to extend up to the outer edge of the disc and does not represent a complete global accretion solution. For representation, we obtain such a solution for $\beta_{\rm in} = 4$ which is illustrated with solid curve and marked as ‘d’.

Apparently, solution ‘d’ in Fig. 3.1 does not connect the black hole horizon with the outer edge of the disc. However, solutions of this kind are potentially promising in the sense that they can be joined with the another transonic accretion solution passing through the outer sonic point ($x_{\rm out}$) via shock transition. The complete description of such a composite global accretion solution can be visualized in the following manner. The rotating subsonic accretion flow at the outer edge of the disk slowly gains its radial velocity due to the attraction of gravity. Subsequently, flow becomes supersonic after passing through $x_{\rm out}$ and continues to proceed towards the black hole. In the vicinity of the black holes, since the viscous timescale greatly exceeds over the infall timescale, the angular momentum transport due to viscosity becomes feeble and therefore, centrifugal repulsion becomes comparable to the gravitational force there. As a result, infalling matter experiences a virtual barrier and eventually slows down. This causes the piling of matter and develops local turbulence that establishes entropy generation leading towards the triggering of shock transition provided the shock conditions are satisfied. In fact, according to the second law of thermodynamics, the presence of the shock wave in accretion flows is thermodynamically preferred when the post-shock flow possesses high entropy content (Becker and Kazanas 2001). The entropy content of a dissipative accretion flow is obtained as (Chakrabarti 1996a),

$$\dot{\mathcal{M}}(x) \propto \left(\frac{\beta}{1+\beta}\right)^n a^{(2n+1)} \upsilon x^{3/2} (x-1), \tag{3.9}$$

where $n = 1/(\gamma - 1)$ is the polytropic index of the flow. In the absence of any dissipative processes, namely viscosity and/or radiative cooling, $\dot{\mathcal{M}}$ remains constant throughout the flow except at the shock transition.

As already described in Chapter 2, in an accretion disk, transition of flow variables in the form of shock wave is manifested through the conservation laws of mass, momentum, energy and magnetic field (Sarkar and Das 2016; and reference therein). Across the shock front, these laws are explicitly expressed as the continuity of (a) mass flux ($\dot{M}_- = \dot{M}_+$) (b) the momentum flux ($W_- + \Sigma_- v_-^2 = W_+ + \Sigma_+ v_+^2$) (c) the energy flux ($\mathcal{E}_- = \mathcal{E}_+$) and (d) the magnetic flux ($\dot{\Phi}_- = \dot{\Phi}_+$), respectively where, the quantities with subscripts '$-$' and '$+$' refer their values before and after the shock. Here, we calculate the local energy of the flow as (Fukue 1990, Samadi, Abbassi, and Khajavi 2014),

$$\mathcal{E}(x) = \frac{v^2}{2} + \frac{a^2}{\gamma - 1} + \frac{\lambda^2}{2x^2} - \frac{1}{2(x-1)} + \frac{< B_\phi^2 >}{4\pi\rho}, \tag{3.10}$$

where all quantities have their usual meaning. Employing these shock conditions, in the next, we calculate the shock location and its various properties knowing the flow parameters.

Toward this, we choose the flow parameters at the inner sonic point ($x_{\rm in}$) as in the case 'd' of Fig. 3.1. Following the method described in Chakrabarti and Das (2004), using the shock conditions, we then uniquely determine the outer sonic point location ($x_{\rm out}$) and other flow variables of the accretion flow at $x_{\rm out}$ for the chosen inner sonic point. Utilizing these flow variables at $x_{\rm out}$, we integrate equations (3.3-3.6) outward up to the outer edge of the disc (chosen as $x = 1000$) in order to obtain a complete global accretion solution including shock waves. We present the result in Fig. 3.2, where Mach number ($M$) is plotted as function of logarithmic radial distance. In reality, the obtained solution is needed to be visualized in the following way. The inflowing matter is injected subsonically from the outer edge of the disc at $x_{\rm edge} = 1000$. Flow becomes supersonic after crossing the outer sonic point at $x_{\rm out} = 369.98$ and continue to proceed towards the horizon. This is shown by thick solid curve. Flow may continue its journey even further as shown by thick dotted curve, but eventually shock conditions are satisfied at $x_s = 22.36$ and hence, supersonic flow undergoes a discontinuous transitions in the form of shock waves to become subsonic. This is indicated by the vertical arrow. Due to gravity, subsonic flow again gains its radial velocity and ultimately enters in to the black hole supersonically after passing through the inner sonic point at $x_{\rm in} = 2.41$. This part of the solution is depicted using thin solid

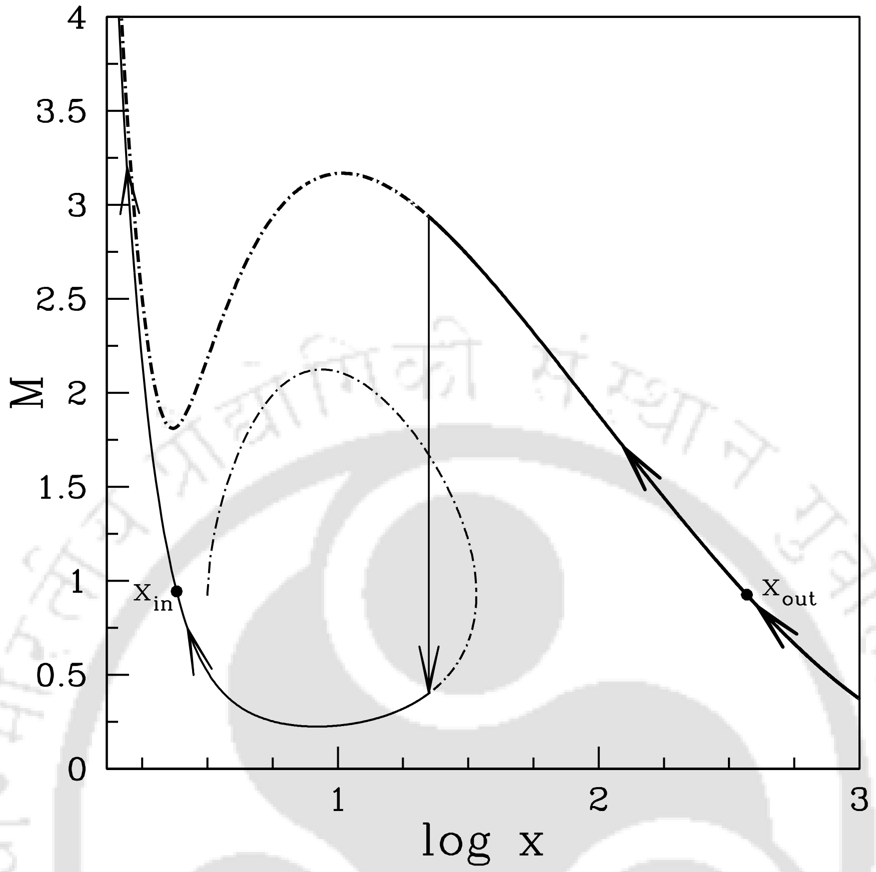

Fig. 3.2 Illustration of a complete global accretion solution including shock transition in the log $x - M$ plane. Inner sonic point ($x_{\rm in}$) and outer sonic point ($x_{\rm out}$) are marked. Arrows indicate the direction of the flow motion and vertical arrow represents the shock transition. Flow parameters used here are same as Fig. 3.1(d). See text for details (Sarkar, Das, and Mandal 2018).

curve. In the figure, $x_{\rm in}$ and $x_{\rm out}$ are marked. Arrows indicate the overall direction of the flow motion towards the black hole.

In the next figure, we examine the effects of the dissipation parameters ($\beta_{\rm edge}$ and/or $\dot{m}$) on the dynamics of shock location for flows with fixed initial parameters. In Fig. 3.3, inflowing matter is injected subsonically from the outer edge of the disc at $x_{\rm edge} = 500$ with specific energy $\mathcal{E}_{\rm edge} = 1.025 \times 10^{-3}$, angular momentum $\lambda_{\rm edge} = 0.1386\lambda_K$ and $\alpha_B = 0.02$. When the accretion rate and the plasma $\beta$ at $x_{\rm edge} = 500$ are chosen as $\dot{m} = 0.0001$ and $\beta_{\rm edge} = 10^4$, respectively, flow encounter shock transition at $x_s = 72.79$. In the figure, solid curve represents this result where the vertical arrow indicates the shock location. The corresponding inner and outer sonic points flow variables are given

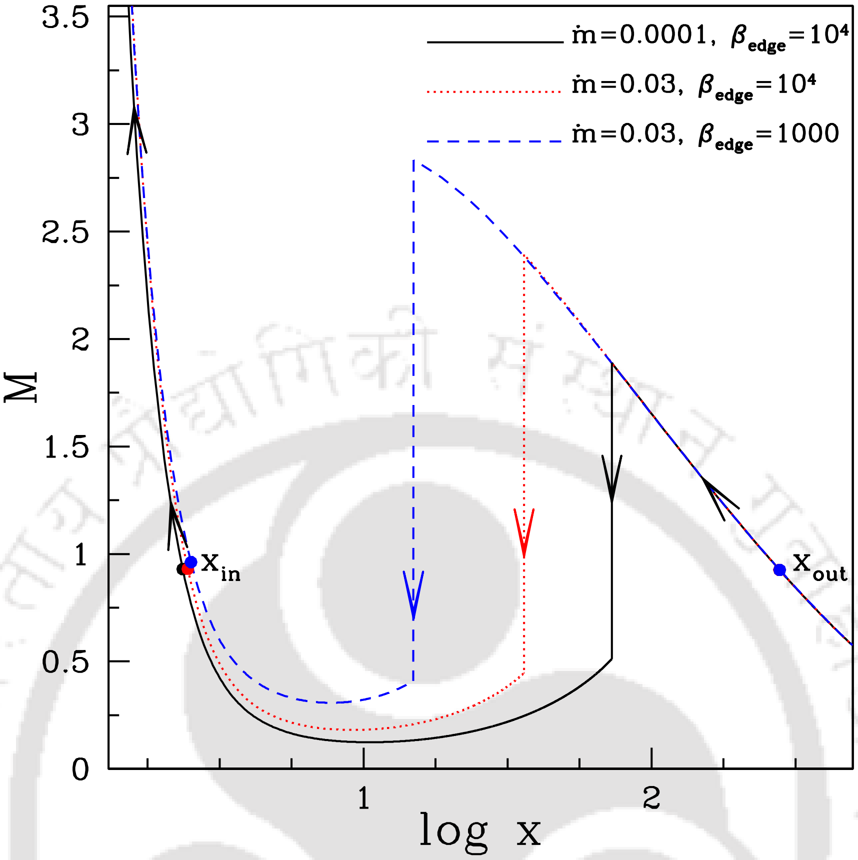

Fig. 3.3 Variation of Mach number as function of logarithmic radial distance. Flows are injected from the outer edge $x_{\rm edge} = 500$ with energy $\mathcal{E}_{\rm edge} = 1.025 \times 10^{-3}$, angular momentum $\lambda_{\rm edge} = 0.1386\lambda_K$ and viscosity $\alpha_B = 0.02$. Solid, dotted and dashed curves depict the results obtained for $(\dot{m},\ \beta_{\rm edge}) = (10^{-4}, 10^4)$, $(0.03, 10^4)$ and $(0.03, 10^3)$, respectively. Vertical arrows indicate the corresponding shock transitions positioned at $x_s = 72.79$ (solid), $x_s = 36.11$ (dotted) and $x_s = 14.88$ (dashed). See text for details (Sarkar, Das, and Mandal 2018).

in table 3.1. Next, we increase the accretion rate as $\dot{m} = 0.03$, keeping all the remaining flow parameters fixed at $x_{\rm edge}$ and observe that the shock front moves towards the horizon at $x_s = 36.11$. This result is depicted using dotted curve where the dotted vertical arrow represents the shock transition. Increase of $\dot{m}$ evidently enhances the cooling rate of the flow. Since density and temperature of the flow are boosted up in the post-shock flow (PSC), effect of cooling at PSC is more intense compared to pre-shock flow and therefore, it reduces thermal pressure that cause the shock front to move close to the horizon in order to maintain pressure balance across the shock front. Further, we fix $\beta_{\rm edge} = 1000$ and $\dot{m} = 0.03$ keeping the other flow parameters

Table 3.1 Flow variables measured at the sonic points for a shock induced global accretion solution. See text for details (Sarkar, Das, and Mandal 2018).

| Sonic Point | $x_c$ | $\lambda_c$ | $\beta_c$ | $v_c$ | $a_c$ |
|---|---|---|---|---|---|
| Inner | 2.3550 | $0.9392\lambda_K$ | 24.9315 | 0.15333 | 0.16495 |
| Outer | 278.3447 | $0.1706\lambda_K$ | 6132.3040 | 0.02648 | 0.028598 |

Note: Subscript ‘c’ refers to the quantities measured at sonic points. For inner (outer) sonic point, ‘c’ is identified with ‘in’ (‘out’).

unchanged at $x_{\rm edge}$ and obtain the shock location at $x_s = 14.88$. We plot this result by dashed curve where dashed vertical line denotes shock location as before. Lowering of $\beta_{\rm edge}$ demonstrates the increase of turbulent magnetic fields in the accretion flow that eventually leads to increase of Maxwell stress and therefore, the angular momentum transport from the inner part of the disc to the outer part of the disc is enhanced. This results the weakening of the centrifugal repulsion at PSC. Moreover, decrease of $\beta_{\rm edge}$ eventually increases the synchrotron cooling efficiency as well. Overall, with the combined effects of both physical processes, shock front is pushed even further towards the horizon. This exhibits the fact that apart from $\dot{m}$, the role of $\beta_{\rm edge}$ is also important in determining the dynamics of shock location.

In Fig. 3.4, we illustrate the vertically averaged accretion disc structure corresponding to the solutions depicted in Fig. 3.3. In each panel, we plot the variation of a flow variable with logarithmic radial distance where the vertical arrows indicate the shock transition. Here, we consider $M_{\rm BH} = 10M_\odot$ as a fiducial value. In Fig. 3.4(a), we demonstrate the radial velocity profile ($v$) of the accretion flow. As expected, $v$ increases with the decrease of radial coordinate until it undergoes a shock transition. Across the shock, $v$ drops down to a subsonic value and again increases gradually in the post-shock region. Finally flow enters in to the black hole with velocity comparable to the speed of light after passing through the inner sonic point. Here, solid, dotted and dashed curves represent results for $(\dot{m}, \beta_{\rm edge}) = (10^{-4}, 10^4)$, $(0.03, 10^4)$ and $(0.03, 10^3)$, respectively. We show the density profile of the flow in Fig. 3.4(b), where we observe the rise of density immediately after the shock transition in every cases. This happens due to the the reduction of radial velocity at PSC and eventually preserves the conservation of mass flux across the shock front. The overall density profile corresponding to $\dot{m} = 0.03$ is higher compared to the case of $\dot{m} = 10^{-4}$ simply because the large $\dot{m}$ stands for higher mass inflow at the outer edge. In Fig. 3.4(c), the proton temperature profile ($T_p$) is shown. Across the shock front, supersonic pre-shock flow is turned into

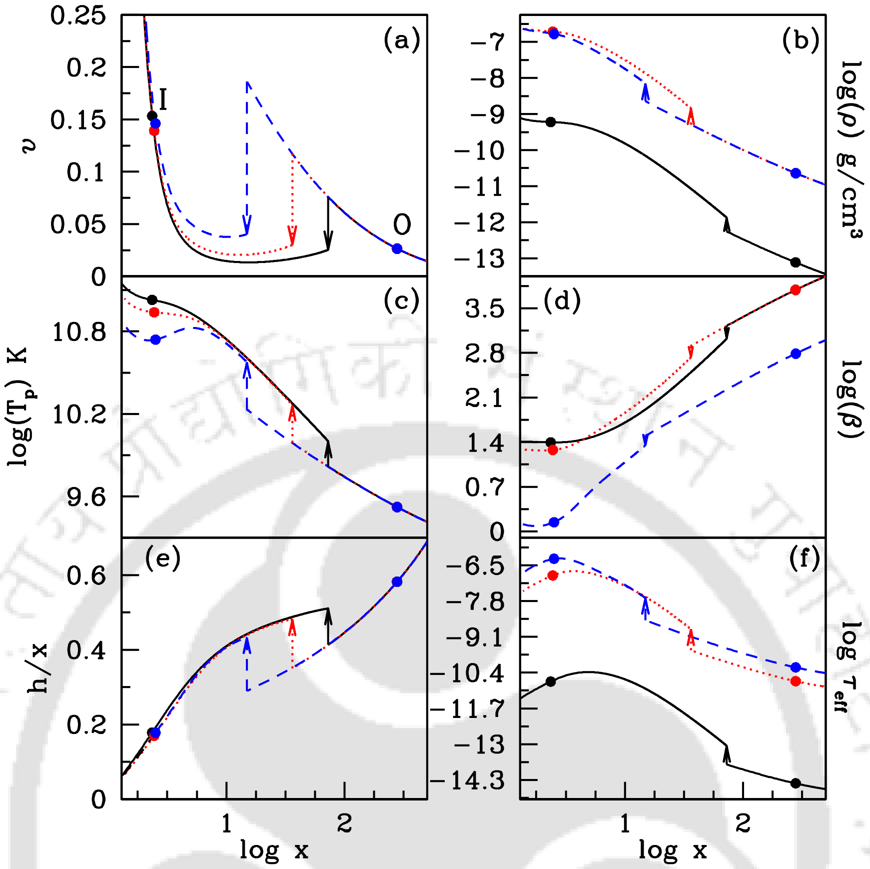

Fig. 3.4 Variation of (a) radial velocity, (b) density in g/cm$^3$, (c) Temperature (d) ratio of gas pressure to magnetic pressure, (e) disc scale height ($h/x$) and (f) effective optical depth as function of logarithmic radial coordinate. Results plotted with solid, dotted and dashed curves correspond to the accretion solution depicted in Fig. 3.3. Filled circles represent the sonic points where the closer one is the inner sonic point and the furthest one is the outer sonic point. Vertical arrows indicate the shock position. See text for details (Sarkar, Das, and Mandal 2018).

the subsonic flow and therefore, most of the kinetic energy of the infalling matter is converted to the thermal energy at PSC. This eventually leads to the heating of the PSC as indicated by the rise of post-shock temperature profile. Interestingly, when $\dot{m}$ is increased, the effect of cooling becomes more effective at PSC that causes the reduction of $T_p$ as clearly seen close to the inner part of the disc. In addition, we observe that the decrease of $\beta_{\rm edge}$ essentially exhibits the reduction of the temperature profile of the accretion flow. This finding is in agreement with the results of numerical simulation (Machida, Nakamura, and Matsumoto 2006) which yields a cooler disk structure for a magnetically dominated accretion flow. In Fig. 3.4(d), we show the radial variation of plasma $\beta$. We find that $\beta$ decreases as the flow approaches to the black hole. Moreover, $\beta$ falls down sharply across the shock that turns PSC into magnetically dominated. The radial dependence of the vertical scale-height $(h/x)$ is presented in Fig. 3.4(e). The validity of the thin disc approximation is observed all throughout from the outer edge to the horizon even in the presence of shock transition. Finally, in Fig. 3.4(f), we demonstrate the variation of effective optical depth, $\tau_{\rm eff} = \sqrt{\tau_{\rm es}\tau_{\rm syn}}$ where, $\tau_{\rm es}$ represents the scattering optical depth given by $\tau_{\rm es} = \kappa_{\rm es}\rho h$ and the electron scattering opacity, $\kappa_{\rm es}$, is taken to be $\kappa_{\rm es} = 0.38$ cm$^2$g$^{-1}$. Here, $\tau_{\rm syn}$ denotes the absorption effect arising due to thermal processes and is given by $\tau_{\rm syn} = \left(hq_{\rm syn}/4\sigma T_e^4\right)(2GM_{BH}/c^2)$ where, $q_{\rm syn}$ is the synchrotron emissivity (Shapiro and Teukolsky 1983) and $\sigma$ is the Stefan-Boltzmann constant. We find that the optical depth of PSC is always greater than the pre-shock region as the density in the post-shock region is higher (see, Fig. 3.4b). In addition, the overall variation of the optical depth for enhanced accretion rate remains higher all throughout. Moreover, in spite of the steep density profile, PSC is found to remain optically thin $(\tau < 1)$. This apparently indicates that the possibility of escaping hard radiations from the PSC seems to be significant.

Fig. 3.5, illustrates the various shock properties as function of accretion rate $(\dot{m})$ for flows injected from a fixed outer edge as $x_{\rm edge} = 500$ with $\beta_{\rm edge} = 1400$, energy $\mathcal{E}_{\rm edge} = 1.025 \times 10^{-3}$ and viscosity $\alpha_B = 0.02$. In the upper panel (Fig. 3.5a), the variation of shock location is shown for three different values of angular momentum $(\lambda_{\rm edge})$ at $x_{\rm edge}$. The solid, dotted and dashed curves correspond to flows injected with angular momentum $\lambda_{\rm edge} = 0.13757\lambda_K$, $0.13865\lambda_K$ and $0.13972\lambda_K$, respectively. From the figure, it is evident that a wide range of $\dot{m}$ provides shock induced global accretion solutions. For a given $\lambda_{\rm edge}$, the shock position advances towards the horizon with the increase of accretion rate $(\dot{m})$. The increase of accretion rate enhances the efficiency of radiative cooling and the flow loses energy during accretion. Loss of energy leads to drop in post-shock thermal pressure and hence the shock front moves closer to the horizon in order to maintain pressure balance across the shock. When accretion rate is crossed its critical value $(\dot{m}^{\rm cri})$, standing shock fails to form as the shock conditions are no longer satisfied. This clearly provides an indication that the possibility of shock formation reduces with the increase of $\dot{m}$. It is to be noted that $\dot{m}^{\rm cri}$ does not possess a global value, instead it largely depends on the accretion flow parameters. Interestingly, when $\dot{m} > \dot{m}^{\rm cri}$, flow may contain oscillatory shocks, however, the analysis of non-steady shock properties are beyond the scope of the present work. In addition, for a given $\dot{m}$, shock front moves outwards from the horizon when $\lambda_{\rm edge}$ is increased. This happens

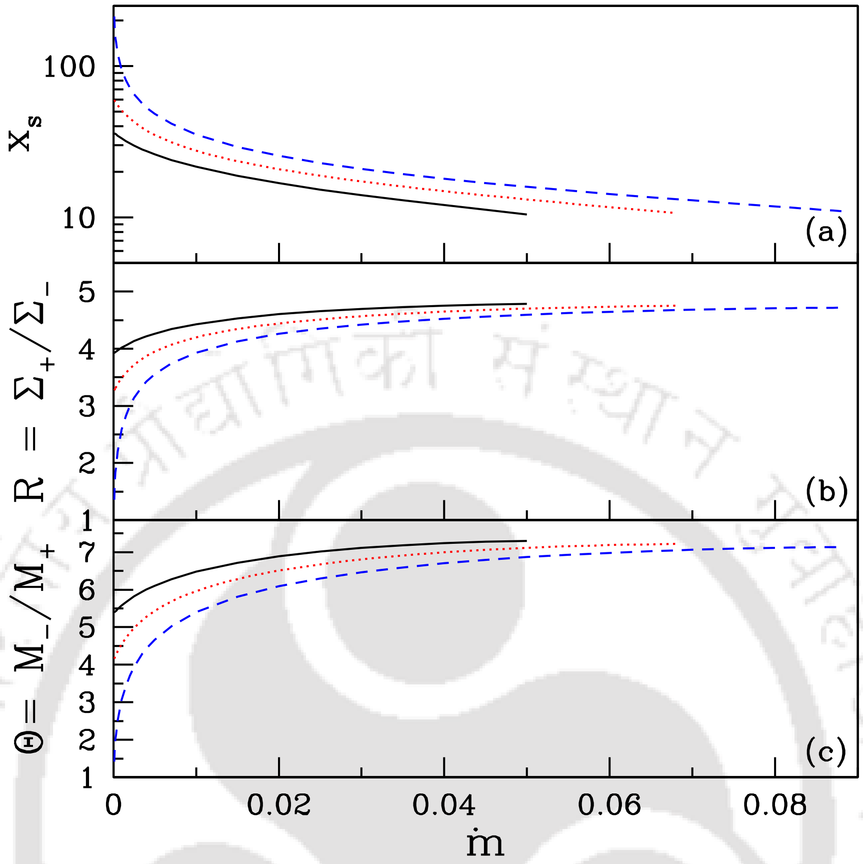

Fig. 3.5 Variation of (a) shock location $x_s$, (b) compression ratio $R$, and (c) shock strength $\Theta$ as function of $\dot{m}$ for flows injected from $x_{\rm edge} = 500$ with $\alpha_B = 0.02$, $\beta_{\rm edge} = 1400$ and $\mathcal{E}_{\rm edge} = 1.025 \times 10^{-3}$. Solid, dotted and dashed curves represent the results corresponding to $\lambda_{\rm edge} = 0.13757\lambda_K$, $0.13865\lambda_K$ and $0.13972\lambda_K$, respectively. See text for details (Sarkar, Das, and Mandal 2018).

due to the fact that the centrifugal barrier becomes stronger with the increase of $\lambda_{\rm edge}$ which clearly indicates that the shocks are centrifugally driven.

It is already pointed out that the density and temperature of the PSC is increased due to the effect of shock compression. Moreover, the spectral properties of an accretion disc are directly dependent on the density and temperature distribution of the flow. Therefore, it is worthy to measure the amount of density and temperature enhancement across the shock transition. Towards this, we first compute the compression ratio which is defined as the ratio of the vertically averaged post-shock density to the pre-shock density ($R = \Sigma_+/\Sigma_-$) and plot it as function of $\dot{m}$ in Fig. 3.5(b). The flow parameters are chosen as in Fig. 3.5(a). For fixed $\lambda_{\rm edge}$, $R$ is found to increase monotonically with the increase of $\dot{m}$. This happens because shock front is pushed towards the horizon

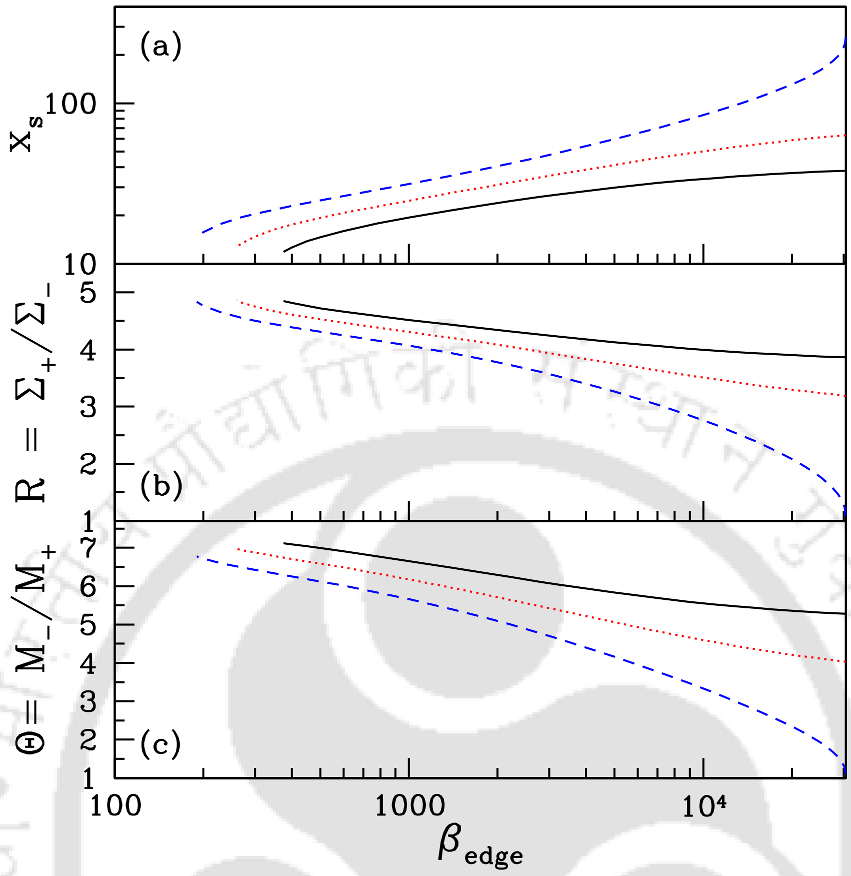

Fig. 3.6 Variation of (a) the shock location $x_s$ (b) shock compression ratio $R$ and (c) shock strength $\Theta$ as function of $\beta_{\rm edge}$ for different values of $\lambda_{\rm edge}$. Flows are injected from $x_{\rm edge} = 500$ with $\mathcal{E}_{\rm edge} = 1.025 \times 10^{-3}$, $\alpha_B = 0.02$ and $\dot{m} = 0.01$, respectively. Results depicted with solid, dotted and dashed curves are for $\lambda_{\rm edge} = 0.13757\lambda_K$, $0.13865\lambda_K$ and $0.13972\lambda_K$, respectively. See text for details (Sarkar, Das, and Mandal 2018).

with the increase of $\dot{m}$ that boosted the density compression and subsequently increases the compression ratio. On the contrary, for fixed $\dot{m}$, when $\lambda_{\rm edge}$ is increased, shock recedes away due to the stronger centrifugal barrier causing the decrease of post-shock compression. Since shock ceases to exist for $\dot{m} > \dot{m}^{\rm cri}$, we observe a cut-off in $R$ for all the cases. Next, we calculate the strength of the shock ($\Theta$) which is defined as the ratio of pre-shock Mach number ($M_-$) to the post-shock Mach number ($M_+$) and it is essentially measures the temperature jump across the shock. In Fig. 3.5(c), we show the variation of $\Theta$ as function of $\dot{m}$ for the same set of flow parameters as in Fig. 3.5(a). We find that the response of $\Theta$ on the increase of $\dot{m}$ is similar to $R$ as described in Fig. 3.5(b).

In Fig. 3.6, we proceed to explore the shock properties in terms of $\beta_{\rm edge}$ for flows with same outer boundary values, namely, $x_{\rm edge} = 500$, $\mathcal{E}_{\rm edge} = 1.025 \times 10^{-3}$, $\alpha_B = 0.02$ and $\dot{m} = 0.01$. The solid, dotted and dashed curves represent results corresponding to $\lambda_{\rm edge} = 0.13757\lambda_K$, $0.13865\lambda_K$ and $0.13972\lambda_K$, respectively. Here also we observe that the shock front proceeds towards the horizon with the decrease of $\beta_{\rm edge}$ for all cases having different $\lambda_{\rm edge}$. When $\beta_{\rm edge}$ is reduced, the effect of synchrotron cooling is increased due to the increase of magnetic activity and therefore, shock moves inward. However, the indefinite reduction of $\beta_{\rm edge}$ is not possible keeping the remaining flow parameters unchanged because under a critical limit ($\beta^{\rm cri}_{\rm edge}$), shock ceases to exist. As in Fig. 3.5b-c, here also we study the variation of compression ratio ($R$) and the shock strength ($\Theta$) as function of $\beta_{\rm edge}$. We find that both $R$ and $\Theta$ display anti-correlation relation with $\beta_{\rm edge}$.

Next, we study the properties of shock wave in terms of viscosity ($\alpha_B$). While doing so, as before, we choose the flow injection parameter as $x_{\rm edge} = 500$, $\mathcal{E}_{\rm edge} = 1.025 \times 10^{-3}$, $\beta_{\rm edge} = 1400$ and $\dot{m} = 0.01$. We depict the results in Fig. 3.7 where, solid, dotted and dashed curve are obtained for $\lambda_{\rm edge} = 0.13757\lambda_K$, $0.13865\lambda_K$ and $0.13972\lambda_K$, respectively. We observe that shock forms for a wide range of $\alpha_B$. The shock position is reduced with the increase of $\alpha_B$ for all cases having different $\lambda_{\rm edge}$. Increase of $\alpha_B$ enhances the angular momentum transport outwards that causes the weakening of the centrifugal barrier and hence the shock is pushed towards the horizon. When $\alpha_B$ is chosen beyond its critical value ($\alpha^{\rm cri}_B$), shock conditions are not satisfied and therefore, standing shock ceases to exist. Needless to mention that $\alpha^{\rm cri}_B$ largely depends on the other accretion flow parameters. When $\alpha > \alpha^{\rm cri}_B$, sub-Keplerian flow deviates from the Keplerian disc very close to the horizon and flow enters into the black hole after passing through a single sonic point. Further, we calculate the compression ratio ($R$) and the shock strength ($\Theta$) for flows described in Fig. 3.7(a) and present the obtained results in Fig. 3.7(b)-(c). We observe that both $R$ and $\Theta$ are gradually increased with $\alpha_B$.

So far, we have examined the properties of shock induced global accretion solutions for flows having adiabatic index $\gamma = 4/3$. In reality, the limiting values of $\gamma$ lie in the range between 4/3 to 5/3, depending on the ratio of the thermal energy and the rest energy of the flow (Frank, King, and Raine 2002). Keeping this in mind, we now intend to compute the critical viscosity parameter ($\alpha^{\rm cri}_B$) as function of $\beta_{\rm in}$ that allows shocked accretion solution. While doing this, we consider thermally ultra-relativistic flow ($\gamma \sim 4/3$) and thermally semi-non-relativistic flow ($\gamma \sim 1.5$) (Kumar, Chattopadhyay,

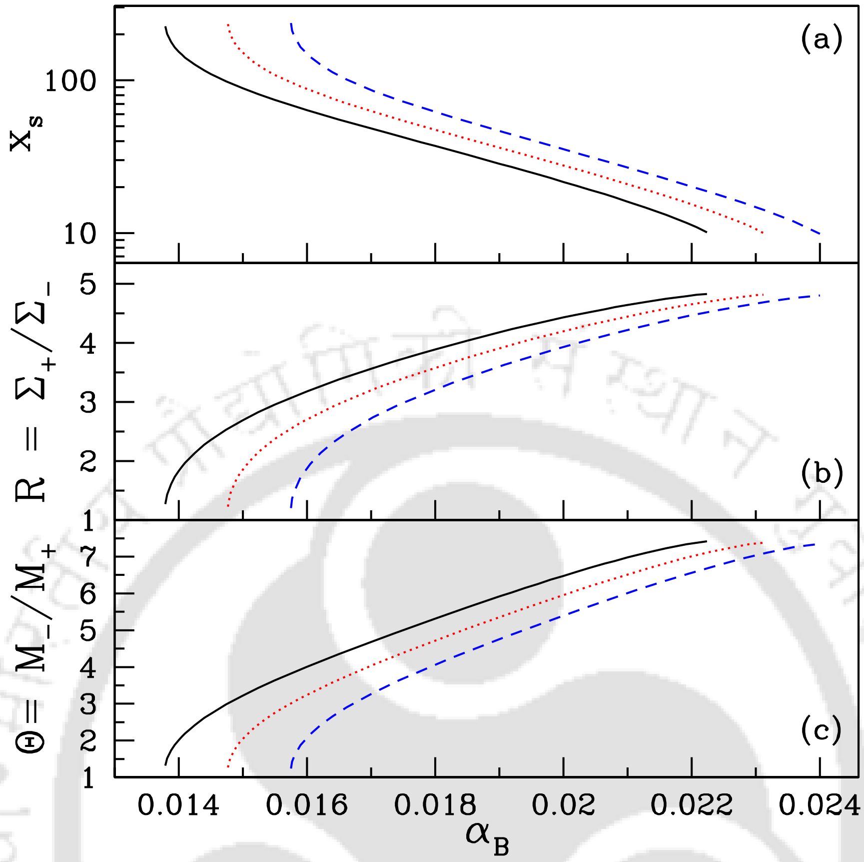

Fig. 3.7 Variation of (a) the shock location $x_s$ (b) shock compression ratio $R$ and (c) shock strength $\Theta$ as function of viscosity $\alpha_{\rm B}$ for different values of $\lambda_{\rm edge}$. Flows are injected from $x_{\rm edge} = 500$ with $\mathcal{E}_{\rm edge} = 1.025 \times 10^{-3}$, $\beta_{\rm edge} = 1400$ and $\dot{m} = 0.01$. Results drawn with solid, dotted and dashed curves are for $\lambda_{\rm edge} = 0.13757\lambda_K$, $0.13865\lambda_K$ and $0.13972\lambda_K$, respectively. See text for details (Sarkar, Das, and Mandal 2018).

and Mandal 2014, Yuan and Narayan 2014) and obtain $\alpha_B^{\rm cri}$ for both the extreme cases as depicted in Fig. 3.8. Here, we assume $\dot{m} = 0.01$. Filled and open circles joined using the solid line represent the results corresponding to $\gamma = 4/3$ and 1.5, respectively. In a magnetized accretion flow with a given $\alpha_B$, the transport of angular momentum towards the outer edge of the disc is increased with the decrease of $\beta_{\rm in}$ as the magnetic pressure contributes to the total pressure. Since shocks under consideration are centrifugally driven (see Fig. 3.5), therefore, when $\beta_{\rm in}$ is small, a lower value of $\alpha_B$ is sufficient to transport the required angular momentum for shock formation. Evidently, $\alpha_B^{\rm cri}$ possesses lower value for magnetized flow. As $\beta_{\rm in}$ is increased, $\alpha_B^{\rm cri}$ is also increased and eventually approached towards a saturation value corresponding to the gas pressure dominated flow. For $\gamma = 4/3$, critical viscosity parameter tends to the asymptotic

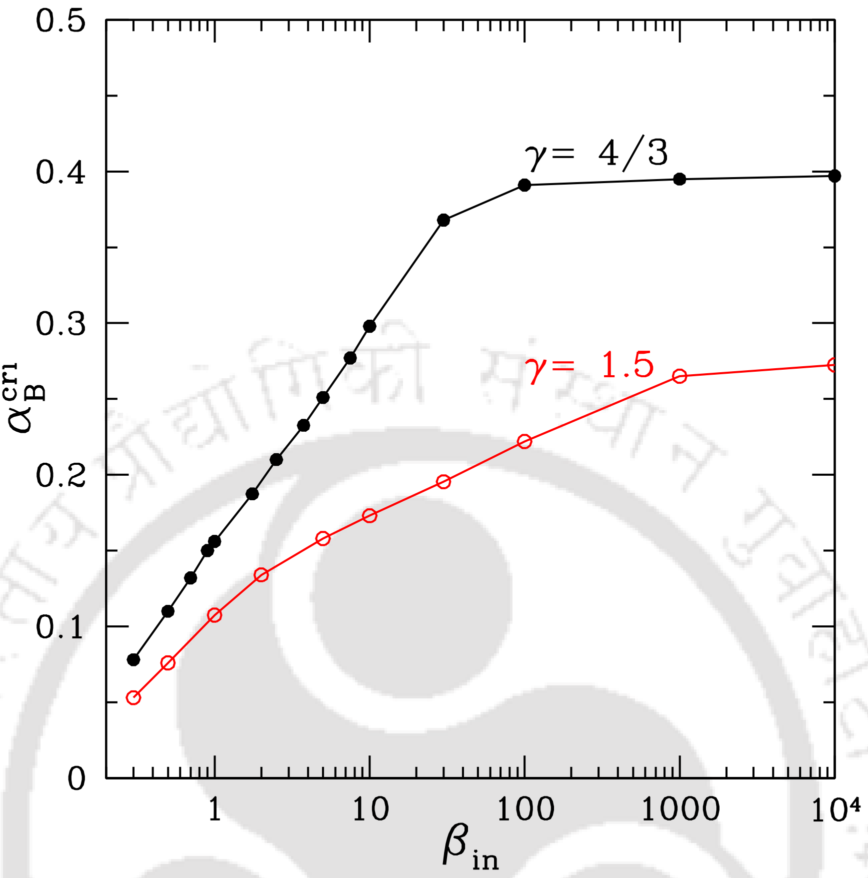

Fig. 3.8 Variation of critical viscosity parameter ($\alpha_B^{\rm cri}$) as function of plasma $\beta$ at inner sonic point ($\beta_{\rm in}$) that allows standing shocks. Here, we choose $\dot{m} = 0.01$. Adiabatic indices are marked. See text for details (Sarkar, Das, and Mandal 2018).

value $\alpha_B^{\rm cri} \sim 0.4$ (Chakrabarti and Das 2004) and for $\gamma = 1.5$, the saturation value is found to be $\alpha_B^{\rm cri} \sim 0.27$ (Das, Becker, and Le 2009, Sarkar and Das 2016). We observe that $\alpha_B^{\rm cri}$ is reduced as the flow changes its character from thermally ultra-relativistic ($\gamma = 4/3$) to thermally semi-non-relativistic limit ($\gamma = 1.5$). This apparently indicates that the possibility of shock transition seems to be feeble when the flow approaches to the non-relativistic regime. This happens due to the fact that when $\gamma$ tends to 5/3, flow possesses only single sonic point (Chakrabarti and Das 2004), thereby reducing the possibility of shock formation.

We continue our investigation to calculate the critical accretion rate of the flow that provides the global accretion solutions including standing shock. In Fig. 3.9, we present the variation of critical accretion rate ($\dot{m}^{\rm cri}$) as function of plasma $\beta$ measured at the inner sonic point ($\beta_{\rm in}$). Here, we choose viscosity parameter as $\alpha_B = 0.01$. In this analysis, we have chosen the wide range of $\beta$ where, $\beta < 1$ represents the magnetic

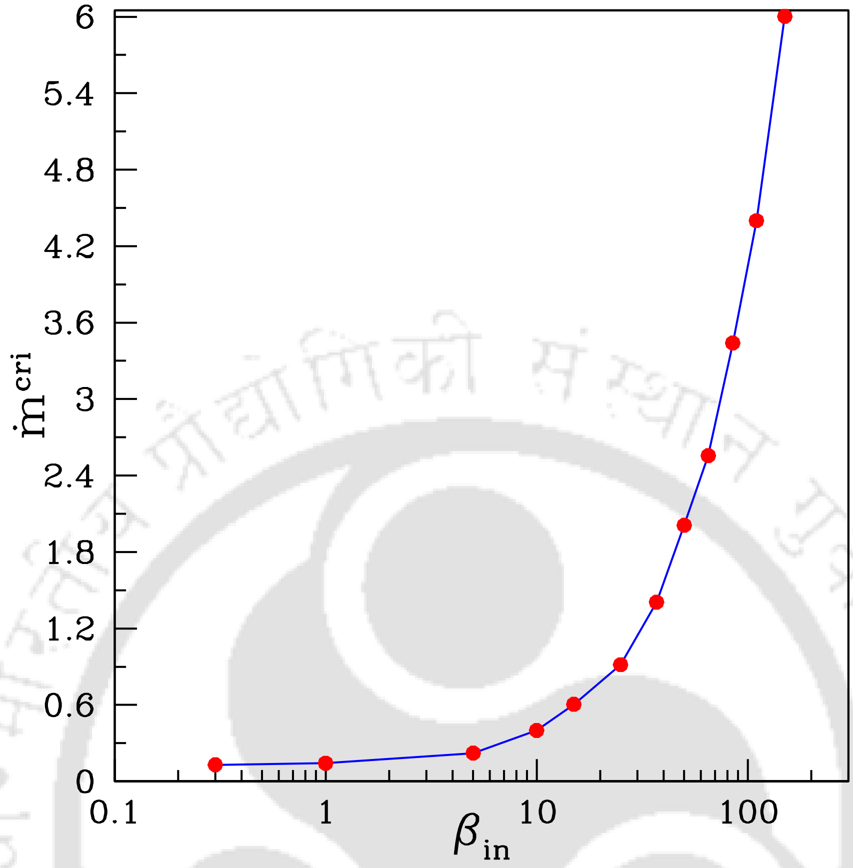

Fig. 3.9 Variation of critical accretion rate $\dot{m}^{\rm cri}$ that allows standing shock as function of $\beta_{\rm in}$. Here, viscosity parameter is chosen as $\alpha_B = 0.01$. See text for details (Sarkar, Das, and Mandal 2018).

pressure dominated flow and $\beta > 1$ denotes the gas pressure dominated flow. Moreover, we consider synchrotron cooling as the effective radiative mechanism active in the flow. Since synchrotron process depends on both the strength of the magnetic fields and the density of accreting matter, one can obtain the required cooling effect by suitably tuning the density and the magnetic fields together. When $\beta_{\rm in} < 1$, the inner part of the disc becomes magnetically dominated as the disc is threaded with strong magnetic fields as compared to the gas dominated disc and therefore, significant cooling effect can be achieved even with small accretion rate. Thus, for magnetically dominated flow, we obtain small values of $\dot{m}^{\rm cri}$. For example, we obtain the magnetic field at $x_{\rm in} = 2.5234$ as $B(x_{\rm in}) = 1.453 \times 10^7$ Gauss for $\lambda_{\rm in} = 0.978185\lambda_K$, $\alpha_B = 0.01$, $\beta_{\rm in} = 0.3$, $\dot{m}^{\rm cri} = 0.13$ and $M_{\rm BH} = 10 M_\odot$, respectively. As we gradually increase the value of $\beta_{\rm in}$, the effect of magnetic fields becomes weaker that eventually decreases the cooling effect in the flow. Hence, flow can sustain standing shock even with relatively large

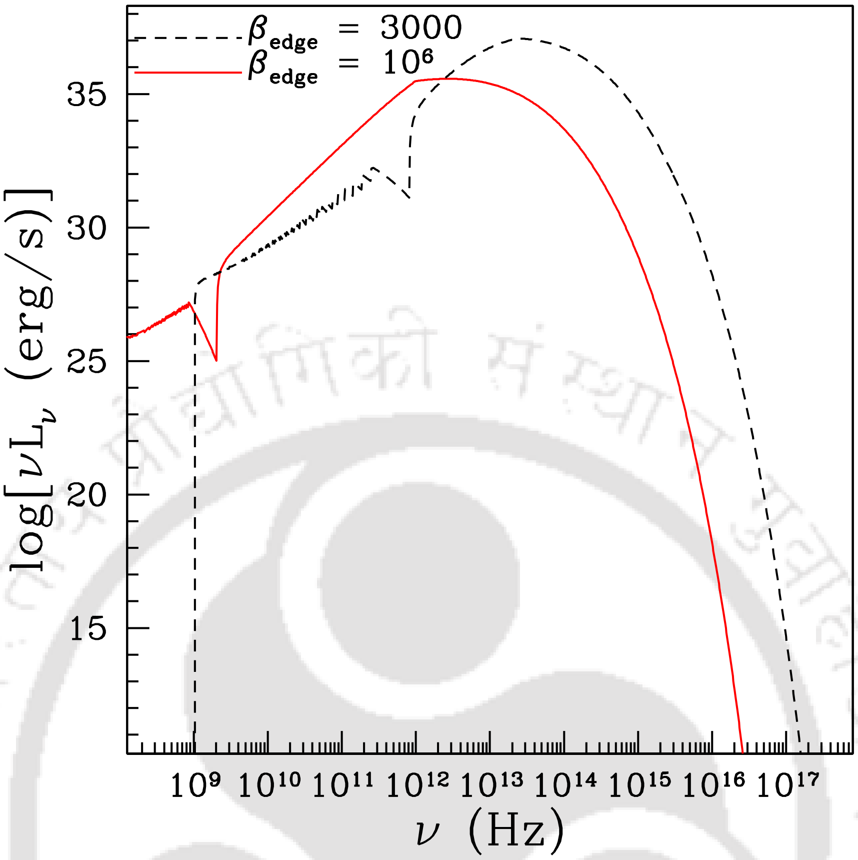

Fig. 3.10 Typical spectra from an accretion disc around a black hole of mass $M = 10\mathrm{M}_\odot$ for a strong and weak accretion shock located at $x_s = 13.14$ and 72.12 respectively. The two different shock locations correspond to flows injected from the outer edge with two different values of $\beta$ as indicated in the figure. See text for details (Sarkar, Das, and Mandal 2018).

accretion rate. When $\beta \gg 1$, magnetic fields are very weak leading to the negligible cooling effect in the flow. Therefore, we are effectively left with a flow where $\dot{m}^{\rm cri}$ tends to become independent of $\beta_{\rm in}$ as observed in the figure.

In Fig. 3.10, we present the typical spectrum for shocked accretion flows injected from outer edge $x_{\rm edge} = 500$ with angular momentum $\lambda_{\rm edge} = 0.13865\lambda_K$ and energy $\mathcal{E}_{\rm edge} = 1.025 \times 10^{-3}$. Here, we consider viscosity as $\alpha_B = 0.02$ and accretion rate as $\dot{m} = 0.1$. For representation, black hole mass is chosen as $M_{\rm BH} = 10M_\odot$. Considering $\beta_{\rm edge} = 10^6$, we obtain the global accretion solution where standing shock is formed at $x_s = 72.12$. Following the works of Mandal and Chakrabarti (2005a); Chakrabarti and Mandal (2006), we compute the disc synchrotron spectrum corresponding to this accretion solution and present it in Fig. 3.10 using solid curve. Further, we increase the effect of magnetic fields by setting $\beta_{\rm edge} = 3000$ and inject the flow keeping the remaing flow variables unaltered. We observe that the flow encounters standing shock transition at $x_s = 13.14$. We then compute the disc spectrum as before and depict it in Fig. 3.10 using dashed curve. In both the cases, the pre-shock (low energy radiation) and post shock (high energy radiation) synchrotron contributions are well separated across the sharp discontinuity due to sudden jump in temperature, density and magnetic field at the shock. The spikes in pre-shock contribution represent the cumulated cyclotron lines coming from different disc annuli. Evidently, lower $\beta$ at outer boundary (dashed curve) corresponds to higher magnetic fields and therefore, the flow will be radiatively more efficient. Accordingly, the spectrum is shifted towards high energy for large magnetic field value. This essentially indicates that the disc is making a transition to a brighter hard state with the decrease of $\beta_{\rm edge}$. The above findings is in agreement with the results of Oda *et al.* (2012), where the brightening of the hard state is reported for disc that makes transition to the low-$\beta$ state.

In the course of our investigation of accretion flow properties, we next put an effort to calculate the disc luminosity. Since we use the synchrotron emission as the potential cooling mechanism while modeling the accretion flows around black holes, the total surface disc luminosity ($L_{\rm disc}$) is estimated as,

$$L_{\rm disc} = 4\pi \int_{x_i}^{x_{\rm f}} Q^{-} x dx,$$

where, the limit $x_i$ refers to the location just outside the horizon and $x_f$ stands for the outer edge of the disc, respectively, and $Q^-$ denotes the synchrotron cooling rate. Here, for a given accretion rate ($\dot{m}$), we compute the maximum disc luminosity ($L_{\rm disc}^{\rm max}$) for shock and shock free accretion solutions by freely varying the remaining flow parameters and show its variation in units of Eddington luminosity as function of $\dot{m}$ in Fig. 3.11. Filled circles joined with the solid line represent the results corresponding to the global accretion solutions including shocks and the open circles connected with the dotted curve are for shock free accretion solutions. Overall, we observe that $L_{\rm disc}^{\rm max}$ increases with $\dot{m}$ for all cases. This happens, simply because the increase of $\dot{m}$ manifests the rise of the flow density that eventually allows the flow to cool down more efficiently. Moreover, we find that for a fixed $\dot{m}$, $L_{\rm disc}^{\rm max}$ remains always higher for shocked accretion flows compared to the shock free flows. In other words, according to our model, the accretion flow containing shock waves are radiatively more efficient than the flows having no shock. Therefore, it is fairly indicative that the shocked accretion solutions

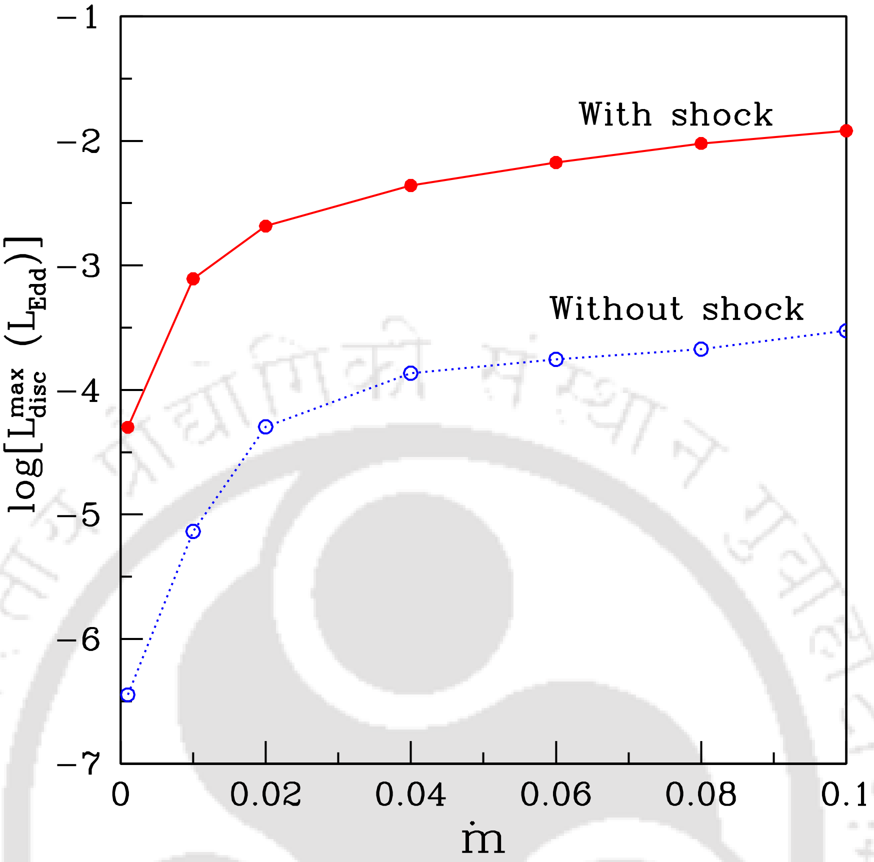

Fig. 3.11 Variation of maximum disc luminosity $L_{\rm disc}^{\rm max}$ as a function of accretion rate $\dot{m}$. Filled circles connected with solid line denote the results for shocked accretion flows whereas the open circles joined with dotted line are for shock free accretion solutions. See text for details (Sarkar, Das, and Mandal 2018).

seems to be potentially more preferred over the shock free solutions in explaining the energetics of black hole sources.

Until now, we have studied the various properties of accretion shock waves around black holes. These shocks are non-dissipative in nature as the specific energy remains conserved across the shock front (Chakrabarti 1989). Indeed, shocks of this kind are radiatively inefficient as well. Apparently, the realistic shock waves are likely to be dissipative, where a part of accreting energy is escaped from the shock location through the disc surfaces. This essentially causes the reduction of the overall specific energy profile in the PSC region (Singh and Chakrabarti 2011). The plausible mechanism that perhaps regulates the energy dissipation at the shock is the thermal Comptonization process (Chakrabarti and Titarchuk 1995) that eventually reduce the thermal energy in the PSC. Based on the above consideration, we assume that the loss of energy across

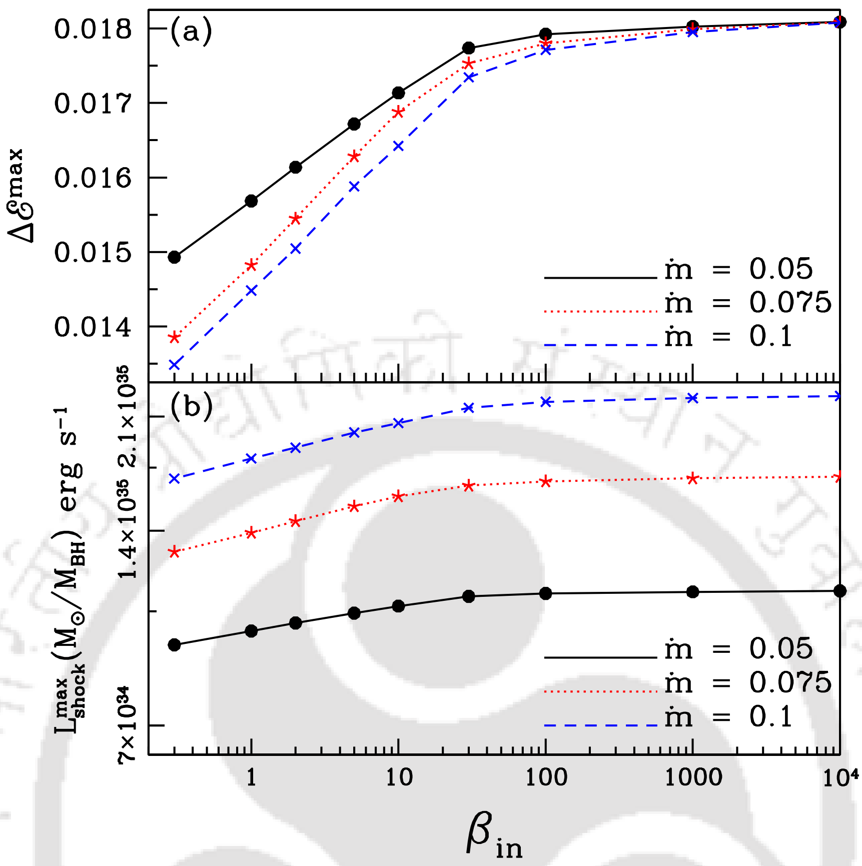

Fig. 3.12 Variation of maximum energy dissipation at shock ($\Delta\mathcal{E}^{\rm max}$) as a function of $\beta$ at inner sonic point ($\beta_{\rm in}$) for three different values of accretion rates, $\dot{m} = 0.05$, 0.075 and 0.1 denoted by solid, dotted and dashed curves, respectively (Sarkar, Das, and Mandal 2018).

the shock front is proportional to the temperature difference between the immediate pre-shock and post shock flow and therefore, the energy loss across the shock front is calculated as (Das, Chakrabarti, and Mondal 2010),

$$\Delta\mathcal{E} = fn(a_+^2 - a_-^2), \tag{3.11}$$

where, $a_-$ and $a_+$ denote the immediate pre-shock and post-shock sound speed and $f$ represents the fraction of the available thermal energy lost at shock. In this analysis, we treat $f$ as a free parameter and chose its value as $f = 0.998$ for representation. Evidently, this is the measure of energy dissipation across the shock (Das, Chakrabarti, and Mondal 2010, Singh and Chakrabarti 2011, Sarkar and Das 2013, Kumar and Chattopadhyay 2013). We then compute the maximum energy dissipation ($\Delta\mathcal{E}^{\rm max}$) by freely varying all the flow parameters and plot it as function of $\beta_{\rm in}$ for various values of accretion rates in Fig. 3.12(a). Here, solid, dotted and dashed curves represent the results corresponding to $\dot{m} = 0.05$, 0.075 and 0.1, respectively. We observe that for a given accretion rate ($\dot{m}$), $\Delta\mathcal{E}^{\rm max}$ initially shows gradual increment with $\beta_{\rm in}$ which eventually approaches towards a saturation value in the gas pressure dominated domain. Meanwhile, it was shown by numerical simulation (Machida, Nakamura, and Matsumoto 2006) that in the magnetically dominated state, accretion disc becomes cool as compared to a gas pressure dominated disc. This clearly indicates that the gas pressure dominated flow is expected to possess higher thermal energy content and accordingly, we obtain enhanced $\Delta\mathcal{E}^{\rm max}$ when $\beta_{\rm in}$ is larger. Moreover, as $\dot{m}$ is increased, cooling becomes more effective in the flow resulting the lowering of thermal energy content. Therefore, for a given $\beta_{\rm in}$, $\Delta\mathcal{E}^{\rm max}$ remains smaller for flows having higher $\dot{m}$. When $\beta_{\rm in}$ is large, the effect of synchrotron cooling due to the increase of accretion rate becomes practically insignificant. Hence, when $\beta_{\rm in} \rightarrow 10^4$, $\Delta\mathcal{E}^{\rm max}$ asymptotes to a saturation value irrespective to the flow accretion rate.

Next, we intend to infer the utility of dissipated energy at the shock ($\Delta\mathcal{E}$) in terms of the observable quantities. Indeed, a portion of the total usable energy available at the PSC is the same dissipative energy $\Delta\mathcal{E}$. Since jets are likely to be launched from the PSC, a part of this energy is used in the process of jet generation. Keeping this in mind, we calculate the maximum kinetic power lost by the disc corresponding to $\Delta\mathcal{E}^{\rm max}$ in terms of shock luminosity as $L^{\rm max}_{\rm shock} = \dot{M} \times \Delta\mathcal{E}^{\rm max} \times c^2$ erg s$^{-1}$ (Le and Becker 2004; 2005, Sarkar and Das 2016). Here, $\dot{M} (\equiv \dot{m}\dot{M}_{edd})$ represents the accretion rate in physical units. With this, in Fig. 3.12(b), we show the variation of the maximum shock luminosity (scaled with black hole mass) as a function of $\beta_{\rm in}$ for various accretion rates ($\dot{m}$). As before, solid, dotted and dashed curves represent the results corresponding to $\dot{m} = 0.05$, 0.075 and 0.1, respectively. Since we calculate the maximum shock luminosity using $\Delta\mathcal{E}^{\rm max}$, the obtained results apparently depend on the accretion rate although it manifest the variations similar to $\Delta\mathcal{E}^{\rm max}$ (see Fig. 3.12a). Consequently, we observe that for a given $\beta_{\rm in}$, the maximum shock luminosity is increased with $\dot{m}$. Based on the above findings, we point out that our model calculation of shock luminosity (as depicted in Fig. 3.12b) can be readily used to understand the observational findings of core radio luminosity values associated with the black hole sources.

## 3.3 Chapter Conclusion

In this Chapter, we study the effect of synchrotron cooling in a magnetized advective accretion flow around a non-rotating black hole. While investigating the various properties of the accretion flow, since the origin of viscosity and the exact mode of angular momentum transport in accretion discs is still remain inconclusive, we rely on the numerical simulation results of Machida, Nakamura, and Matsumoto (2006) and assume that the $x\phi$-component of the Maxwell stress is proportional to the total pressure of the accreting matter. During accretion, flow changes its sonic state from subsonic to supersonic to become transonic before falling into the black hole. The position where flow becomes transonic is called as the sonic point. Depending on the input parameters, flow may pass through the multiple sonic points and the flow of this kind has the potential to exhibit shock phenomenon. Meanwhile, Oda *et al.* (2007; 2012) studied the global accretion solutions of magnetically supported accretion discs around stationary black holes. In these works, authors considered the accretion solutions that pass through the inner sonic point only. Essentially, these solutions are the subset of the generalized transonic accretion solutions as they ignored the flows containing multiple sonic points. In the previous Chapter, we studied the properties of the shocked accretion flow considering bremsstrahlung cooling where magnetic field strength was assumed to be moderate throughout the flow. In the present Chapter, we calculate the shock induced global accretion solution for flows having wide range of plasma $\beta$ parameters as $0.3 \leq \beta_{\rm in} \leq \infty$. With this, we further examine the effects of the dissipation parameters, namely viscosity ($\alpha_B$) and accretion rate ($\dot{m}$), on the properties of global accretion solutions that contains shock waves. Such a study is important in the sense that the dissipation processes are likely to influence the spectral and timing properties of the radiation emitted from the disc (Chakrabarti and Manickam 2000, Nandi *et al.* 2001a;b; 2012, Radhika and Nandi 2014, Iyer, Nandi, and Mandal 2015).

Our main concern here is to obtain the global magnetized accretion solution in presence of synchrotron cooling that contains shock wave (Fig. 3.2). For an accretion flow injected from a fixed outer edge, the dynamics of the shock front is regulated by cooling parameters, namely accretion rate ($\dot{m}$) and plasma $\beta$. Due to the presence of discontinuous shock transition, post-shock flow (*i.e.*,PSC) is compressed resulting a hot and dense PSC. Therefore, when accretion rate and/or magnetic field are increased, cooling efficiency is enhanced causing the reduction of thermal pressure at PSC. This eventually compels the shock front to move towards smaller distance in order to balance the total pressure across the shock (Fig. 3.3). In our model solution, we find that the accretion flow is very hot, magnetized and optically as well as geometrically thin in the inner part of the disc (Fig. 3.4). This eventually allows the hard radiation to escape from PSC with ease. Moreover, we find that shock induced global accretion solutions are not the discrete solutions as shock forms for a wide range of flow parameters. Interestingly, above a critical limit of cooling parameters ($\dot{m}^{\rm cri}$ and $\beta^{\rm cri}_{\rm edge}$), PSC ceases to exist as the standing shock conditions fails to satisfy in presence of excess cooling (Fig. 3.5-3.6).

Next, we put an effort to examine the properties of global shock solutions in both gas pressure as well as magnetic pressure dominated flow. While doing this, we calculate the critical viscosity parameter ($\alpha^{\rm cri}_B$) that caters standing shock waves. Here, we consider two different values of adiabatic index that represents accretion flow lying in the range between ultra-relativistic ($\gamma = 4/3$) to semi-non-relativistic ($\gamma = 1.5$) domain. We observe that in all cases, $\alpha^{\rm cri}_B$ initially increases with $\beta_{\rm in}$ and asymptotically approaches to the saturation values $\sim 0.4$ (for $\gamma = 4/3$) and $\sim 0.27$ (for $\gamma = 1.5$), respectively for gas pressure dominated flow Chakrabarti and Das (2004), King, Pringle, and Livio (2007), Das, Becker, and Le (2009), Kumar and Chattopadhyay (2013). Our steady model eventually establishes the fact that global shocks accretion solution can be obtained for fairly high viscosity parameter (Fig. 3.8).

We have further estimated the critical accretion rate ($\dot{m}^{\rm cri}$) that provides the global accretion solution including shock waves. We find that $\dot{m}^{\rm cri}$ is small for magnetically dominated flow as it is adequate to provide the required cooling efficiency that can sustain the standing shock in the accretion flow. As the strength of the magnetic field decreases, $\dot{m}^{\rm cri}$ gradually increases and ultimately $\dot{m}^{\rm cri}$ tends to become independent when magnetic fields are very weak leading to the gas pressure dominated flow (Fig. 3.9).

In Fig. 3.10, we have explored the typical spectrum of a magnetized accretion disc around black holes. For the purpose of representation, we consider two accretion flows having different magnetic field strengths. We find that the spectrum moves towards the high energy when magnetic field is large. This clearly indicates that the disc makes transition to the the brighter hard state as the disc becomes magnetically dominated. In addition, we compare the disc luminosities for accretion solutions with and without shock and observe that shock accretion solutions are radiatively more efficient than the shock free solutions. This provides a possible hint that global shock solutions are potentially preferred over the shock free solutions in understanding the energetics of the black hole sources.

More important findings we examine in our steady state model, when shocks under consideration are assumed to be dissipative in nature. In this circumstances, a part of the accreting energy is liberated at the shock which is allowed to escape through the disc surface. Interestingly, this available energy dissipated at shock can be used in powering the jets (Le and Becker 2004; 2005, Das, Becker, and Le 2009). Following this, we self-consistently calculate the maximum radiative luminosity at shock ($L^{\rm max}_{\rm shock}$) corresponding to $\Delta\mathcal{E}^{\rm max}$ as an observable quantity and argue that the obtained results may be used to explain the observational findings of radio luminosities corresponding to the black hole sources.

# Chapter 4

# Advective magnetized accretion flow around rotating black hole

In this Chapter, we study the properties of magnetized accretion flow around rotating black hole[1]. In particular, we have focussed on the transonic solution around the rotating black hole. The relativistic effect of the spinning black hole is approximated by assuming the pseudo-Kerr potential introduced by Chakrabarti and Mondal (2006). We self-consistently solve all the governing equations that describe the magnetized accretion flow around rotating black hole and obtain the global accretion solutions including shock waves. We study the properties of standing shock waves in terms of flow parameters and observe that shock formation takes place for an ample range of parameters both around weakly rotating ($a_k \rightarrow 0$) as well as rapidly rotating black holes ($a_k \sim 0.8$). We also calculate the critical accretion rate ($\dot{m}^{\rm cri}$) for standing shocks in magnetized accretion flow. It may be noted that $\dot{m}^{\rm cri}$ does not bear any universal value, rather it is largely dependent on the inflow parameters. We continue our study considering the fact that standing accretion shocks are dissipative by nature and calculate the maximum energy that can be extracted from the PSC. In reality, this available energy could be utilized in powering the jets (Sarkar and Das 2016; reference therein) as they seem to originate from PSC regions (Aktar *et al.* 2017; reference therein).

We organize the Chapter as follows. In Section 4.1, we write the model equations and carry out the analysis of transonic conditions. In Section 4.2, we display our results where shocked accretion solutions for magnetized flow and its properties are discussed.

---

[1] The contents of this chapter are under review in Das S., Sarkar B., 2018, MNRAS.

Moreover, we determine the critical inflow parameters for standing shock as well. We further study the characteristics of dissipative standing shock. Finally, in Section 4.3, concluding remarks are presented.

## 4.1 Governing Equations

In this Chapter, a thin, axisymmetric, magnetized accretion flow onto a rotating black hole is considered and the accretion disc is assumed to lie on the black hole equatorial plane. The magnetic field structure considered in the accretion disc is the same as described in Chapter 2. Moreover, we employ the cylindrical polar coordinate $(x, \phi, z)$ to study the properties of accretion flow, where black hole is placed at its origin. In order to express the flow variables, we choose an unit system as $M_{\rm BH} = c = G = 1$, where $M_{\rm BH}$ is the mass of the black hole, $c$ represents the speed of light and $G$ denotes the gravitational constant, respectively. Accordingly, length, angular momentum and time are measured in units of $GM_{\rm BH}/c^2$ , $GM_{\rm BH}/c$ and $GM_{\rm BH}/c^3$, respectively. In the subsequent sections, we choose $M_{\rm BH} = 10M_\odot$ as a reference value.

Considering steady state scenario, the governing equations of motion that describe the magnetized accreting matter are obtained as follows:
(i) Equation for radial momentum:

$$v\frac{dv}{dx} + \frac{1}{\rho}\frac{dP}{dx} + \frac{d\Psi_{\rm eff}}{dx} + \frac{\left\langle B_\phi^2 \right\rangle}{4\pi x \rho} = 0, \tag{4.1}$$

where $v$ and $\rho$ stand for the radial velocity and density of the flow and $P$ represents total pressure which we take into account as $P = p_{\rm gas} + p_{\rm mag}$, where $p_{\rm gas}$ and $p_{\rm mag}$ denote the gas pressure and the magnetic pressure of the flow. We obtain the gas pressure inside the disc as $p_{\rm gas} = R\rho T/\mu$, where $R$, $T$ and $\mu$, respectively, represent the gas constant, the temperature and the mean molecular weight. Here, we use $\mu = 0.5$ for fully ionized hydrogen. Further, the magnetic pressure is obtained as $p_{\rm mag} =< B_\phi^2 > /8\pi$. We define $\beta = p_{\rm gas}/p_{\rm mag}$ and using this, we attain total pressure as $P = p_{\rm gas}(\beta + 1)/\beta$. Moreover, in equation (4.1), $\Psi_{\rm eff}$ denotes the effective pseudo potential around a rotating black hole (see Section 1.3.2) (Chakrabarti and Mondal 2006) and is given as,

$$\Psi_{\rm eff} = -\frac{\mathcal{Q} + \sqrt{\mathcal{Q}^2 - 4\mathcal{P}\mathcal{R}}}{2\mathcal{P}},$$

where

$$\mathcal{P} = \frac{\epsilon^2\lambda^2}{2x^2},$$

$$\mathcal{Q} = -1 + \frac{\epsilon^2\omega\lambda r^2}{x^2} + \frac{2a_k\lambda}{r^2 x},$$

$$\mathcal{R} = 1 - \frac{1}{r - x_0} + \frac{2a_k\omega}{x} + \frac{\epsilon^2\omega^2 r^4}{2x^2}.$$

Here, $x$ represents the cylindrical radial distance and $r$ specifies spherical radial distance, respectively. Also, $\lambda$ stands for the specific angular momentum of the flow. In addition, we write $x_0 = 0.04 + 0.97a_k + 0.085a_k^2$, $\omega = 2a_k/(x^3 + a_k^2 x + 2a_k^2)$ and $\epsilon^2 = (x^2 - 2x + a_k^2)/(x^2 + a_k^2 + 2a_k^2/x)$, where $\epsilon$ refers the redshift factor and $a_k$ denotes the spin of the black hole. It is to be noted that the adopted pseudo potential satisfactorily mimics the space-time geometry around rotating black hole for $a_k \lesssim 0.8$ (Chakrabarti and Mondal 2006).

(ii) Mass flux conservation equation:

$$\dot{M} = 2\pi x \Sigma v, \tag{4.2}$$

where $\dot{M}$ specifies the accretion rate which we treat as global constant all throught and $\Sigma$ represents the vertically integrated density (Matsumoto *et al.* 1984). It may be noted that in this Chapter, the direction of the inward radial velocity is considered as positive always.

(iii) Angular momentum conservation equation:

$$v\frac{d\lambda(x)}{dx} + \frac{1}{\Sigma x}\frac{d}{dx}(x^2 T_{x\phi}) = 0. \tag{4.3}$$

Here, we assume the vertically integrated total stress to be dominated by the $x\phi$ component of the Maxwell stress $T_{x\phi}$. For the accretion flow with large radial velocity, $T_{x\phi}$ comes out to be (Chakrabarti and Das 2004, Machida, Nakamura, and Matsumoto 2006)

$$T_{x\phi} = \frac{< B_x B_\phi >}{4\pi} h = -\alpha_B (W + \Sigma v^2), \tag{4.4}$$

where $h$, $\alpha_B$ and $W$, respectively, represent the local disc height, the proportionality constant and the vertically integrated pressure of the flow (Matsumoto *et al.* 1984). Following the work of Shakura and Sunyaev (1973), we regard $\alpha_B$ as a global constant all throughout of the flow. Note that when $v$ is significantly small, as in the case of Keplerian disc, equation (4.4) reduces to '$\alpha$-model' (Shakura and Sunyaev 1973).

We consider thin disc approximation where infalling matter maintains hydrostatic equilibrium in the vertical direction and calculate the disc height ($h$) as, $h = a\sqrt{x/(\gamma \Psi_r')}$ where $\Psi_r' = \left(\frac{\partial \Psi_{\rm eff}}{\partial r}\right)_{z<<x}$, $z$ denotes local vertical scale height in the cylindrical coordinate system and $r = \sqrt{x^2 + z^2}$ (Das, Chakrabarti, and Mondal 2010). Here, we define the sound speed as $a = \sqrt{\gamma P/\rho}$, where $\gamma$ stands for the adiabatic index of the flow. In this Chapter, we assume $\gamma$ to remain constant along the flow and choose $\gamma = 4/3$.

(iv) The equation for entropy:

$$\Sigma v T \frac{ds}{dx} = \frac{hv}{\gamma - 1}\left(\frac{dp_{\rm gas}}{dx} - \frac{\gamma p_{\rm gas}}{\rho}\frac{d\rho}{dx}\right) = Q^- - Q^+, \tag{4.5}$$

where $T$ and $s$ refer to the temperature and specific entropy of the flow, respectively. Moreover, $Q^+$ denotes the heating rate and $Q^-$ represents the cooling rate of the flow. Meanwhile, the numerical simulation works of (Hirose, Krolik, and Stone 2006, Machida, Nakamura, and Matsumoto 2006) indicate that during accretion, heating of the accreting matter occurs because of the energy dissipation via magnetic reconnection process and is calculated as

$$Q^+ = \frac{< B_x B_\phi >}{4\pi} xh \frac{d\Omega}{dx} = -\alpha_B (W + \Sigma v^2) x \frac{d\Omega}{dx}, \tag{4.6}$$

where $\Omega$ stands for the angular velocity of the flow.

Usually, the accretion flow experiences heat loss as the consequences of the variety of cooling mechanisms, such as bremsstrahlung, synchrotron and Comptonization of bremsstrahlung as well as synchrotron photons. However, in the present Chapter, as the infalling matter is magnetized in nature, we therefore consider only the synchrotron radiative mechanism as dominant cooling process and the corresponding cooling rate is obtained as (Shapiro and Teukolsky 1983),

$$Q^- = \frac{S a^5 \rho h}{v}\sqrt{\frac{\Psi_r'}{x^3}}\frac{\beta^2}{(1+\beta)^3}, \tag{4.7}$$

with,

$$S = 1.4827 \times 10^{18} \frac{\dot{m}\mu^2 e^4}{I_n m_e^3 \gamma^{5/2}} \frac{1}{G M_\odot c^3},$$

where $e$ and $m_e$ represent the charge and mass of the electron and $\dot{m}$ denotes the accretion rate expressed in units of Eddington rate ($\dot{M}_{\rm Edd} = 1.39 \times 10^{17} \times M_{\rm BH}/M_\odot$ g s$^{-1}$). Also, $I_n = (2^n n!)^2/(2n+1)!$ and $n$ represents the polytropic index of the flow which is related to the adiabatic index as $n = 1/(\gamma - 1)$. We estimate the electron temperature employing the relation $T_e = (\sqrt{m_e/m_p})T_p$, where the coupling between ion and electron is neglected (Chattopadhyay and Chakrabarti 2002). Here, $m_p$ and $T_p$ refer the mass and temperature of the ion.

(v) The advection equation of toroidal magnetic flux:

Following induction equation, the advection rate of toroidal magnetic flux is obtained as,

$$\frac{\partial < B_\phi > \hat{\phi}}{\partial t} = \nabla \times \left( \vec{v} \times < B_\phi > \hat{\phi} - \frac{4\pi}{c} \eta \vec{j} \right), \tag{4.8}$$

where $\vec{v}$, $\vec{j}$ and $\eta$, respectively, represent the velocity vector, the current density and the resistivity of the flow. It may be noted that equation (4.8) is azimuthally averaged. For an accretion disc, since the Reynold number is generally very large, we ignore the magnetic-diffusion terms because of large length scale. Furthermore, here we ignore dynamo term as well. Considering steady state, the obtained equation is further vertically integrated employing the assumption that the azimuthally averaged toroidal magnetic fields disappear at disc surface. Based on these considerations, the toroidal magnetic flux advection rate is calculated as,

$$\dot{\Phi} = -\sqrt{4\pi} v h B_0(x), \tag{4.9}$$

where,

$$\begin{aligned} B_0(x) &= \langle B_\phi \rangle (x; z = 0) \\ &= 2^{5/4} \pi^{1/4} (RT/\mu)^{1/2} \Sigma^{1/2} h^{-1/2} \beta^{-1/2} \end{aligned}$$

denotes azimuthally averaged toroidal magnetic field resided at the equatorial plane of the accretion disc (Oda *et al.* 2007). Inside the accretion disc, if the magnetic flux is dissipated by the magnetic reconnection or escapes from the disc due to buoyancy, $\dot{\Phi}$ will not be conserved. Besides, when MRI driven dynamo augments the toroidal magnetic flux, $\dot{\Phi}$ may vary with radial coordinate. Keeping these findings in mind, we thus consider $\dot{\Phi} \propto x^{-\zeta}$ Oda *et al.* (2007), where $\zeta$ stands for a parameter describing the magnetic flux advection rate. Therefore, we have the following parametric relation as

$$\dot{\Phi}\left(x; \zeta, \dot{M}\right) \equiv \dot{\Phi}_{\rm edge} \left(\frac{x}{x_{\rm edge}}\right)^{-\zeta}, \tag{4.10}$$

where $\dot{\Phi}_{\rm edge}$ indicates the advection rate of the toroidal magnetic field at a large distance, usually the disc's outer edge ($x_{\rm edge}$). For $\zeta = 0$, radial magnetic flux remains conserved whereas, for $\zeta > 0$, the magnetic flux is increased with the decrease of $x$. However, for representation, in this study, we choose $\zeta = 1$ all throughout unless stated otherwise.

### 4.1.1 Analysis of transonic conditions

During the course of accretion, matter from the outer edge of the disc ($x_{\rm edge}$) proceeds towards the black hole under the influence of gravity. In reality, inflowing matter possesses negligible radial velocity at $x_{\rm edge}$ in contrast with the local sound speed and enters into the black hole with velocity equivalent to $c$. This findings evidently demand the transonic nature of the accreting matter. The radial coordinate where the accretion flow smoothly changes its sonic character from subsonic to supersonic state is commonly called as critical point. Below, we carry out the critical point analysis of the magnetized accretion flow by solving equations (4.1), (4.2), (4.3), (4.5), (4.9) and (4.10) simultaneously (Das 2007; and references therein) and is expressed as,

$$\frac{dv}{dx} = \frac{N}{D}, \tag{4.11}$$

where the numerator ($N$) is calculated as,

$$\begin{aligned}
N = {} & \frac{Sa^5}{v}\sqrt{\frac{\Psi'_r}{x^3}}\frac{\beta^2}{(1+\beta)^3} + \frac{2\alpha_B^2 I_n (a^2 g + \gamma v^2)^2}{\gamma^2 x v} \\
& + \left[\frac{[3+\beta(\gamma+1)]v}{(\gamma-1)(1+\beta)} - \frac{4\alpha_B^2 g I_n (a^2 g + \gamma v^2)}{\gamma v}\right]\left(\frac{d\Psi_{\rm eff}}{dx}\right) \\
& + \left[\frac{va^2(2\beta\gamma+4)}{2\gamma(\gamma-1)(1+\beta)} - \frac{2\alpha_B^2 I_n a^2 g (a^2 g + \gamma v^2)}{\gamma^2 v}\right]\left(\frac{d\ln\Psi'_r}{dx}\right) \\
& + \frac{2[3+\beta(\gamma+1)]a^2 v}{\gamma(\gamma-1)(1+\beta)^2 x} - \frac{3a^2 v(2\gamma\beta+3)}{2\gamma(\gamma-1)(1+\beta)x} \\
& + \frac{6\alpha_B^2 I_n a^2 g (a^2 g + \gamma v^2)}{\gamma^2 v x} - \frac{8\alpha_B^2 I_n a^2 g (a^2 g + \gamma v^2)}{\gamma^2 v (1+\beta) x} \\
& - \frac{a^2 v (4\zeta - 1)}{2\gamma x (\gamma-1)(1+\beta)} - \frac{4\lambda \alpha_B I_n (a^2 g + \gamma v^2)}{\gamma x^2}
\end{aligned} \tag{4.11a}$$

and the denominator $(D)$ is calculated as,

$$D = \frac{2a^2}{(\gamma-1)}\left[\frac{2}{\gamma(1+\beta)} + \frac{\beta}{1+\beta}\right] - \frac{[3+(\gamma+1)\beta]v^2}{(\gamma-1)(1+\beta)}$$
$$+\frac{2\alpha_B^2 I_n(a^2 g+\gamma v^2)}{\gamma}\left[(2g-1) - \frac{a^2 g}{\gamma v^2}\right]. \tag{4.11b}$$

In the above analysis, we define $g = I_{n+1}/I_n$.

Next, we calculate the derivative of $a$, $\lambda$ and $\beta$ with respect to $x$ as,

$$\frac{da}{dx} = \left(\frac{a}{v} - \frac{\gamma v}{a}\right)\frac{dv}{dx} + \frac{3a}{2x} - \frac{a}{2}\left(\frac{d\ln\Psi_r^{'}}{dx}\right)$$
$$-\frac{\gamma}{a}\left(\frac{d\Psi_{\rm eff}}{dx}\right) - \frac{2a}{(1+\beta)x} \tag{4.12}$$

$$\frac{d\lambda}{dx} = -\frac{\alpha_B x(a^2 g-\gamma v^2)}{\gamma v^2}\frac{dv}{dx} + \frac{2\alpha_B a x g}{\gamma v}\frac{da}{dx}$$
$$+\frac{\alpha_B(a^2 g+\gamma v^2)}{\gamma v} \tag{4.13}$$

$$\frac{d\beta}{dx} = \left[\frac{4(1+\beta)}{v} - \frac{3\gamma v(1+\beta)}{a^2}\right]\frac{dv}{dx} + \frac{9(1+\beta)}{2x}$$
$$-2(1+\beta)\left(\frac{d\ln\Psi_r^{'}}{dx}\right) - \frac{3\gamma(1+\beta)}{a^2}\frac{d\Psi_{\rm eff}}{dx}$$
$$-\frac{6}{x} + \frac{(1+\beta)(4\zeta-1)}{2x} \tag{4.14}$$

From equation (4.11), we obtain two conditions at the critical point (also known as '*sonic point*') as $N=0$ and $D=0$. Setting $D$ to zero, we have the expression of Mach number $(M = v/a)$ at the critical point $(x_c)$ as,

$$M_c = \sqrt{\frac{-m_2 - \sqrt{m_2^2 - 4m_1 m_3}}{2m_1}}, \tag{4.15}$$

where

$$m_1 = 2\alpha_B^2 I_n \gamma^2(\gamma-1)(2g-1)(1+\beta_c) - \gamma^2(3+(\gamma+1)\beta_c),$$
$$m_2 = 2\gamma(2+\gamma\beta_c) + 4\alpha_B^2 I_n \gamma g(g-1)(\gamma-1)(1+\beta_c),$$
$$m_3 = -2\alpha_B^2 I_n g^2(\gamma-1)(1+\beta_c).$$

Setting $N = 0$, we obtain a cubic equation of the sound speed ($a_c$) at $x_c$ as,

$$\mathcal{A}a_c^3 + \mathcal{B}a_c^2 + \mathcal{C}a_c + \mathcal{D} = 0, \tag{4.16}$$

where

$$\mathcal{A} = S\sqrt{\frac{\Psi'_r}{x_c^3}\frac{\beta_c^2}{(1+\beta_c)^3}},$$

$$\begin{aligned}
\mathcal{B} = {} & \frac{2\alpha_B^2 I_n(g+\gamma M_c^2)^2}{\gamma^2 x_c} + \frac{M_c^2(2\gamma\beta_c+4)}{2\gamma(\gamma-1)(1+\beta_c)}\left(\frac{d\ln\Psi'_r}{dx}\right) \\
& - \frac{2\alpha_B^2 I_n g(g+\gamma M_c^2)}{\gamma^2}\left(\frac{d\ln\Psi'_r}{dx}\right) \\
& + \frac{2[3+\beta_c(\gamma+1)]M_c^2}{\gamma(\gamma-1)(1+\beta_c)^2 x_c} \\
& - \frac{3M_c^2(2\gamma\beta_c+3)}{2\gamma(\gamma-1)(1+\beta_c)x_c} + \frac{6\alpha_B^2 I_n g(g+\gamma M_c^2)}{\gamma^2 x_c} \\
& - \frac{8\alpha_B^2 I_n g(g+\gamma M_c^2)}{\gamma^2(1+\beta_c)x_c} - \frac{(4\zeta-1)M_c^2}{2\gamma(\gamma-1)(1+\beta_c)x_c},
\end{aligned}$$

$$\mathcal{C} = -\frac{4\lambda_c\alpha_B I_n M_c(g+\gamma M_c^2)}{\gamma x_c^2},$$

$$\begin{aligned}
\mathcal{D} = {} & \left[\frac{[3+\beta_c(\gamma+1)]M_c^2}{(1+\beta_c)(\gamma-1)} - \frac{4\alpha_B^2 g I_n(g+\gamma M_c^2)}{\gamma}\right] \\
& \times\left(\frac{d\Psi_{\rm eff}}{dx}\right).
\end{aligned}$$

Here, the flow variables specified with subscript ‘c’ denote their values evaluated at $x_c$.

Now, using the accretion flow parameters, we solve equation (4.16) to obtain the sound speed ($a_c$) at $x_c$ and subsequently calculate $v_c$ using equation (4.15). By employing the values of $v_c$ and $a_c$ in Eq. (4.11), we examine the characteristics of the critical points. As before, in this Chapter, since our motivation is to investigate the structure of the magnetized accretion flow, we therefore focus into the accretion solutions only in the subsequent analysis.

## 4.2 Results and Discussions

### 4.2.1 Transonic Global Solutions

In the present Chapter, we intend to obtain the global magnetized transonic accretion solution that delineates a smooth connection between horizon and the disc edge. With this aim, we simultaneously solve the equations (4.11-4.14) for a specified set of flow parameters. While doing this, we treat $\dot{m}$, $\alpha_B$, and $\gamma$ as global parameters of the flow. Moreover, one requires $a_k$ value and the boundary values of $\lambda$ and $\beta$ at a given $x$ as local parameters to solve these equations. Since the black hole accretion solutions are necessarily transonic in nature, flow must pass through at least one critical point and therefore, it is reasonable to choose the boundary values of the flow at the critical point. With this, we hereby integrate equations (4.11-4.14) starting from the critical point once inwards up to just outside the black hole horizon and then outward up to a large distance (equivalently 'outer edge of the disc'). Ultimately, these two parts of the solution are joined to obtain a complete global transonic accretion solution. Depending on the input parameters, accretion flow may possess single or multiple critical points (Das, Chattopadhyay, and Chakrabarti 2001a, Sarkar and Das 2013) These critical points are classified as inner ($x_{\rm in}$) or outer ($x_{\rm out}$) critical points depending on whether they form close to or far away from the black hole horizon. It is to be noted that we present angular momentum ($\lambda$) in terms of Keplerian angular momentum $\lambda_K(\equiv \sqrt{x^3/(x-2)^2})$, corresponding to the Schwarzschild metric, all throughout the Chapter.

### 4.2.2 Global Accretion Solutions with Shock

When the accretion flow containing multiple critical points accretes on to a black hole, it first passes through the outer critical point ($x_{\rm out}$) to become supersonic and keeps on accreting further inwards. Meanwhile, flow starts experiencing centrifugal repulsion resulting the accumulation of matter in the nearby region of the black hole that ultimately induces the shock transition when the density threshold is reached. With this, an effective virtual barrier is formed around the black hole. At shock, supersonic flow jumps in to the subsonic branch that makes the post-shock flow hot as the kinetic energy of the flow is converted to the thermal energy. Moreover, across the shock, flow undergoes shock compression that ultimately causes the post-shock flow to become dense. Interestingly, 2nd law of thermodynamics suggests that shocked accretion

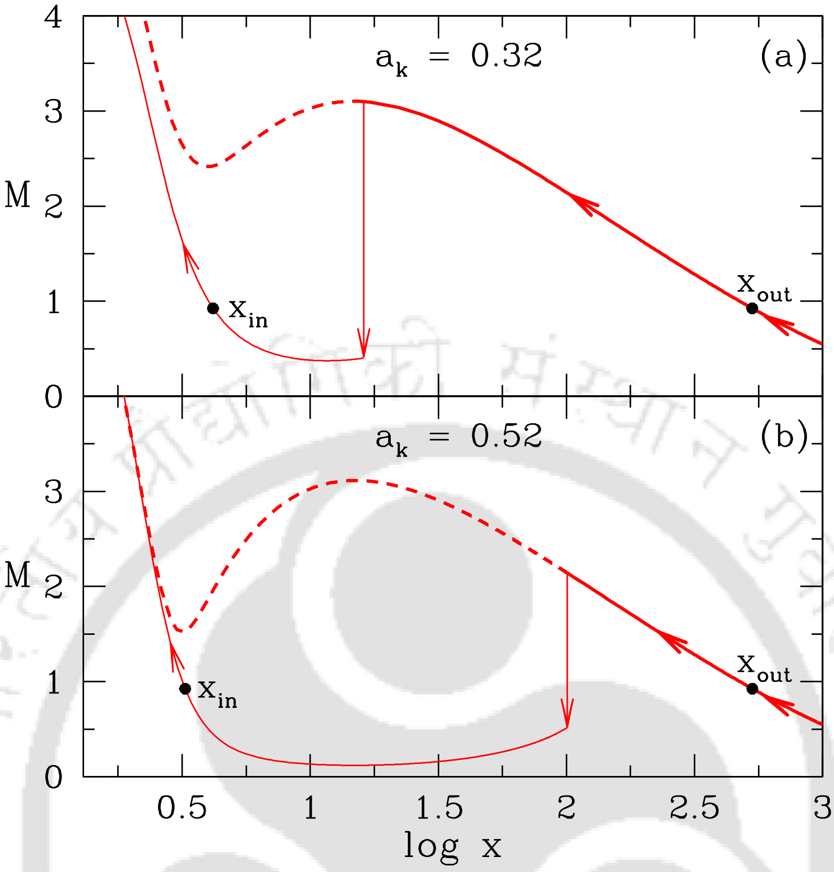

Fig. 4.1 Plot of Mach number with logarithmic radial distance. Flow is injected with $x_{\rm edge} = 1000$, $\mathcal{E}_{\rm edge} = 1.0793 \times 10^{-3}$, $\lambda_{\rm edge} = 0.1240\lambda_K$, $\beta_{\rm edge} = 1.6 \times 10^5$, $\alpha_B = 0.02$ and $\dot{m} = 0.05$, respectively. We choose in panel (a) $a_k = 0.32$ and (b) $a_k = 0.52$. In each panel, $x_{\rm in}$ and $x_{\rm out}$ are indicated using filled circles and shock transition is shown by vertical arrow. See text for details (Das and Sarkar 2018).

solutions are favorable as the entropy of the post-shock matter is comparatively higher than the pre-shock matter (Becker and Kazanas 2001). We calculate the entropy of the flow which is expressed as (Chakrabarti 1996a), $\dot{\mathcal{M}}(x) = \upsilon x a^{2n+1}\left(\frac{\beta}{1+\beta}\right)^n \sqrt{\frac{x}{\gamma \Psi_r'}}$. In the dissipation free limit, $\dot{\mathcal{M}}$ remains constant all throughout expect at the shock transition. What is more is that at the discontinuous transition, the conservation of mass flux, momentum flux, energy flux and magnetic flux are held in order to satisfy the standing shock conditions (see Section 3.2.1 of Chapter 3). In the subsequent analysis, upon employing these set of shock conditions, we compute the shock position and its diverse properties knowing the input parameters of the accretion flow.

In Fig. 4.1, we show the result obtained from one representative case where the variation of Mach number ($M = \upsilon/a$) with the logarithmic radial distance is depicted.

We choose the injection parameters of the flow at the outer edge ($x_{\rm edge} = 1000$) as $\mathcal{E}_{\rm edge} = 1.0793 \times 10^{-3}$, $\lambda_{\rm edge} = 0.1240\lambda_K$, $\beta_{\rm edge} = 1.6 \times 10^5$, $\alpha_B = 0.02$ and $\dot{m} = 0.05$, respectively. In Fig. 4.1(a), we consider the black hole to be slowly rotating having $a_k = 0.32$. Here, flow is subsonic at the outer edge and becomes supersonic after crossing the outer critical point located at $x_{\rm out} = 530.9$. The supersonic flow proceeds further inwards and encounters shock transition at $x_s = 16.2$ while jumping in to the subsonic branch. In the figure, shock position is shown using vertical arrow. Gradually flow velocity is increased as it moves inward and then it passes $x_{\rm in}$ smoothly at 4.1777 before crossing the horizon. Here, we show the direction of the flow motion using arrows and mark the inner and outer critical points with filled circles. Next, we consider a higher value of spin as $a_k = 0.52$ and inject matter keeping all the other parameters same as in Fig. 4.1(a). The result is depicted in Fig. 4.1(b), where the outer critical point, shock location and inner critical point are obtained as $x_{\rm out} = 531.43$, $x_{\rm s} = 100.62$ and $x_{\rm in} = 3.2502$, respectively. Thus for the same boundary conditions, when $a_k$ is increased, shock front moves away from the black hole horizon.

### 4.2.3 Properties of Standing Shocks

One of the pertinent aspect in understanding the magnetically supported accreting flow around the rotating black holes is to study the dependence of the shock position ($x_s$) on the $\beta$ values. Accordingly, we calculate $x_s$ in terms of $\beta_{\rm edge}$ for flows with fixed outer boundary values accreting on to a given black hole. For that, we choose the outer boundary parameters as $x_{\rm edge} = 1000$, $\mathcal{E}_{\rm edge} = 1.0793 \times 10^{-3}$, $\alpha_B = 0.02$ and $\dot{m} = 0.05$. In Fig. 4.2(a), we display the results obtained for $a_k = 0.4$, where solid, dotted and dashed curves are for $\lambda_{\rm edge} = 0.1285\lambda_K$, $0.1279\lambda_K$ and $0.1274\lambda_K$, respectively. We notice that the shock front proceeds towards the horizon with the decrease of $\beta_{\rm edge}$ irrespective to the values of $\lambda_{\rm edge}$. This happens because when $\beta_{\rm edge}$ is decreased, the efficiency of synchrotron cooling is enhanced due to the increase of magnetic activity inside the disc. The effect becomes more prominent at the inner part of the disc (*i.e.*, PSC) as, due to shock transition, both density and temperature are relatively higher there compared to the pre-shock flow. This renders the thermal pressure to drop down in the PSC region and ultimately shock front moves inward to maintain the pressure balance across it. Incidentally, keeping the all the boundary flow parameters fixed, one can not reduce $\beta_{\rm edge}$ indefinitely as shock ceases to exist when $\beta_{\rm edge} < \beta^{\rm cri}_{\rm edge}$ (shock conditions fail to satisfy there). It may be noted that $\beta^{\rm cri}_{\rm edge}$

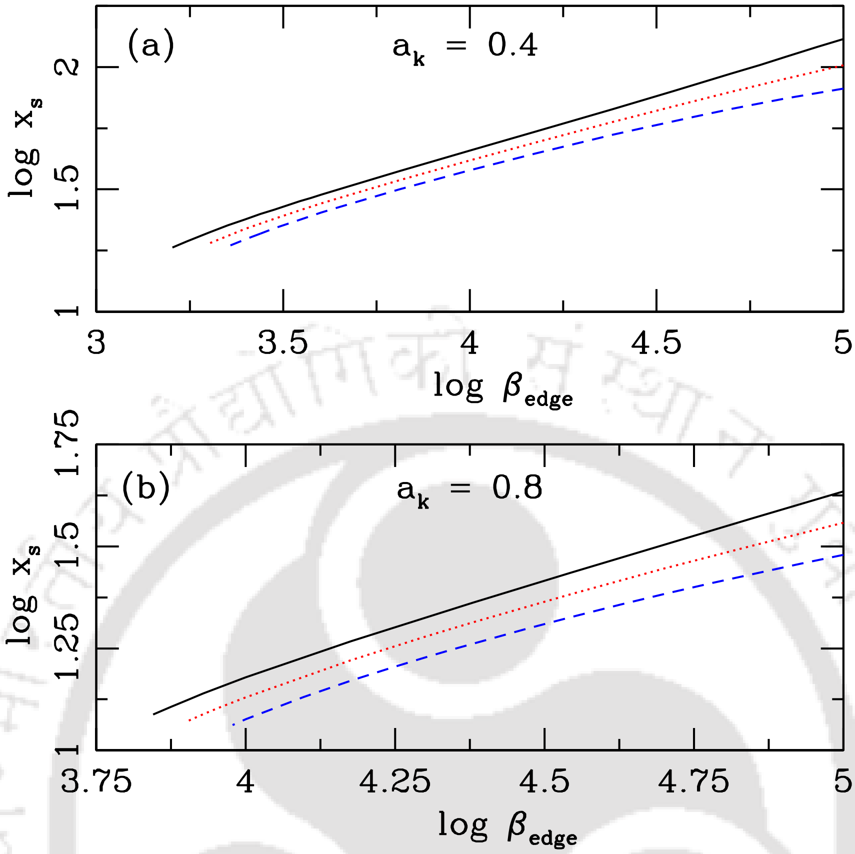

Fig. 4.2 Shock location ($x_s$) variation with $\beta_{\rm edge}$. Here, the inflow parameters are chosen as $x_{\rm edge} = 1000$, $\mathcal{E}_{\rm edge} = 1.0793 \times 10^{-3}$, $\alpha_B = 0.02$ and $\dot{m} = 0.05$, respectively. In every panel, spin of the black hole ($a_k$) is marked. In panel (a), results plotted with solid, dotted and dashed curves are obtained for $\lambda_{\rm edge} = 0.1285\lambda_K$, $0.1279\lambda_K$ and $0.1274\lambda_K$. And in panel (b), results depicted with solid, dotted and dashed curves are for $\lambda_{\rm edge} = 0.1144\lambda_K$, $0.1139\lambda_K$ and $0.1134\lambda_K$, respectively. See text for details (Das and Sarkar 2018).

does not have a universal value, instead it depends on the flow parameters fixed at the outer edge of the disc. Further, we depict the results for $a_k = 0.8$ in Fig. 4.2(b), where solid, dotted and dashed curves represent results corresponding to $\lambda_{\rm edge} = 0.1144\lambda_K$, $0.1139\lambda_K$ and $0.1134\lambda_K$, respectively. Here, we keep all the other flow parameters same as in Fig. 4.2(a). We find that the shock location proceeds towards the horizon with the decrease of $\beta_{\rm edge}$ in all cases as observed in Fig. 4.2(a).

Next, we examine the correlation of $\beta$ values between the inner and outer critical points for shock induced global accretion solutions. While doing this, we choose two cases where inflowing matters are accreted on to rotating black holes having different

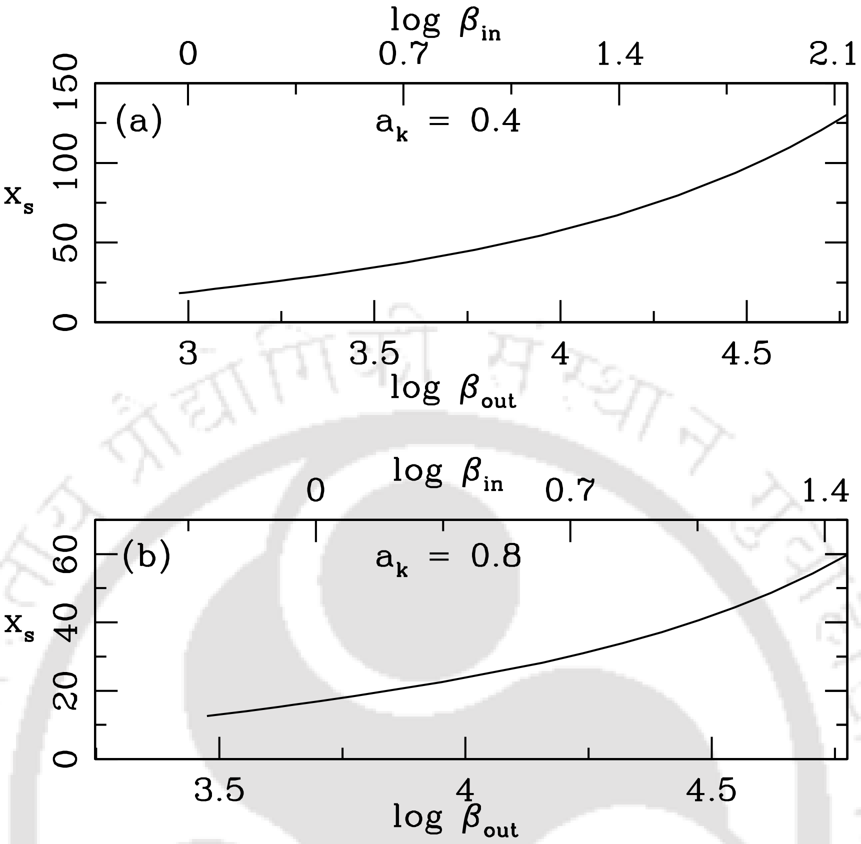

Fig. 4.3 Variation of the shock location ($x_s$) as function of $\beta_{\rm out}$ (lower axis) and $\beta_{\rm in}$ (upper axis). In each panel, $a_k$ is marked. See text for details (Das and Sarkar 2018).

spin parameters as $a_k = 0.4$ and 0.8, respectively. We choose the flow parameters at the outer edge of the disc as $x_{\rm edge} = 1000$, $\mathcal{E}_{\rm edge} = 1.0793 \times 10^{-3}$, $\alpha_B = 0.02$ and $\dot{m} = 0.05$, respectively. For $a_k = 0.4$, we consider the result depicted in Fig. 4.3(a) corresponding to $\lambda_{\rm edge} = 0.1285\lambda_K$ and show the variation of shock location as function of both $\beta_{\rm out}$ (lower horizontal axis) and $\beta_{\rm in}$ (upper horizontal axis). Here, $\beta_{\rm in}$ and $\beta_{\rm out}$ refer $\beta$ values measured at $x_{\rm in}$ and $x_{\rm out}$ , respectively. We see that $x_s$ decreases when the magnetic activity is increased ($\beta$ is decreased) inside the disc. We continue our study choosing the result presented in Fig. 4.3(b) for $\lambda_{\rm edge} = 0.1155\lambda_K$ and show the variation of $x_s$ in terms of $\beta_{\rm out}$ as well as $\beta_{\rm in}$ in Fig. 4.3(b). We observe that in all cases, $\beta_{\rm in} < \beta_{\rm out}$ all throughout. This finding is not surprising because, in our model, the advection of magnetic flux increases as the inflowing matter approaches towards the horizon and eventually, $\beta$ is reduced towards the inner part of the disc. Moreover, we find that shock solutions exist even for $\beta_{\rm in} < 1$ irrespective to the choice of $a_k$ value.

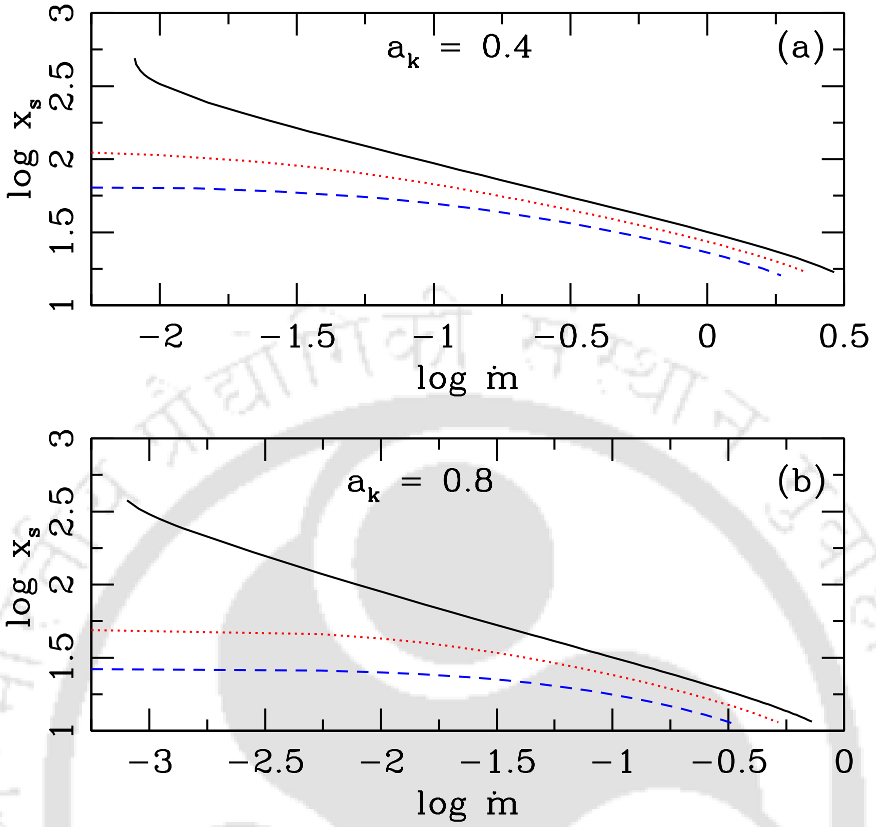

Fig. 4.4 Variation of the shock location ($x_s$) as function of $\dot{m}$. Flow parameters at the outer edge of the disc is chosen $x_{\rm edge} = 1000$, with $\mathcal{E}_{\rm edge} = 1.0793 \times 10^{-3}$, $\alpha_B = 0.02$ and $\beta_{\rm edge} = 10^5$, respectively. Results depicted in top and bottom panelsfor $a_k = 0.4$ and 0.8. In (a), solid, dotted and dashed curves are obtained for $\lambda_{\rm edge} = 0.1285\lambda_K$, $0.1274\lambda_K$ and $0.1263\lambda_K$ whereas insolid, dotted and dashed curves represents results for $\lambda_{\rm edge} = 0.1144\lambda_K$, $0.1134\lambda_K$ and $0.1123\lambda_K$. See text for details (Das and Sarkar 2018).

This evidently indicates that global transonic accretion solutions harbour standing shock waves both in gas pressure dominated as well as in magnetic pressure dominated flows for a wide range of $a_k$ values.

It is worthy to explore the effect of cooling on the formation of shock wave in an accretion flow and therefore, in Fig. 4.4, we study the variation of shock location ($x_s$) with accretion rate ($\dot{m}$). Towards this, we consider the flow injection parameters as $x_{\rm edge} = 1000$, $\beta_{\rm edge} = 10^5$, $\mathcal{E}_{\rm edge} = 1.0793 \times 10^{-3}$ and $\alpha_B = 0.02$, respectively. As before, in Fig. 4.4(a), we chose $a_k = 0.4$ and the profile of shock location ($x_s$) is presented for various values of $\lambda_{\rm edge}$. Here, solid, dotted and dashed curves represent flows injected with $\lambda_{\rm edge} = 0.1285\lambda_K$, $0.1274\lambda_K$ and $0.1263\lambda_K$, respectively. From the figure, it is clear that large range of $\dot{m}$ admits standing shock in magnetized accretion flow. Moreover, we find that for a given $\lambda_{\rm edge}$, $x_s$ moves inwards as $\dot{m}$ is increased. In reality, enhanced accretion rate boosts the efficiency of the radiative cooling that causes the flow to lose energy during accretion. Since PSC is hot and dense, the effect of cooling at PSC becomes profound that evidently decreases the post-shock thermal pressure. Consequently, this compels the shock front to settle down at some smaller distance to fulfill the shock conditions. Unfortunately, $\dot{m}$ can not be increased indefinitely due to the fact that when $\dot{m}$ exceeds its critical value ($\dot{m}^{\rm cri}$), standing shocks are no longer feasible as the shock conditions fail to satisfy there. Clearly, $\dot{m}^{\rm cri}$ does not retain a global value, rather it depends on the flow parameters. It is also apparent that the possibility of standing shock formation reduces with the increase of $\dot{m}$. Furthermore, it is intriguing to understand what happens to the flow when standing shock conditions fail to satisfy. Interestingly, in that case, inner part of the accretion flow may start to modulate exhibiting the feature of oscillatory shock (Das and Aktar 2015; and references therein). Unfortunately, the investigation of non-steady shock properties is beyond the scope of the present Chapter. In addition, we find that for a given $\dot{m}$, shock front recedes away from the black hole when $\lambda_{\rm edge}$ is increased. This happens due to the fact that higher $\lambda_{\rm edge}$ enhances the centrifugal repulsion that push the shock front outward against gravity. These findings establish the fact that shocks are centrifugally driven. In Fig. 4.4(b), we present the result corresponding to $a_k = 0.8$, where solid, dotted and dashed curves represent results obtained for $\lambda_{\rm edge} = 0.1144\lambda_K$, $0.1134\lambda_K$ and $0.1123\lambda_K$, respectively. Here also, we observe that the formation of shock and its dependence on $\dot{m}$ and $\lambda_{\rm edge}$ are in general similar to the results shown in Fig. 4.5(a).

For completeness, we investigate the variation of shock location in terms of viscosity ($\alpha_B$) for flows having fixed outer edge boundary parameters. Here, we choose the flow injection parameters as $x_{\rm edge} = 1000$, $\mathcal{E}_{\rm edge} = 1.0793 \times 10^{-3}$, $\beta_{\rm edge} = 10^5$ and $\dot{m} = 0.05$, respectively. In Fig. 4.5(a), we show the obtained results for $a_k = 0.4$, where solid, dotted and dashed curves are for $\lambda_{\rm edge} = 0.1285\lambda_K$, $0.1279\lambda_K$ and $0.1274\lambda_K$, respectively. Notice that shocked accretion solutions exist for a wide range of $\alpha_B$ and shock location shifts towards the horizon with the increase of $\alpha_B$ for all cases having different $\lambda_{\rm edge}$ values. In reality, as $\alpha_B$ is increased, angular momentum transport in the outward direction becomes more efficient that causes the weakening of centrifugal repulsion and hence, shock front is driven inward. When $\alpha_B$ exceeds its critical limit ($\alpha_B^{\rm cri}$), shock conditions do not remain favorable and as a result, standing shock

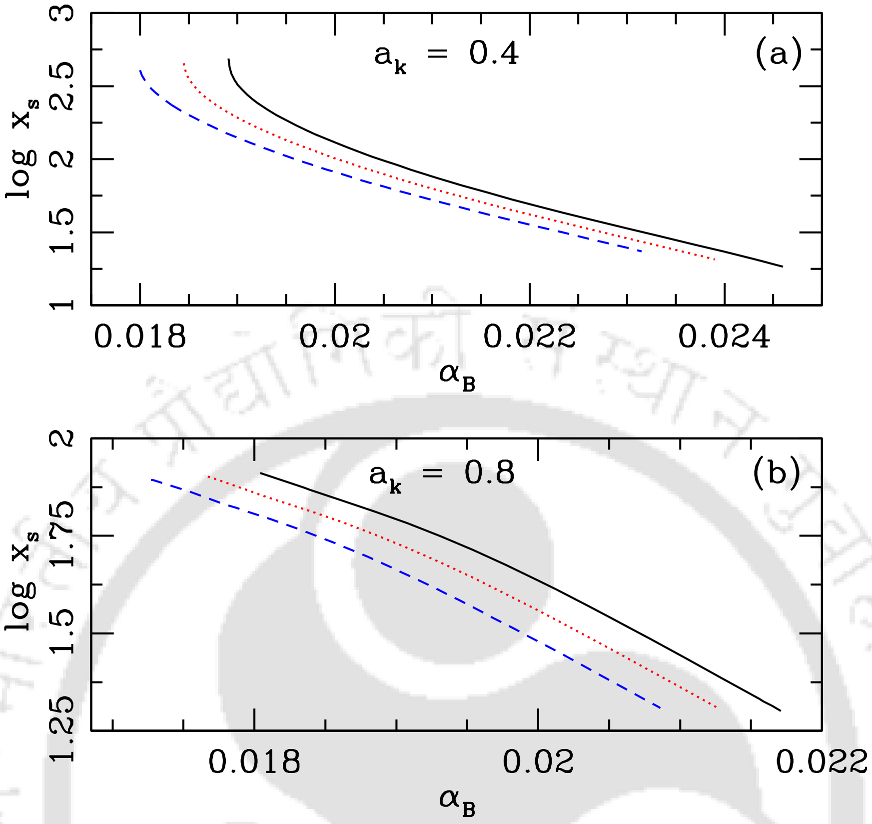

Fig. 4.5 Variation of the shock location ($x_s$) as function of $\alpha_B$. Accreting matter is supplied with inflow parameters as $x_{\rm edge} = 1000$, with $\mathcal{E}_{\rm edge} = 1.0793 \times 10^{-3}$, $\dot{m} = 0.05$ and $\beta_{\rm edge} = 10^5$, respectively. In each panel, $a_k$ is marked. In top panel (a), the results corresponding to $\lambda_{\rm edge} = 0.1285\lambda_K$, $0.1279\lambda_K$ and $0.1274\lambda_K$ are represented using solid, dotted and dashed line style. The same line style is used to denote the results for $\lambda_{\rm edge} = 0.1144\lambda_K$, $0.1139\lambda_K$ and $0.1134\lambda_K$ in lower panel (b). See text for details (Das and Sarkar 2018).

disappears. Again, it may be noted that $\alpha_B^{\rm cri}$ largely depends on the accretion flow parameters. Further, in Fig. 4.5(b), we display the result for $a_k = 0.8$, where solid, dotted and dashed curves denote results for $\lambda_{\rm edge} = 0.1144\lambda_K$, $0.1139\lambda_K$ and $0.1134\lambda_K$, respectively. Here, we find that shock location decreases with the increase of $\alpha_B$ around rotating black holes as well.

### 4.2.4 Parameter Space for Shock

We have already mentioned that during the course of accretion, inflowing matter may contain shock wave provided it possesses multiple critical points. Interestingly, one

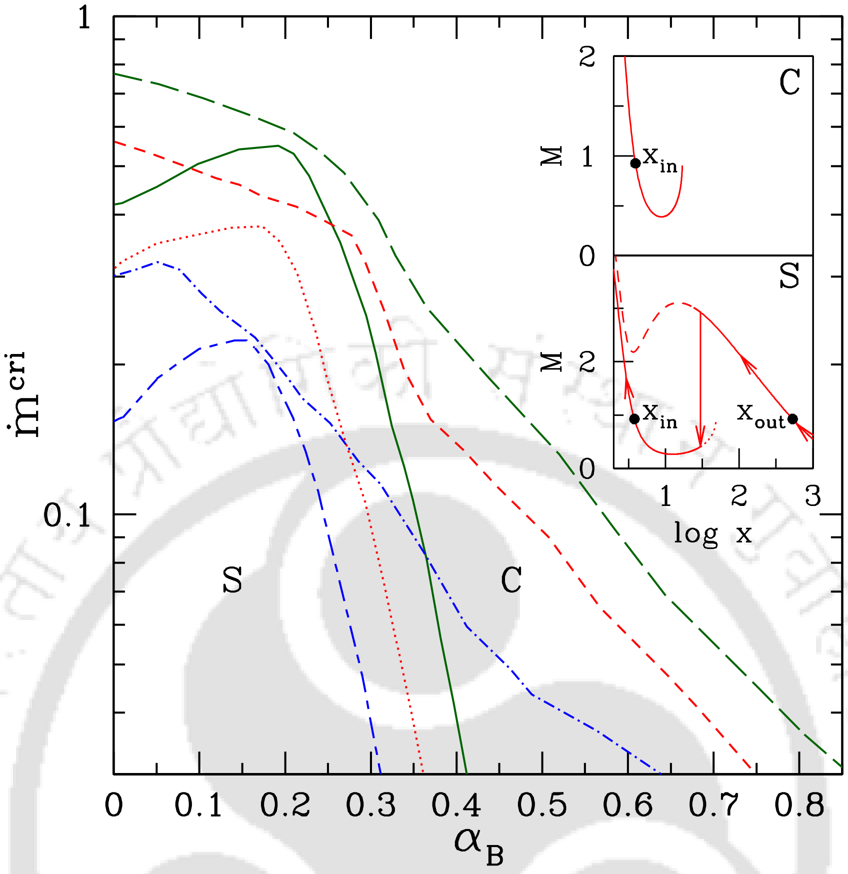

Fig. 4.6 Variation of critical accretion rate ($\dot{m}^{\rm cri}$) as a function of viscosity parameter ($\alpha_B$) for various $a_k$. Here, we choose $\beta_{\rm in} = 10$. Long-dashed, dashed and dot-dashed curves are obtained for $a_k = 0, 0.4$ and $0.8$ and the region bounded by them in $\alpha_B - \dot{m}^{\rm cri}$ plane provides closed accretion solutions passing through the inner critical point. In addition, solid, dotted and short-long-dashed curves represent the effective region corresponding to $a_k = 0, 0.4$ and $0.8$ that admits standing shock solutions. In the inset, examples of closed (marked with C) and shocked solutions (marked with S) are presented. See text for details (Das and Sarkar 2018).

can obtain standing shock solution, if the standing shock conditions are satisfied (see Section 4.2.2). But, when shock conditions are not favorable and the entropy content at the inner sonic point is higher than the outer sonic point, the shock formation never remains steady as the shock location becomes imaginary (Das, Chattopadhyay, and Chakrabarti 2001a) and therefore, shock starts to execute continuous back and forth oscillation that seems to exhibit the quasi-periodic oscillation phenomenon (Das, Chattopadhyay, and Chakrabarti 2001a). In this case, accretion solution passing through the inner sonic point fails to connect the black hole horizon to the outer edge of the disc as it becomes closed in the range $x_{\rm in} < x < x_{\rm out}$ with $M(x) = M_c$ (Chakrabarti and Das 2004). Needless to mention that it is not possible to examine the characteristic of the non-steady shock solution in the framework of the present Chapter, however, we estimate the critical accretion rate ($\dot{m}^{\rm cri}$) that provides accretion solutions containing standing shocks and/or closed topologies. While doing this, we fix $\beta_{\rm in} = 10$, and for a given $a_k$, we calculate $\dot{m}^{\rm cri}$ as function of $\alpha_B$, where $x_{\rm in}$ and $\lambda_{\rm in}$ are varied freely. Accordingly, in Fig. 4.6, we classify the parameter space spanned by $\alpha_B$ and $\dot{m}^{\rm cri}$ that provides closed topologies and standing shocks, respectively. Examples of closed topology (marked as C) and standing shock solution (marked as S) are displayed in the small boxes, where the variation of Mach number with radial coordinate is plotted. In the figure, long-dashed, short-dashed and dot-dashed curves are obtained for $a_k = 0$, 0.4 and 0.8 that separate the $\alpha_B - \dot{m}^{\rm cri}$ plane where left-bottom region allows closed topologies. Similarly, solid, dotted and short-long-dashed curves separate the standing shock parameter space for $a_k = 0$, 0.4 and 0.8, respectively. We observe that the shock parameter space appears to be the subset of parameter space for closed topology all throughout. This is expected as the region of closed topologies includes the region of standing as well as oscillating shocks. Meanwhile, Das and Chakrabarti (2008) showed that for fixed $a_k$, the effective region of standing shock parameter space shrinks with the increase of accretion rate for an inviscid flow. Actually, when the accretion rate is enhanced, cooling becomes more effective and hence, inflowing matter loses energy during accretion. On the other hand, the presence of viscosity enhances the flow energy as it accretes. Interestingly, when both dissipation processes, namely, viscosity and synchrotron cooling, are present in the flow, viscous dissipation effectively compensates a part of the energy loss happens due to cooling. Here, in a way, viscosity and cooling act oppositely in deciding the shock parameter space. However, as synchrotron cooling and viscous heating depend differently on the flow variables, one does not cancel the other effect completely (Das 2007). Overall, for a given $a_k$, standing shock continues to form until an optimum combination of $(\alpha_B, \dot{m}^{\rm cri})$ is reached which evidently exhibits as a peak in the $\alpha_B - \dot{m}^{\rm cri}$ plane. In general, the flow is dominated by cooling in the left side of the peak whereas viscous heating dominates on the other side. As expected, shock disappears when viscosity exceeds its critical limit (Chakrabarti and Das 2004). In addition, in case of a rapidly rotating black hole, shock forms in a relatively low angular momentum accretion flow (Aktar, Das, and Nandi 2015) that effectively causes the weak centrifugal repulsion and therefore, standing shock settles down at a smaller length scale. Moreover, increasing dissipation strengths (namely, $\alpha_B$ and $\dot{m}$) compel the shock front to move towards the horizon (see Fig. 4.4-4.5). This clearly indicates

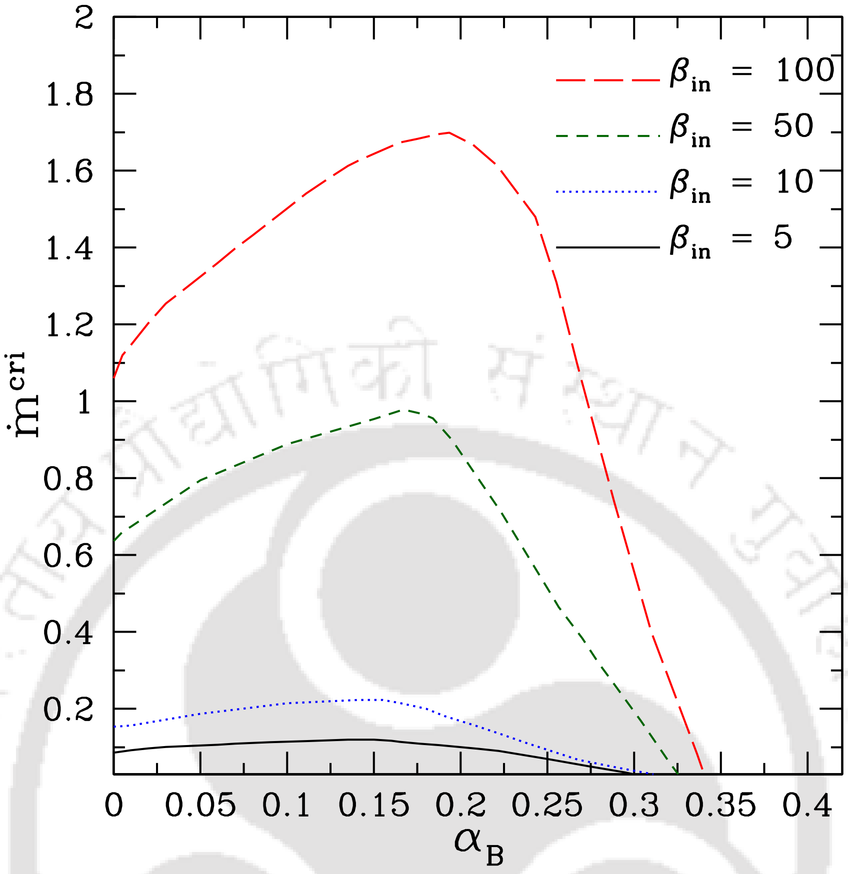

Fig. 4.7 Variation of critical accretion rate ($\dot{m}^{\rm cri}$) for standing accretion shock with viscosity parameter ($\alpha_B$) for different $\beta_{\rm in}$. Here, we fix black hole spin as $a_k = 0.8$. Solid, dotted, dashed and long-dashed curves denote results for $\beta_{\rm in} = 5, 10, 50$, and 100, respectively. See text for details (Das and Sarkar 2018).

that rapidly rotating black holes can sustain shocks for lower dissipation rates and we observe the similar findings in Fig. 4.6.

Now, we intend to study the effect of magnetic fields in deciding the effective region of parameter space in ($\alpha_B, \dot{m}^{\rm cri}$) plane for standing shock. In Fig. 4.7, we present the obtained results, where shock parameter space is computed for rapidly rotating black hole ($a_k = 0.8$) considering different $\beta_{\rm in}$ values. In the figure, the regions bounded with solid, dotted, short-dashed and long-dashed curves are obtained for $\beta_{\rm in}$ = 5, 10, 50 and 100, respectively. We observe that the effective region of the parameter space for shock gradually reduces with the decrease of $\beta_{\rm in}$. This happens due to the fact that when $\beta_{\rm in}$ is low, synchrotron cooling becomes very much effective and therefore, the level of dissipation experienced by the inflowing matter turns out to be significant even

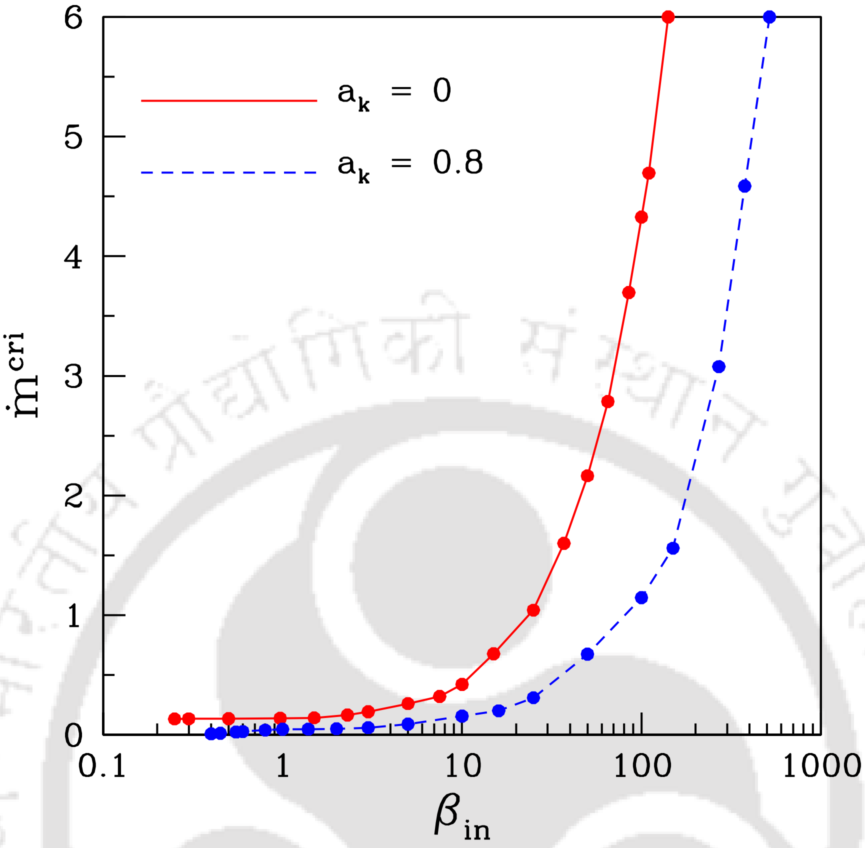

Fig. 4.8 Comparison of critical accretion rate $\dot{m}^{\rm cri}$ for shock with $\beta_{\rm in}$. In the plot, filled circles joined with solid line denote results for $a_k = 0$ and filled circles connected with dashed line represent results corresponding to $a_k = 0.8$, respectively. Here $\alpha_B = 0.01$ is used. See text for details (Das and Sarkar 2018).

with moderate accretion rates. Thus, the possibility of shock formation is eventually reduced as the magnetic activity is increased inside the disc.

We carry out the analysis further to calculate the critical accretion rate ($\dot{m}^{\rm cri}$) of the flow as function of $\beta_{\rm in}$ that provides global accretion solutions containing standing shock. In Fig. 4.8, we compare the critical accretion rate ($\dot{m}^{\rm cri}$) where solid and dashed curves represent the results obtained for non-rotating ($a_k = 0$) and rapidly rotating ($a_k = 0.8$) black holes, respectively. Here, we choose the viscosity parameter as $\alpha_B = 0.01$. We find that standing shocks exist for a wide range of $\beta_{\rm in}$ that effectively includes both gas pressure dominated flows ($\beta > 1$) as well as magnetic pressure dominated flows ($\beta < 1$). Since synchrotron process directly depends on the density and magnetic fields of the flow, one can achieve the desired cooling efficiency by suitably adjusting the accretion rate and plasma $\beta$. In the figure, we observe this findings for

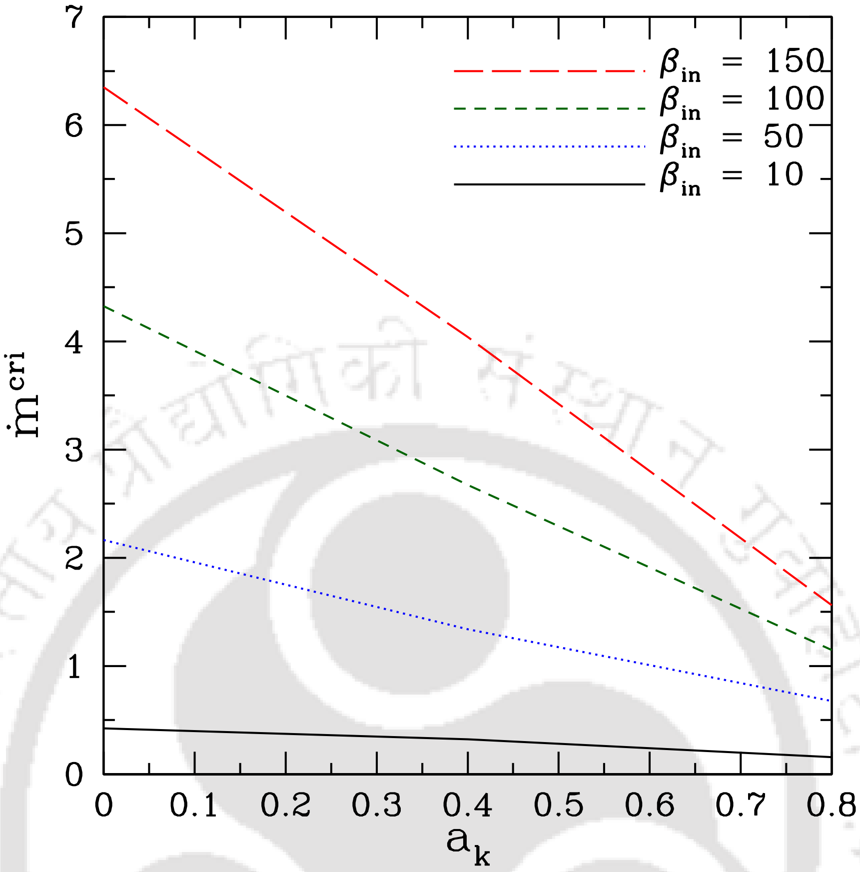

Fig. 4.9 Variation of critical accretion rate $\dot{m}^{\rm cri}$ with $a_k$ for shock. Here, we fix viscosity parameter as $\alpha_B = 0.01$. Results depicted with solid, dotted, dashed and big-dashed line styles correspond to $\beta_{\rm in} = 10, 50, 100$ and 150. See text for details (Das and Sarkar 2018).

both the cases (for $a_k = 0$ and 0.8) where the critical accretion rate ($\dot{m}^{\rm cri}$) for shock is found to be increased with $\beta_{\rm in}$ . In reality, when $\beta_{\rm in} < 1$, the inner part of the disc is magnetically dominated and a tiny amount of accretion rate is sufficient to cool the flow. On the other hand, as $\beta_{\rm in}$ is gradually increased, the strength of magnetic fields becomes weak and therefore, enhanced accretion rate is needed for the cooling of the flow. Interestingly, when $\beta_{\rm in} \gg 1$, magnetic fields becomes insignificant and flow is capable of sustaining standing shocks even for super-Eddington accretion rates ($\dot{m}^{\rm cri} > 1$). Moreover, we find that for a given $\beta_{\rm in}$, $\dot{m}^{\rm cri}$ is smaller for higher $a_k$. This clearly indicates that inflowing matter around rapidly rotating black holes contain shocks for relatively lower accretion rates which is consistent with the findings of Fig. 4.6.

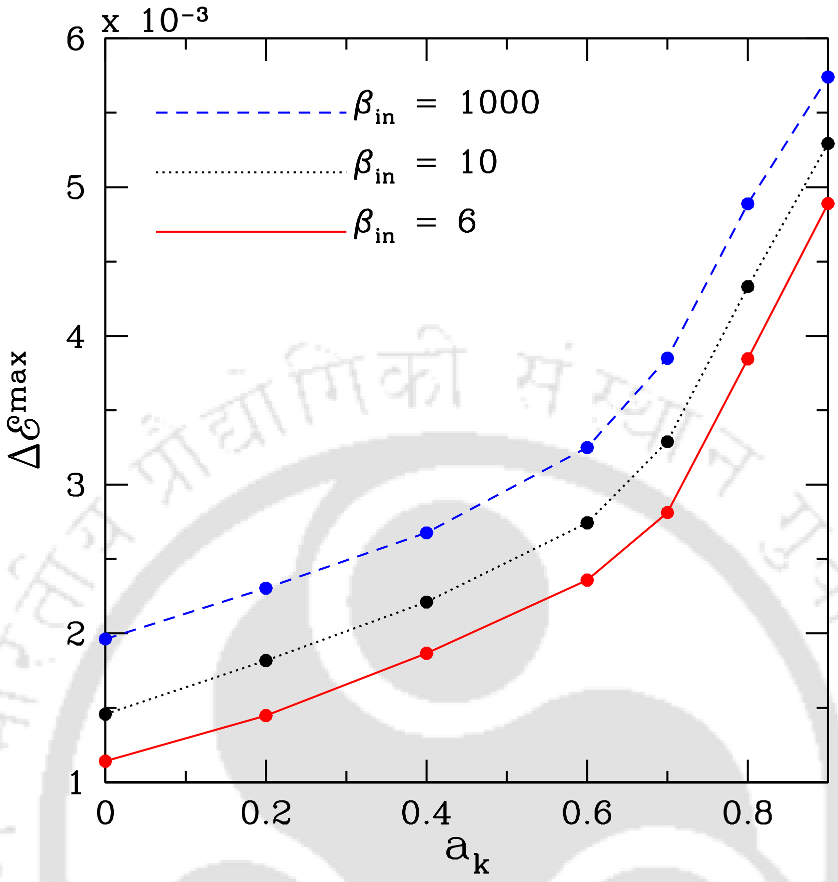

Fig. 4.10 Plot of maximum energy dissipation ($\Delta\mathcal{E}^{\rm max}$) at the shock with $a_k$ for three distinct values of $\beta_{\rm in}$. Here, we choose accretion rate as $\dot{m} = 0.05$ and fix viscosity parameter as $\alpha_B = 0.01$. Solid, dotted and dashed curves are obtained for $\beta_{\rm in} = 6, 10$ and 1000, respectively. See text for details (Das and Sarkar 2018).

In the context of the formation of standing shock in a magnetized accretion flow, we now illustrate the dependence of the critical accretion rate ($\dot{m}^{\rm cri}$) on the spin of the black hole ($a_k$) in Fig. 4.9. In order for that we fix the viscosity as $\alpha_B = 0.01$. Here, solid, dotted, dashed and long-dashed curves are obtained for $\beta_{\rm in}$ = 10, 50, 100 and 150, respectively. We observe that for a given $\beta_{\rm in}$, $\dot{m}^{\rm cri}$ decreases with the increase of $a_k$ in all cases. Moreover, here again we find that when $\beta_{\rm in}$ is large, accretion flow continues to sustain standing shock for higher accretion rate and vice versa.

### 4.2.5 Energy Extraction from PSC

So far, we have carried out the investigation of standing shock properties for flows accreting on to rotating black holes. While doing this, we consider the shock to be thin and non-dissipative and therefore, the specific energy remains essentially conserved across the shock front (Chakrabarti 1989). However, in reality, the nature of the shock can be dissipative as well and in that case, the available energy dissipated at shock escaped through the disc surfaces along the vertical direction. A part of this energy is then converted to hard radiations and the rest may be used in jet generation as jets seem to be originated from the PSC around rotating black holes (Aktar *et al.* 2017; and references therein). In effect, this cause the depletion of energy at PSC (Singh and Chakrabarti 2011). Moreover, (Chakrabarti and Titarchuk 1995) pointed out that the dissipative energy at shock is likely to be regulated via thermal Comptonization process that ultimately reduces the thermal energy of the PSC. Based on the above insight, we model the dissipated energy to be proportional to the temperature difference between the immediate pre-shock and post-shock flow. Following this, the energy loss ($\Delta\mathcal{E}$) at the shock is estimated as (Das, Chakrabarti, and Mondal 2010),

$$\Delta\mathcal{E} = fn(a_{+}^{2} - a_{-}^{2}), \tag{4.17}$$

where $a_{-}$ and $a_{+}$ specify the sound speed just before and after the shock transition. Here, $f$ refers the fractional value of thermal energy difference dissipated at shock and we treat it as free parameter (Das, Chakrabarti, and Mondal 2010, Singh and Chakrabarti 2011, Sarkar and Das 2013, Kumar and Chattopadhyay 2013, Sarkar, Das, and Mandal 2018). For the purpose of representation, in this Chapter, we choose $f = 0.1$ all throughout.

In Fig. 4.10, we show how the maximum energy dissipated at shock ($\Delta\mathcal{E}^{\rm max}$) is varied with $a_k$. While doing this, we choose $\dot{m} = 0.05$ and $\alpha_B = 0.01$, respectively and freely vary the other flow parameters. In the plot, solid, dotted and dashed curves illustrate the results for $\beta_{\rm in} = 6, 10$ and $1000$, respectively. We find that for given $\beta_{\rm in}$, $\Delta\mathcal{E}^{\rm max}$ increases with the increase of $a_k$. In general, standing shock forms at a smaller radial coordinate when $a_k$ is increased (Aktar, Das, and Nandi 2015) and hence, the thermal energy content across the shock is also increased. Eventually, the accessible thermal energy likely to be dissipated at shock is also enhanced. Therefore, for a given $\beta_{\rm in}$, we find a positive correlation between $\Delta\mathcal{E}^{\rm max}$ and $a_k$. On the other hand, as $\beta_{\rm in}$ is reduced, synchrotron cooling turns out to be more compelling in the flow due to the increase of magnetic field strength that ultimately reduces the thermal energy content in the PSC. Thus, $\Delta\mathcal{E}^{\rm max}$ diminishes with the decrease of $\beta_{\rm in}$ for fixed $a_k$. Finally, if the mass, spin and accretion rate of a given black hole candidate is known, the above formalism can be employed to estimate the maximum accessible energy in the PSC region and then this unbound energy could be compared with the observed radio jet kinetic power.

## 4.3 Chapter Conclusion

In this Chapter, we study the magnetized advection accretion flow around rotating black hole where viscosity and synchrotron cooling are considered as the dominant dissipation processes. We calculate the shock induced global accretion solutions and investigate the effect of dissipation parameters, such as $\dot{m}$, $\alpha_B$ and $\beta$, in deciding the formation of shock waves. The results are summarized below.

We find that accreting matter continues to harbour standing shock waves for $a_k \leqslant 0.8$ (see Fig. 4.1-4.5). It may be noted that we restrict the upper limit of $a_k$ below its maximum allowed value (*i.e.*, $a_k \rightarrow 1$), because the adopted potential satisfactorily mimics the space-time geometry around the rotating black hole for spin parameter $a_k \lesssim 0.8$ (Chakrabarti and Mondal 2006). Furthermore, we have realized that standing shocks in magnetized accretion flow are quite common and they exist for a wide range of flow parameters (see Fig. 4.2-4.5).

Next, we quantify the range of dissipation parameters that admit the formation of standing shocks in magnetized accretion flow around rotating black holes. We find that flow can sustain shock waves even when the level of dissipation is very high. More importantly, we observe that radiative cooling acts oppositely in contrast with viscous dissipation in deciding the shock parameter space (see Fig. 4.6). However, the effect of cooling can not be mitigated completely by viscous heating as their dependencies on the flow variables are different. Further, we find that the possibility of shock formation always decreases with the increase of dissipation strength. Subsequently, we calculate the critical accretion rate ($\dot{m}^{\rm cri}$) for standing shock. When accretion rate exceeds the critical limit, standing shock conditions are not satisfied and consequently, standing shock disappears. We find that $\dot{m}^{\rm cri}$ strongly depends on viscosity ($\alpha_B$), magnetic fields ($\beta$) and spin of the black hole ($a_k$), respectively (see Fig. 4.6-4.9). What is more is that standing shock exists in a magnetically dominated accretion flow when the accretion rate lies in general in the sub-Eddington domain ($\dot{m} < 1$) whereas for gas pressure dominated flow, shock forms even for super-Eddington accretion rate ($\dot{m} > 1$) (see Fig. 4.7-4.9).

Further, we obtain the standing shock solution for magnetized accretion flow, where the shock is considered to be dissipative by nature. The available energy dissipated at shock ($\Delta\mathcal{E}$) is usually escaped through the disc surface that is being utilized to power the jets/outflows (Le and Becker 2004; 2005, Das, Becker, and Le 2009). Towards this, we compute the maximum energy dissipated at shock ($\Delta\mathcal{E}^{max}$) and find that $\Delta\mathcal{E}^{max}$ increases with $a_k$ although its dependence on $\beta_{\rm in}$ is very much conspicuous.

Finally, we would like to mention that the present formalism is developed by adopting a simplified pseudo potential to delineate the gravitational effect around a rotating black hole. Incidentally, while studying the non-linear shock solutions, this approach allow us to avoid the mathematical complexity of general theory of relativity and at the same time it retains the salient features of space-time geometry around rotating black holes Chakrabarti and Mondal (2006). In this regard, although the present formalism introduces a bit of imperfections, however, we believe that the basic findings of this Chapter will qualitatively remain unaltered due to this approximation.

# Chapter 5

# Conclusions and Future perspective

In this thesis, we study global accretion solutions of magnetized accretion flows around black holes. We show the existence of shocks in global accretion solutions and investigate the properties of the post-shock corona (PSC).

In Chapter 2, we assume a Schwarzschild black hole and adopt the Comptonization of bremsstrahlung mechanism as the cooling mechanism active in the flow. We find that the dynamics of the PSC is controlled by the flow parameters, namely, viscosity, cooling efficiency factor ($\xi$) and strength of the magnetic field, respectively. We separate the effective region of the parameter space for standing shock and observe that shock can form for wide range of flow parameters. We calculate the critical viscosity parameter ($\alpha_B^{\rm cri}$) that allows standing shocks in the accretion flow around black holes. We find that $\alpha_B^{\rm cri}$ gradually increases as the plasma $\beta$ increases and ultimately tends to the value $\sim 0.3$ for gas pressure dominated flow. We estimate the maximum disc luminosity ($L_{\rm disc}^{\rm max}$) from our model for both the shocked and shock free global accretion solutions. We find that $L_{\rm disc}^{\rm max}$ positively correlates with $\xi$ and show that $L_{\rm disc}^{\rm max}$ always remains higher for shocked flows as compared to the shock free case. Further, we compute the maximum energy that could be extracted from the PSC. This is compared against the observed radio luminosity values for several supermassive black hole sources and close agreement is seen.

In Chapter 3, we assume synchrotron emission to be the dominant radiative process in the magnetized accretion flow around a stellar mass black hole. We calculate the shock induced global accretion solution for flows having wide range of plasma $\beta$ parameters as $0.3 \leqslant \beta_{\rm in} \leqslant \infty$. We calculate the critical viscosity parameter ($\alpha_B^{\rm cri}$)

that caters standing shock waves. We observe that $\alpha_B^{\rm cri}$ initially increases with $\beta_{\rm in}$ and asymptotically approaches to the saturation values $\sim 0.4$ (for $\gamma = 4/3$) and $\sim 0.27$ (for $\gamma = 1.5$), respectively for gas pressure dominated flow. We further show that shocked accretion solutions are more luminous than shock free solutions. Also, we find that when the strength of magnetic field is large, the flow is radiatively more efficient and the spectrum is shifted towards high energy. We have self-consistently estimated the maximum radiative luminosity at shock ($L_{\rm shock}^{\rm max}$) as an observable quantity which may be used to explain the observational findings of radio luminosities corresponding to the black hole sources.

In Chapter 4, we extend the formulations of Chapter 3 to include the effect of rotation of the black hole and explore the dynamical structure of an advection dominated, magnetized accretion flow around it. We obtained the global transonic accretion solutions with shocks and show that the rotation of the black hole significantly affects the shock properties and the dynamics of the PSC. We classify the parameter space spanned by critical accretion rate ($\dot{m}^{\rm cri}$) and viscosity ($\alpha_B$) into regions that allow closed accretion solution (passing through the inner sonic point only) and standing accretion shocks. We show that for a rotating black hole, accretion solutions with shock exist for $a_k \leqslant 0.8$. Furthermore, we show that standing shocks in magnetized accretion flow are quite common and they exist for a wide range of flow parameters. Also, we compute the maximum energy that could be extracted from the PSC and study its variation with magnetic parameter $\beta$ and spin of the black hole.

Chapter 5 presents the conclusion the work and gives future outlooks.

## Future prospects

Magnetized accretion flow around black holes has been an active area of research for many years. Due to the generalized nature of the content presented in the thesis, the work can be applied in future to address many important issues. Below we list some of the future prospects of this dissertation.

For the sake of simplicity, we choose pseudo-potentials in the thesis to account for the space time geometry around a black hole. Although this approach reduces the mathematical complexity of general theory of relativity while investigating non-linear phenomenon, such as shocks, the present formalism introduces a bit of imperfections. A pure general relativistic treatment of the work in future would be ideal.

We have considered the adiabatic constant of the flow as global constant in the thesis, although it should be estimated self-consistently from the thermal properties of the accreting matter. In general, since the inner part of the disc is very hot and the radiative cooling time of relativistic electrons are shorter than the non-relativistic ions, the accreting plasma is expected to be characterized by two temperature flows. In future, we plan to investigate the shock properties in two-temperature magnetized accretion flows around Schwarzschild as well as Kerr black holes. In a proper two-temperature analysis, the effect of all the relevant cooling mechanisms like bremsstrahlung, synchrotron and Comptonization can be investigated.

In the thesis, we have adopted a simple prescription of sound speed that allow us to obtain the accretion solutions in a simple way by retaining the memory of magnetic contribution of the flow. However, a steady MHD flow is usually characterized by the fast magnetosonic wave, slow magnetosonic wave and the Alfvén wave, respectively. Moreover, the speed of the magnetosonic waves depends on the angle between the wave vector and magnetic field. These aspects need to be incorporated while modelling the magnetized accretion flow around black holes.

Outflows have been neglected in this dissertation. But when toroidal flux lines are ejected bouyantly from the disc, the 'hoop-stress' would help to collimate the flow (Pudritz and Norman 1986, Lebedev *et al.* 2005, Singh and Chakrabarti 2011). It would be an important study to investigate the effect of magnetic fields on the outflow rates.

Optically thick, steady, magnetically supported discs were studied by Oda *et al.* (2009) to explain the bright/hard state in black hole candidates. They found that such discs are thermally stable. We plan to extend the model of optically thin low-$\beta$ discs in the thesis, to the optically thick regime. In this case, the total pressure in the disc would be contributed from the gas pressure, the radiation pressure as well as magnetic pressure. The existence of stationary shock solutions in such discs would be investigated and the consequences of these solutions explored.

In the thesis, the parameter $\zeta$ parametrizes the radial variation of the toroidal magnetic flux advection rate ($\dot{\Phi}$). In this dissertation, we have assumed $\zeta = 1$ throughout, as a representative case. However, in general it is expected that the variation of $\zeta$ will have significant effect on the radial structure of the disc. In particular, Oda *et al.* (2007) showed that the variation of $\zeta$ affects the temperature, plasma$-\beta$, accretion rate and optical depth in the disc. Since $\zeta$ will affect the angular momentum transport, the dynamics of shock is also likely to be goverened by the value of $\zeta$. This needs to be investigated in detail in future.

# References

Abbassi, S., Ghanbari, J., and Najjar, S.: 2008, *Monthly Notices of the Royal Astronomical Society* **388**, 663.

Abramowicz, M.A. and Zurek, W.H.: 1981, *Astrophys. J.* **246**, 314.

Abramowicz, M.A., Czerny, B., Lasota, J.P., and Szuszkiewicz, E.: 1988, *Astrophys. J.* **332**, 646.

Abramowicz, M.A. and Chakrabarti, S.K.: 1990, *Astrophys. J.* **350**, 281.

Abramowicz, M.A., Chen, X., Kato, S., Lasota, J.-P., and Regev, O.: 1995, *Astrophys. J.* **438**, L37.

Akizuki, C. and Fukue, J.: 2006, *Publications of the Astronomical Society of Japan* **58**, 469.

Aktar, R., Das, S., and Nandi, A.: 2015, *Monthly Notices of the Royal Astronomical Society* **453**, 3414.

Aktar, R., Das, S., Nandi, A., and Sreehari, H.: 2017, *Monthly Notices of the Royal Astronomical Society* **471**, 4806.

Armitage, P.J.: 1998, *Astrophys. J.* **501**, L189.

Aschenbach, B.: 2010, *Memorie della Societa Astronomica Italiana* **81**, 319.

Balbus, S.A. and Hawley, J.F.: 1991, *Astrophys. J.* **376**, 214.

Becker, P.A. and Kazanas, D.: 2001, *Astrophys. J.* **546**, 429.

Becker, P.A., Das, S., and Le, T.: 2008, *Astrophys. J.* **677**, L93.

Beloborodov, A.M.: 1998, *Monthly Notices of the Royal Astronomical Society* **297**, 739.

Bhattacharjee, A., Banerjee, I., Banerjee, A., Debnath, D., and Chakrabarti, S.K.: 2017, *Monthly Notices of the Royal Astronomical Society* **466**, 1372.

Blandford, R.D. and Znajek, R.L.: 1977, *Monthly Notices of the Royal Astronomical Society* **179**, 433.

Bondi, H. and Hoyle, F.: 1944, *Monthly Notices of the Royal Astronomical Society* **104**, 273.

Bondi, H.: 1952, *Monthly Notices of the Royal Astronomical Society* **112**, 195.

Brandenburg, A., Nordlund, A., Stein, R.F., and Torkelsson, U.: 1995, *Astrophys. J.* **446**, 741.

Bu, D.-F., Yuan, F., and Xie, F.-G.: 2009, *Monthly Notices of the Royal Astronomical Society* **392**, 325.

Clarke, C. and Carswell, B.: 2007, *Principles of Astrophysical Fluid Dynamics, by Cathie Clarke , Bob Carswell, Cambridge, UK: Cambridge University Press, 2007.*

Chakrabarti, S.K.: 1989, *Astrophys. J.* **347**, 365.

Chakrabarti, S.K.: 1990a, *Monthly Notices of the Royal Astronomical Society* **243**, 610.

Chakrabarti, S.K.: 1990b, *Theory of Transonic Astrophysical Flows. Edited by CHAKRABARTI SANDIP K. Published by World Scientific Publishing Co. Pte. Ltd.*.

Chakrabarti, S.K. and Molteni, D.: 1993, *Astrophys. J.* **417**, 671.

Chakrabarti, S. and Titarchuk, L.G.: 1995, *Astrophys. J.* **455**, 623.

Chakrabarti, S.K.: 1996a, *Astrophys. J.* **464**, 664.

Chakrabarti, S.K.: 1996b, *Monthly Notices of the Royal Astronomical Society* **283**, 325.

Chakrabarti, S.K.: 1997, *Astrophys. J.* **484**, 313.

Chakrabarti, S.K.: 1999, *Astron. Astroph.* **351**, 185.

Chakrabarti, S.K. and Manickam, S.G.: 2000, *Astrophys. J.* **531**, L41.

Chakrabarti, S.K. and Das, S.: 2004, *Monthly Notices of the Royal Astronomical Society* **349**, 649.

Chakrabarti, S.K., Acharyya, K., and Molteni, D.: 2004, *Astron. Astroph.* **421**, 1.

Chakrabarti, S.K. and Mandal, S.: 2006, *Astrophys. J.* **642**, L49.

Chakrabarti, S.K. and Mondal, S.: 2006, *Monthly Notices of the Royal Astronomical Society* **369**, 976.

Chattopadhyay, I. and Chakrabarti, S.K.: 2000, *International Journal of Modern Physics D* **9**, 717.

Chattopadhyay, I. and Chakrabarti, S.K.: 2002, *Monthly Notices of the Royal Astronomical Society* **333**, 454.

Chattopadhyay, I. and Chakrabarti, S.K.: 2011, *International Journal of Modern Physics D* **20**, 1597.

Chen, X. and Taam, R.E.: 1994, *Astrophys. J.* **431**, 732.

Chen, X.: 1995, *Monthly Notices of the Royal Astronomical Society* **275**, 641.

Chen, X., Abramowicz, M.A., Lasota, J.-P., Narayan, R., and Yi, I.: 1995, *Astrophys. J.* **443**, L61.

Das, S., Chattopadhyay, I., and Chakrabarti, S.K.: 2001a, *Astrophys. J.* **557**, 983.

Das, S., Chattopadhyay, I., Nandi, A., and Chakrabarti, S.K.: 2001b, *Astron. Astroph.* **379**, 683.

Das, S. and Chakrabarti, S.K.: 2004, *International Journal of Modern Physics D* **13**, 1955.

Das, S.: 2007, *Monthly Notices of the Royal Astronomical Society* **376**, 1659.

Das, S. and Chakrabarti, S.K.: 2008, *Monthly Notices of the Royal Astronomical Society* **389**, 371.

Das, S., Becker, P.A., and Le, T.: 2009, *Astrophys. J.* **702**, 649.

Das, S., Chakrabarti, S.K., and Mondal, S.: 2010, *Monthly Notices of the Royal Astronomical Society* **401**, 2053.

Das, S., Chattopadhyay, I., Nandi, A., and Molteni, D.: 2014, *Monthly Notices of the Royal Astronomical Society* **442**, 251.

Das, S. and Aktar, R.: 2015, *Astronomical Society of India Conference Series* **12**.

Das, S. and Sarkar, B.: 2018, *Monthly Notices of the Royal Astronomical Society*, under review.

de Gasperin F., et al.: 2012, *Astron. Astroph.* **547**, A56.

De Villiers, J.-P., Hawley, J.F., Krolik, J.H., and Hirose, S.: 2005, *Astrophys. J.* **620**, 878.

Dihingia, I.K., Das, S., and Mandal, S.: 2018, *Monthly Notices of the Royal Astronomical Society* **475**, 2164.

Eardley, D.M., Lightman, A.P., and Shapiro, S.L.: 1975, *Astrophys. J.* **199**, L153.

Faghei, K.: 2013, *Astrophysics and Space Science* **345**, 125.

Falcke, H. and Biermann, P.L.: 1999, *Astron. Astroph.* **342**, 49.

Falcke, H., Körding, E., and Markoff, S.: 2004, *Astron. Astroph.* **414**, 895.

Frank, J., King, A., and Raine, D.J.: 2002, *Accretion Power in Astrophysics*, Cambridge University Press, Cambridge.

Fukue, J.: 1987, *Publications of the Astronomical Society of Japan* **39**, 309.

Fukue, J.: 1990, *Publications of the Astronomical Society of Japan* **42**, 793.

Fukumura, K. and Tsuruta, S.: 2004, *Astrophys. J.* **611**, 964.

Fukumura, K., Takahashi, M., and Tsuruta, S.: 2007, *Astrophys. J.* **657**, 415.

Fukumura, K. and Kazanas, D.: 2007, *Astrophys. J.* **669**, 85.

Fukumura, K., Hendry, D., Clark, P., Tombesi, F., and Takahashi, M.: 2016, *Astrophys. J.* **827**, 31.

Garain, S.K., Ghosh, H., and Chakrabarti, S.K.: 2012, *Astrophys. J.* **758**, 114.

Garain, S.K., Ghosh, H., and Chakrabarti, S.K.: 2014, *Monthly Notices of the Royal Astronomical Society* **437**, 1329.

Giacconi, R., Gursky, H., Paolini, F.R., and Rossi, B.B.: 1962, *Physical Review Letters* **9**, 439.

Gierliński, M. and Newton, J.: 2006, *Monthly Notices of the Royal Astronomical Society* **370**, 837.

Gu, W.-M. and Lu, J.-F.: 2001, *Chinese Physics Letters* **18**, 148.

Gu, W.-M. and Lu, J.-F.: 2004, *Chinese Physics Letters* **21**, 2551.

Gu, W.-M. and Lu, J.-F.: 2006, *Monthly Notices of the Royal Astronomical Society* **365**, 647.

Hawley, J.F., Gammie, C.F., and Balbus, S.A.: 1995, *Astrophys. J.* **440**, 742.

Hawley, J.F., Gammie, C.F., and Balbus, S.A.: 1996, *Astrophys. J.* **464**, 690.

Hawley, J.F.: 2000, *Astrophys. J.* **528**, 462.

Hawley, J.F. and Krolik, J.H.: 2001, *Astrophys. J.* **548**, 348.

Hirose, S., Krolik, J.H., De Villiers, J.-P., and Hawley, J.F.: 2004, *Astrophys. J.* **606**, 1083.

Hirose, S., Krolik, J.H., and Stone, J.M.: 2006, *Astrophys. J.* **640**, 901.

Ichimaru, S.: 1977, *Astrophys. J.* **214**, 840.

Iyer, N., Nandi, A., and Mandal, S.: 2015, *Astrophys. J.* **807**, 108.

Johansen, A. and Levin, Y.: 2008, *Astron. Astroph.* **490**, 501.

Kadowaki, L.H.S., de Gouveia Dal Pino, E.M., and Singh, C.B.: 2015, *Astrophys. J.* **802**, 113.

King, A.R., Pringle, J.E., and Livio, M.: 2007, *Monthly Notices of the Royal Astronomical Society* **376**, 1740.

Koide, S., Shibata, K., Kudoh, T., and Meier, D.L.: 2002, *Science* **295**, 1688.

Krolik, J.H., Hirose, S., and Blaes, O.: 2007, *Astrophys. J.* **664**, 1045.

Kuo C. Y., et al., 2014, *Astrophys. J.* **783**, L33.

Kumar, R. and Chattopadhyay, I.: 2013, *Monthly Notices of the Royal Astronomical Society* **430**, 386.

Kumar, R., Chattopadhyay, I., and Mandal, S.: 2014, *Monthly Notices of the Royal Astronomical Society* **437**, 2992.

Kusunose, M. and Takahara, F.: 1985, *Progress of Theoretical Physics* **73**, 41.

Landau L. D., Lifshitz, E. D., 1959, Fluid Mechanics. Pergamon, New York

Le, T. and Becker, P.A.: 2004, *Astrophys. J.* **617**, L25.

Le, T. and Becker, P.A.: 2005, *Astrophys. J.* **632**, 476.

Le, T. and Becker, P.A.: 2007, *Astrophys. J.* **661**, 416.

Lebedev S. V., et al., 2005, *Monthly Notices of the Royal Astronomical Society* **361**, 97.

Liang, E.P.T. and Thompson, K.A.: 1980, *Astrophys. J.* **240**, 271.

Lu, J.-F. and Yuan, F.: 1998, *Monthly Notices of the Royal Astronomical Society* **295**, 66.

Lu, J.-F., Gu, W.-M., and Yuan, F.: 1999, *Astrophys. J.* **523**, 340.

Lynden-Bell, D.: 1969, *Nature* **223**, 690.

Machida, M., Hayashi, M.R., and Matsumoto, R.: 2000, *Astrophys. J.* **532**, L67.

Machida, M. and Matsumoto, R.: 2003, *Astrophys. J.* **585**, 429.

Machida, M., Nakamura, K.E., and Matsumoto, R.: 2006, *Publications of the Astronomical Society of Japan* **58**, 193.

Madejski, G., Done, C., and Zycki, P.: 1999, *Astronomische Nachrichten* **320**, 240.

Mandal, S. and Chakrabarti, S.K.: 2005a, *Astron. Astroph.* **434**, 839.

Mandal, S. and Chakrabarti, S.K.: 2005b, *Astrophysics and Space Science* **297**, 269.

Matsumoto, R., Kato, S., Fukue, J., and Okazaki, A.T.: 1984, *Publications of the Astronomical Society of Japan* **36**, 71.

McKinney, J.C. and Gammie, C.F.: 2004, *Astrophys. J.* **611**, 977.

Melia, F. and Misra, R.: 1993, *Astrophys. J.* **411**, 797.

Mineshige, S., Kusnose, M., and Matsumoto, R.: 1995, *Astrophys. J.* **445**, L43.

Molteni, D., Lanzafame, G., and Chakrabarti, S.K.: 1994, *Astrophys. J.* **425**, 161.

Molteni, D., Sponholz, H., and Chakrabarti, S.K.: 1996b, *Astrophys. J.* **457**, 805.

Molteni, D., Tóth, G., and Kuznetsov, O.A.: 1999, *Astrophys. J.* **516**, 411.

Mondal, S. and Chakrabarti, S.K.: 2006, *Monthly Notices of the Royal Astronomical Society* **371**, 1418.

Mosallanezhad, A., Abbassi, S., and Beiranvand, N.: 2014, *Monthly Notices of the Royal Astronomical Society* **437**, 3112.

Mosallanezhad, A., Bu, D., and Yuan, F.: 2016, *Monthly Notices of the Royal Astronomical Society* **456**, 2877.

Nandi, A., Chakrabarti, S.K., Vadawale, S.V., and Rao, A.R.: 2001a, *Astron. Astroph.* **380**, 245.

Nandi, A., Manickam, S.G., Rao, A.R., and Chakrabarti, S.K.: 2001b, *Monthly Notices of the Royal Astronomical Society* **324**, 267.

Nandi, A., Debnath, D., Mandal, S., and Chakrabarti, S.K.: 2012, *Astron. Astroph.* **542**, A56.

Narayan, R. and Popham, R.: 1993, *Nature* **362**, 820.

Narayan, R. and Yi, I.: 1994, *Astrophys. J.* **428**, L13.

Narayan, R. and Yi, I.: 1995a, *Astrophys. J.* **444**, 231.

Narayan, R. and Yi, I.: 1995b, *Astrophys. J.* **452**, 710.

Narayan, R., Kato, S., and Honma, F.: 1997, *Astrophys. J.* **476**, 49.

Nishikawa, K.-I., Richardson, G., Koide, S., Shibata, K., Kudoh, T., Hardee, P., and Fishman, G.J.: 2005, *Astrophys. J.* **625**, 60.

Nobuta, K. and Hanawa, T.: 1999, *Astrophys. J.* **510**, 614.

Novikov I. D., Thorne K. S., 1973, in DeWitt C., DeWitt B., eds, Black Holes. Gordon & Breach, New York, p. 345

Oda, H., Machida, M., Nakamura, K.E., and Matsumoto, R.: 2007, *Publications of the Astronomical Society of Japan* **59**, 457.

Oda, H., Machida, M., Nakamura, K.E., and Matsumoto, R.: 2009, *Astrophys. J.* **697**, 16.

Oda, H., Machida, M., Nakamura, K.E., and Matsumoto, R.: 2010, *Astrophys. J.* **712**, 639.

Oda, H., Machida, M., Nakamura, K.E., Matsumoto, R., and Narayan, R.: 2012, *Publications of the Astronomical Society of Japan* **64**, 15.

Okuda, T., Teresi, V., Toscano, E., and Molteni, D.: 2004, *Publications of the Astronomical Society of Japan* **56**, 547.

Okuda, T., Teresi, V., and Molteni, D.: 2008, *Astrophysics of Compact Objects* **968**, 417.

Okuda, T.: 2014, *Monthly Notices of the Royal Astronomical Society* **441**, 2354.

Okuda, T. and Das, S.: 2015, *Monthly Notices of the Royal Astronomical Society* **453**, 147.

Paczyńsky, B. and Wiita, P.J.: 1980, *Astron. Astroph.* **88**, 23.

Pariev, V.I., Blackman, E.G., and Boldyrev, S.A.: 2003, *Astron. Astroph.* **407**, 403.

Parker, E.N.: 1966, *Astrophys. J.* **145**, 811.

Pessah, M.E. and Psaltis, D.: 2005, *Astrophys. J.* **628**, 879.

Peterson B. M., et al.: 2004, *Astrophys. J.* **613**, 682.

Piran, T.: 1978, *Astrophys. J.* **221**, 652.

Pringle, J.E. and Rees, M.J.: 1972, *Astron. Astroph.* **21**, 1.

Pringle, J.E.: 1976, *Monthly Notices of the Royal Astronomical Society* **177**, 65.

Pudritz, R.E. and Norman, C.A.: 1986, *Canadian Journal of Physics* **64**, 501.

Radhika, D. and Nandi, A.: 2014, *Advances in Space Research* **54**, 1678.

Radhika, D., Nandi, A., Agrawal, V.K., and Seetha, S.: 2016, *Monthly Notices of the Royal Astronomical Society* **460**, 4403.

Rajesh, S.R. and Mukhopadhyay, B.: 2010, *Monthly Notices of the Royal Astronomical Society* **402**, 961.

Riffel, R.A., Storchi-Bergmann, T., and Winge, C.: 2013, *Monthly Notices of the Royal Astronomical Society* **430**, 2249.

Ryu, D., Chakrabarti, S.K., and Molteni, D.: 1997, *Astrophys. J.* **474**, 378.

Sądowski, A.: 2009, *The Astrophysical Journal Supplement Series* **183**, 171.

Salpeter, E.E.: 1964, *Astrophys. J.* **140**, 796.

Samadi, M., Abbassi, S., and Khajavi, M.: 2014, *Monthly Notices of the Royal Astronomical Society* **437**, 3124.

Satyapal, S., Sambruna, R.M., and Dudik, R.P.: 2004, *Astron. Astroph.* **414**, 825.

Sarkar, B. and Das, S.: 2013, *Astronomical Society of India Conference Series* **8**, 143.

Sarkar, B. and Das, S.: 2016, *Monthly Notices of the Royal Astronomical Society* **461**, 190.

Sarkar, B., Das, S., and Mandal, S.: 2018, *Monthly Notices of the Royal Astronomical Society* **473**, 2415.

Schmidt, M.: 1963, *Nature* **197**, 1040.

Shakura, N.I.: 1972, *Astronomicheskii Zhurnal* **49**, 921 (1973, Sov. Astron., 16, 756).

Shakura, N.I. and Sunyaev, R.A.: 1973, *Astron. Astroph.* **24**, 337.

Shafi, N., Oosterloo, T.A., Morganti, R., Colafrancesco, S., and Booth, R.: 2015, *Monthly Notices of the Royal Astronomical Society* **454**, 1404.

Shapiro, S.L., Lightman, A.P., and Eardley, D.M.: 1976, *Astrophys. J.* **204**, 187.

Shapiro, S.L. and Teukolsky, S.A.: 1983, *Black Holes, White Dwarfs and Neutron Stars: The Physics of Compact Objects. New York, Wiley-Interscience..*

Shibata, K., Tajima, T., and Matsumoto, R.: 1990, *Astrophys. J.* **350**, 295.

Singh, C.B. and Chakrabarti, S.K.: 2011, *Monthly Notices of the Royal Astronomical Society* **410**, 2414.

Stone, J.M., Hawley, J.F., Gammie, C.F., and Balbus, S.A.: 1996, *Astrophys. J.* **463**, 656.

Suková, P. and Janiuk, A.: 2015, *Monthly Notices of the Royal Astronomical Society* **447**, 1565.

Suková, P., Charzyński, S., and Janiuk, A.: 2017, *Monthly Notices of the Royal Astronomical Society* **472**, 4327.

Takahashi, M., Goto, J., Fukumura, K., Rilett, D., and Tsuruta, S.: 2006, *Astrophys. J.* **645**, 1408.

Wandel, A. and Liang, E.P.: 1991, *Astrophys. J.* **380**, 84.

Walsh, J.L., Barth, A.J., Ho, L.C., and Sarzi, M.: 2013, *Astrophys. J.* **770**, 86.

Xie, F.-G. and Yuan, F.: 2012, *Monthly Notices of the Royal Astronomical Society* **427**, 1580.

Yadav, J.S., Rao, A.R., Agrawal, P.C., Paul, B., Seetha, S., and Kasturirangan, K.: 1999, *Astrophys. J.* **517**, 935.

Yamauchi, A., Nakai, N., Sato, N., and Diamond, P.: 2004, *Publications of the Astronomical Society of Japan* **56**, 605.

Yuan, F.: 2001, *Monthly Notices of the Royal Astronomical Society* **324**, 119.

Yuan, F., Markoff, S., and Falcke, H.: 2002a, *Astron. Astroph.* **383**, 854.

Yuan, F., Markoff, S., Falcke, H., and Biermann, P.L.: 2002b, *Astron. Astroph.* **391**, 139.

Yuan, F. and Narayan, R.: 2014, *Annual Review of Astronomy and Astrophysics* **52**, 529.

Zel'dovich Y. B., Novikov I. D.: 1964, *Usp. Fiz. Nauk*, **84**, 377

Ziolkowski, J.: 2010, *Memorie della Societa Astronomica Italiana* **81**, 294.